Spring 2019

Chemically-bonded enamel-coated steel pipelines for corrosion protection and flow efficiency

Liang Fan

Department: Civil, Architectural and Environmental Engineering

CHEMICALLY-BONDED ENAMEL-COATED STEEL PIPELINES FOR CORROSION PROTECTION AND FLOW EFFICIENCY

by

LIANG FAN

A DISSERTATION

Presented to the Faculty of the Graduate School of the

MISSOURI UNIVERSITY OF SCIENCE AND TECHNOLOGY

In Partial Fulfillment of the Requirements for the Degree

DOCTOR OF PHILOSOPHY

in

CIVIL ENGINEERING

2019

Approved by:

Dr. Genda Chen, Advisor
Dr. Richard K. Brow
Dr. Hongyan Ma
Dr. Mohamed ElGawady
Dr. Lesley H. Sneed

ABSTRACT

This study is to explore and develop chemically-bonded enamel coating (200-300 um) on steel pipes, when subjected to soil and thermal environments, in order to improve the corrosion protection and safety of hazardous liquid and natural gas pipelines while reducing pressure loss. Out of five types of enamels and their various mixtures, Tomatec slurry and GP2118 powder were selected for steel pipeline applications. They were applied at approximately 810 °C to the inside surface of steel pipes in wet and electrostatic processes, respectively. The thickness and surface roughness of the enamel coating were measured using a gauge and an optical microscope, respectively. The microstructure and porosity of the coating, and coating-steel bond strength were characterized using scanning electron microscopy and PosiTest, respectively. The corrosion resistance of enamel-coated pipelines, with and without cathodic protection (CP), is evaluated using salt spray and electrochemical tests. The stress distribution of enamel-coated pipes and their susceptibility to stress corrosion cracking (SCC) were studied with finite element analyses and slow strain rate tests, respectively. The surface roughness of the two coatings were ~ 1 μm and quite desirable in oil and gas transmission. Small Fe protrusions grew into each coating to form anchor points with a bond strength of 17 MPa between the enamel and its steel substrate. The residual thermal stress remained at the coating-steel interface is 2.5 MPa and thus negligible. Both enamel coatings increased the corrosion resistance of steel pipes in NaCl solution by three orders of magnitude. CP neither caused debonding at the coating-steel interface nor accelerated degradation process of the coating. The more negative the applied CP potential, the more susceptible to SCC the enamel-coated steel.

ACKNOWLEDGMENTS

I would like to take this opportunity to express my sincere gratitude to Dr. Genda Chen for his advice and continuing support throughout the period of my Ph.D. study at Missouri University of Science and Technology (Missouri S&T). I feel privileged to work in such an opportunistic and vibrant research group and create a solid foundation for my professional growth. Thanks are due to the members of my Ph.D. Advisory Committee members, Dr. Lesley Sneed, Dr. Mohamed ElGawady, Dr. Hongyan Ma, and Dr. Richard K. Brow, for their valuable time and efforts to review my dissertation.

Financial support to complete this study was provided by Pipeline and Hazardous Materials Safety Administration (PHMSA) in the U.S. Department of Transportation under Award No. DTPH5615HCAP10. Special thanks are due to Dr. Fujian Tang for his technical training at the beginning of my Ph.D. study, and Dr. Signo Reis and Mr. Michael L. Koenigstein for their assistance in preparing enamel-coated steel specimens.

I appreciate many assistances from my fellow students, Yi Bao, Weina Meng, Yizheng Chen, Yan Tang, Chuanrui Guo, Zhaochao Li, Xingxing Zou, Le Teng, Yanping Zhu, and Abdullah Alhaj, and from laboratory technicians and specialists in Highbay Structures Laboratory, including Gary Abbott, Greg Leckrone, John Bullock, Brian Swift.

Finally, I wish to thank my parents, Lianxiang Fu and Ziyu Fan, and my brother Ming Fan for their love, encouragement and supports as always.

TABLE OF CONTENTS

Page

LIST OF ILLUSTRATIONS

Page

LIST OF TABLES

Page

1. INTRODUCTION

1.1. BACKGROUND

Natural gas, oil and hazardous liquid transmission and gathering pipelines have reached 484, 000 miles in the U.S. [1]. Despite the best effort made to ensure safe operations, over 10, 620 pipeline incidents occurred from 1994 to 2013, resulting in substantial property damage and significant injuries. These incidents were caused by natural forces (wind gusts, heavy rains/floods, lightening), excavations from third parties or operators, operation negligence, corrosion, and material defects. Among them, corrosion is the second to excavation for pipeline failure, accounting for 20% of the total incidents. According to the 2002 survey performed by the NACE International, the average corrosion-related annual cost for the U.S. pipeline operators to monitor, replace and maintain assets for both transmission and distribution services is over $12 billion. Therefore, corrosion problems and their impact on our nation's economy and prosperity cannot be treated light in any measure.

Metallic pipelines can be corroded both internally and externally. According to the statistical data released by the U.S. Department of Transportation Pipeline and Hazardous Materials Safety Administration (PHMSA), internal corrosion accounted for 74% of the significant corrosion related incidents in 2013. Several factors account for pipe internal corrosions, like chemical ingredients of the transported commodities, crude oil or gas flow rate, and operational temperature. For oil pipelines, water that is transported along with crude oils or carried by solid particles can drop out of the crude oil and become in contact with the pipe surface [2]. When water accumulates and persists on the pipe floor for an

extended period of time, internal corrosion happens. For gas pipelines, corrosion can take place when the internal surface is exposed to moisture and contaminants such as chlorides, CO_2, and sulfur compounds, forming electrolytes for electrochemical reactions [3]. Once internal corrosion happens, it will gradually reduce the pipeline wall thickness and mechanical strength, leading to severe pipeline leakage or rupture and posing tremendous threat to the surrounding community [4].

Porcelain enamel coating is proposed to protect hazardous liquid and natural gas pipelines from corrosion and provide them with a smooth finishing for flow efficiency. Enamel is chemically bonded to the surface of steel pipes. Once applied, enamel coating is inseparable from the pipes throughout their service life unless damage unexpectedly. The advantages of porcelain enamel, such as chemical bond, smoothness, chemical stability, and corrosion resistance, make it a promising substitution for epoxy coating in internal pipeline linings.

1.2. LITERATURE REVIEW ON STATE-OF-THE-ART DEVELOPMENT

1.2.1. Internal Coatings for Pipeline. To prevent internal corrosion, various measures can be taken during the design and operation of pipelines. For example, the quality of commodity can be controlled to minimize the chemical ingredients that cause or accelerate metal corrosion. Corrosion inhibitors can be added into transported liquids. Perhaps the most effective corrosion protective approach is to apply internal coatings on the surface of metal pipes since the internal coating can prevent fluid or gas from interacting and reacting with underlying steel. Besides, the coated steel pipes reduce microbiological deposits and bacteria biofilm formations since the higher surface

roughness of uncoated pipes helps shield the bacteria and provides growth conditions for bacterial colonies. In addition to corrosion prevention, internal coatings can improve the efficiency of hydraulic flow and thus reduce energy consumption during the transport of liquids. Internal coatings can also improve the resistance of the pipe to erosion and cavitation and facilitate cleaning and water disposal after the hydrostatic testing of pipelines [5].

Internal pipeline linings are commonly divided into three categories: concrete, rubber, and plastics. However, concrete can result in a smaller inside diameter and its roughness may not be desirable. Rubber-lined pipes are not oil, flame and abrasion resistant and susceptible to temperature change [6]. Plastic coating likely is the most popular physical barrier in corrosion protection of pipelines. To date, two-part solvent based epoxy coating, solvent free and fusion bonding coatings, polyethylene and polyurethane coatings, and glass flake filled polymeric resin coatings are the main plastic protective barriers to internal corrosion of gas pipelines [7-9]. However, the flowing abrasives in the transmission system can eventually abrade and roughen the surface of these softer organic lining materials and finally the build-up begins. Besides, organic coating materials tend to become brittle and separate or delaminated from the base metal because of the leaching or depletion of the oil from the lining materials, promoting under-film corrosion [10].

1.2.2. Enamel Coating. Porcelain enamel, as an inorganic material, is chemically bonded to the substrate metal by fusing glass frits at a temperature of 750 ℃~850℃. It has been widely used in industry and domestic applications to protect metals or alloys from corrosion, including chemical reactors, heat exchangers, food-processing vessels, and cookware. In addition to excellent chemical stability and good corrosion resistance,

porcelain enamel has excellent resistances to abrasion, heat, and mechanical and thermal shocks particularly in extreme wear and erosion applications [11].

The enamel coating can overcome the so-called under-film corrosion associated with epoxy coating. For the epoxy coating, once damaged, corrosion takes place on the surface of the exposed steel and further extends beneath the coating as clearly illustrated in Figure 1.1(a) [12]. The enamel coating, even when locally breached, is chemically bonded to its substrate and corrosion is limited to the breached area as shown in Figure 1.1(b) for coated bars in reinforcing concrete structures [12].

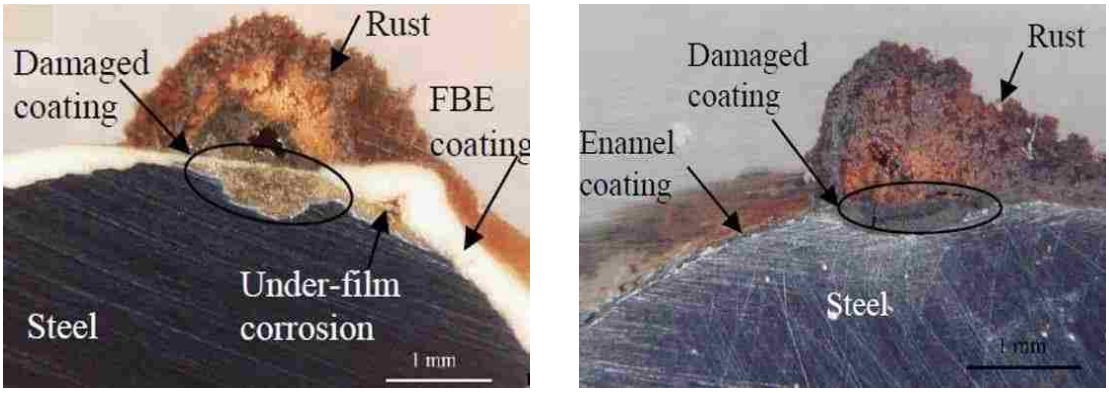

(a) (b)

Figure 1.1. Corrosion spreading in damaged areas for (a) the epoxy coating and (b) the enamel coating [12].

The surface of silica-based enamel coating can be extremely smooth. For example, the surface roughness of a 100~200 μm thick enamel slurry coating was averaged to be 1.3 μm with a standard deviation of 0.3 μm [13]. This value is significantly smaller than the surface roughness of various flow efficiency coatings, which ranges from 3.8 to 18.7 μm for a dry film of 61-140 μm in thickness [14].

1.2.2.1. Coating process. Enamel on steel can be done in several ways such as the wet process of enamel slurry, the plasma spray process of enamel powder, and the electrostatic process of enamel powder. Wet process requires little capital expenses and provides an acceptable finish for industrial applications particularly when the part to be coated is small. Plasma spraying process typically requires a significant capital investment and provides less smooth surface and a coating structure with micro-pores, columnar grains, and laminal splats, which is less effective in corrosion protection [15]. Electrostatic process is most promising to coat large pipelines in field conditions. Pipeline applications do not have the so-called Faraday-cage effect associated with deep recesses and channels of the part to be coated as observed in other applications. The enamel coating applied by the electrostatic process is very consistent and smooth but the charge retention is lowered in high humidity conditions.

The electrostatic process involves both powder spraying and heating steps. The powder is sucked from a fluidized bed container and pneumatically sent to a spray gun where a pointed electrode is applied with high (negative) voltage potential to create a highly non-uniform electric field between the gun and the ground pipe, as shown in Figure 1.2 [16]. The powder particles, exiting the gun, are charged in the electric field of corona discharge. The charged particles are attracted to and deposited on the surface of the grounded pipe. After an initial layer of particles is deposited on the pipe surface, the particles of subsequent layers (not in direct contact with the pipe) have to induce gradually increased mirror image charges due to the presence of the existing particles and eventually can no longer be deposited to the pipe surface due to back ionization. As a result, the outer layer of particles (farther away from the pipe wall) tends to be larger in size. The deposited

particles are fused at high temperature using an induction heater to form a thin coating to the pipe. The effects of powder particle size and shape on charging efficiency, coating formation, and back ionization are discussed by Guskov [16].

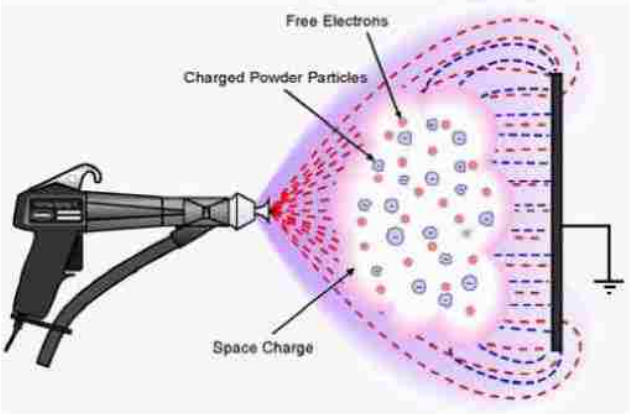

Figure 1.2. Non-uniform field [16].

Powder particles are glass frits that are coated with organic material to allow them (an insulator) charged electrostatically. Regardless of particle size, the so-called back ionization in electrostatic spraying determines a maximum number of charged particles that can be stacked on top of one another or the largest possible coating thickness. On the other hand, a minimum number of particles required to achieve a continuous coating determines the smallest possible coating thickness. In between, the coating thickness increases with the particle size. For pipeline applications, small particles such as 150 mesh grits are less grainy and flow more smoothly. If particles larger than 150 mesh grits are removed, the sifted enamel may adhere to the pipe without the need to hold agents before firing. However, the smaller particles of a sifted base coat have lower charges or weaker electric field formed with their mirror image in the steel. As such, the formation of multiple

layers of particles on the surface of the pipe (or coating thickness) becomes more difficult as a result of the back ionization effect near the pipe wall.

1.2.2.2. Previous application of enamel coating on steel bars. To date, previous studies have been limited to the wet coating process of enamel slurry and the coating application on reinforcing bars in concrete structures [12, 13, 17]. The metal oxides and water in enamel slurry, the iron and carbon in steel, and atmospheric oxygen are involved in chemical redox reactions to promote adhesion between the enamel coating and its substrate [13]. In the wet process of enamel slurry, gases such as CO_2, CO, H_2O and H_2 [10] were released when fired at 810°C for 10 minutes and left behind air bubbles/voids when cooled down [12]. Figure 1.3 shows the cross-sectional and surface morphologies of enamel coating on a steel plate [17]. It can be observed from Figure 1.3(a) that the coating is 250-300 um thick with isolated air bubbles. As shown in Figure 1.3(b), the enamel coating has a smooth and glassy surface but with a few pin-holes resulting from bubbles generated during the high-temperature chemical reaction.

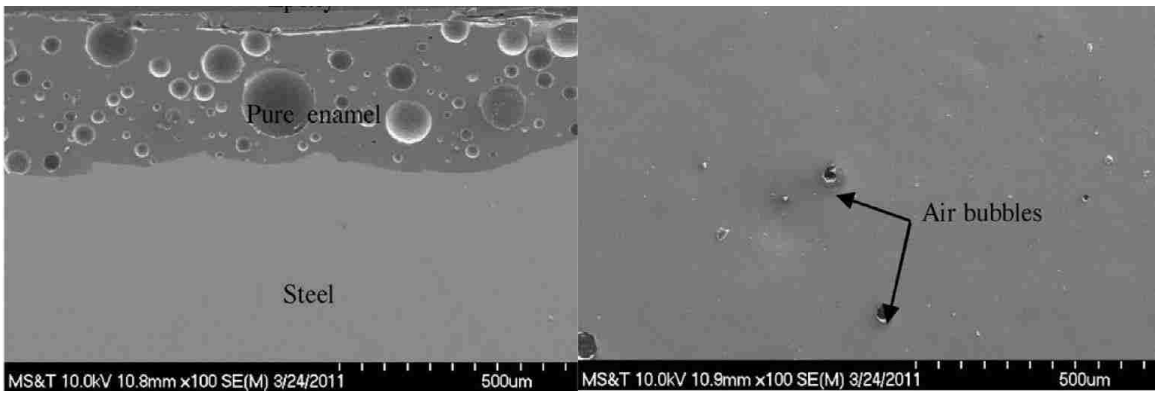

(a) (b)

Figure 1.3. SEM images of enamel coating: (a) cross-sectional view of enamel-coated steel, and (b) surface view of enamel coating [17].

Figure 1.4 shows the fracture surface of an enamel-coated steel plate after a pull-off test. The failure occurred inside the enamel coating cutting through air bubbles as illustrated in Figure 1.4(b). The pull-off cohesive strength was determined to be 7.87 MPa, which is in the same order as the adhesion strength between fusion bond epoxy (FBE) coating and its bonded plate [18].

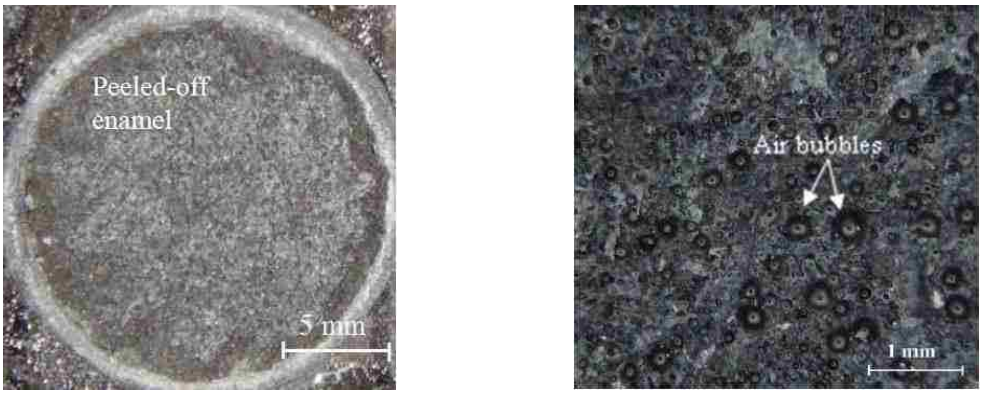

(a) (b)

Figure 1.4. Fracture surface of enamel coating (a) on a steel plate after a pull-off test; (b) of a magnified area [17].

The modulus of a complex impedance, Z, for intact and damaged samples are plotted as a function of frequency in Figure 1.5 [12], which is used to characterize the corrosion resistance of coating. It can be seen from Figure 1.5(a) that the intact FBE coating displays capacitive behavior since the modulus-frequency curve is a 45° straight line and the phase angle fluctuates around -90°. Therefore, the intact FBE coating is an effective corrosion barrier for steel rebar. However, the damaged FBE coating behaved quite differently. The impedance magnitude was reduced significantly from 10^6 to 0.1 MΩ at 0.005 Hz. The significant change in the impedance spectra was caused by the impact-induced damage that provided a pathway for chloride ions to penetrate through and resulted

in corrosion of the coated rebar in the NaCl solution. The impedance of intact enamel coated sample is 0.1 MΩ at 0.005 Hz, which is close to that of damaged epoxy coating as shown in Figure 1.5(b). Therefore, the corrosion resistance of intact enamel coating is much smaller than that of intact epoxy coating.

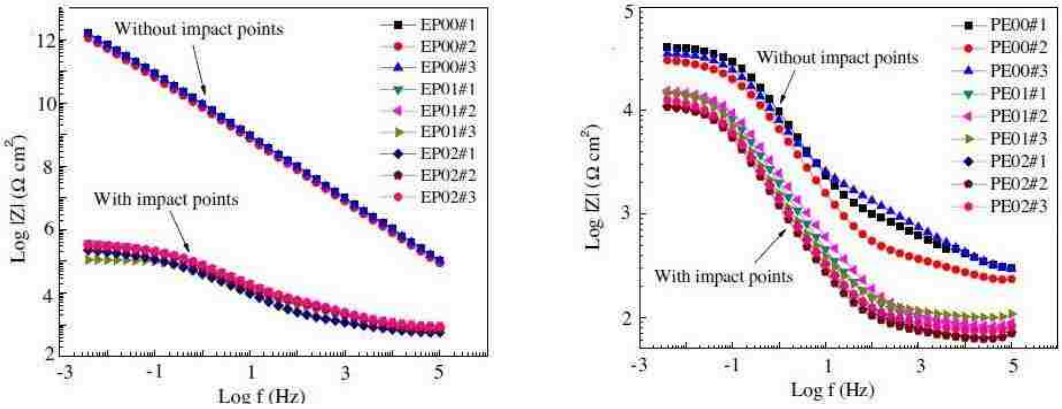

Figure 1.5. Impedance modulus of (a) FBE and (b) enamel-coated steel rebar immersed in 3.5 wt. % NaCl solution [12].

The cross-sectional elemental analysis was conducted on the enamel-coated bar after the corrosion test [12]. Figure 1.6 shows a scanning electron microscopy (SEM) image and its corresponding distribution mappings for Fe, Cl, and Si. The three mappings were used for corrosion detection, the detection of chloride ions, and the identification of enamel coating location and thickness. It can be observed from Figure 1.6 that no chloride ions were detected inside the enamel coating even though isolated pores were present. The Fe mapping was supported by the fact that little or no corrosion product was detected at the coating-steel interface. Therefore, the enamel coating is an effective physical barrier that successfully prevented chloride ions from penetration.

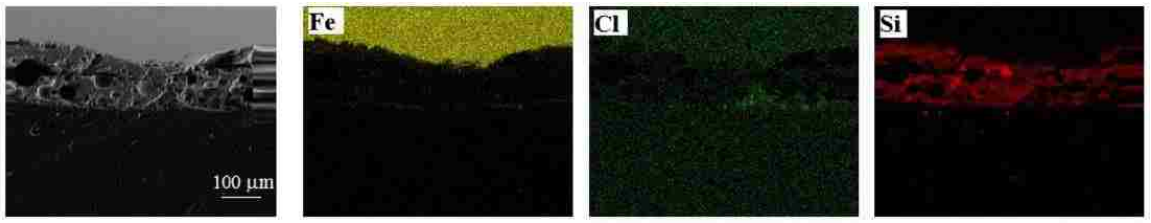

Figure 1.6. Elemental distribution maps after corrosion tests [12].

1.2.2.3. Practical solution and identified challenge of enamel coating application in pipelines. Further studies are needed for pipeline applications due to different steel compositions, geometries and shapes, different operational and environmental conditions, and different design objectives. Since the carbon content of structural steel in pipelines is smaller than that of reinforcement in concrete structures, it is easier to reduce the bubbles generated from CO_2 and CO, which can help eliminating or minimizing pin-holes on the enamel coating surface and reduce the surface roughness substantially. The reduced surface defects will substantially improve the corrosion resistance of enamel coating and the smoothness that is critical to reduce pressure loss along the length of a pipeline for cost effectiveness in liquid and natural gas transport. Therefore, densifying enamels or eliminating/minimizing air bubbles could be a major effort in the development of new enamel coating for pipeline application.

The wet process of enamel slurry may cause a non-uniform layer of coating due to gravity effect. For inside surface coating, the lighter enamel powder (than slurry) would be easier to remain in the crown area of pipe wall, and can reduce coating time due to no need for drying. In addition, coating a kilometer-long pipeline could be time consuming and costly. Therefore, the electrostatic process of enamel powder needs to be studied with the intent for pipeline applications.

When a coated pipe is transported to and handled at the installation site, the coating may be accidentally scratched. Cathodic protection (CP) can be used to prevent steel pipelines from corrosion at the damaged coating site. However, the effect of a CP makes the exposed metal surface strongly alkaline and causes the delamination of organic coating through hydrolysis process of the coating itself or the coating-substrate interface. Therefore, it is imperative to study the effect of CP in enamel-coated pipes in order to avoid cathodic delamination as observed in epoxy coating.

Unlike reinforced concrete structures, transmission pipelines are often embedded underground, externally exposed to soils with various microbes and internally exposed to pressurized liquids and natural gas with additives. Internal corrosion and stress corrosion cracking (SCC) could be a real issue to tackle in pipeline applications [19]. The external and internal pressure on enamel-coated pipes further compounds the thermal effect during enameling in the evaluation of potential SCC.

1.3. RESEARCH OBJECTIVES AND THE SCOPE OF WORK

The overarching goal of this study is to improve the corrosion protection and safety, and reduce the pressure loss and operation cost of hazardous liquid and natural gas pipelines. To achieve this goal, this study aims to explore and develop chemically-bonded enamel coating (200-300 um) on steel pipes for coating uniformity, low surface roughness, high coating efficiency and corrosion resistance. Both the mechanical and electrochemical properties of enamel-coated pipes will be characterized when exposed to soil and thermal environments. The coating uniformity will be measured from the optical images or SEM of coated samples. The surface roughness will be measured according to ASME B46.1-09

[20]. The wet process of enamel slurry will be compared with the electrostatic process of enamel powder to demonstrate their performances measured by coating uniformity, surface roughness, and efficiency (time). Their corrosion behaviors are systematically investigated and compared with that of epoxy-coated samples in 3.5 wt. % NaCl solution with open circuit potential, electrochemical impedance spectroscopy and potentiodynamic polarization tests. Their microstructures are examined with SEM to help interpret the electrochemical test results. The objectives will be established and evaluated both experimentally and numerically in the following seven research tasks:

1. Evaluate the thermal property, phase composition, microstructure, thickness, surface roughness and the strength of bond with steel of two types of enamel (e.g., enamel powder GP2118 from PEMCO and enamel slurry from Tomatec),
2. Investigate the short-term corrosion performance and mechanism of small coupon samples in 3.5 wt.% NaCl solution,
3. Investigate the long-term corrosion performance and mechanism of small coupon samples in 3.5 wt.% NaCl solution,
4. Investigate the performance of large enamel-coated samples using salt spray tests,
5. Investigate the corrosion resistance of steel pipes with damaged enamel coating and cathodic protection (CP),
6. Study the stress distribution in pipelines under thermal loading, internal pressure, and external pressure using finite element analysis, and
7. Study the stress corrosion cracking (SCC) of enameled pipe steel using electrochemical impedance spectroscopy (EIS) and slow strain rate tests.

The entire research plan in this study can be grouped into three phases. The first phase of this study in Task 1 is to characterize enamel coatings for the thickness, surface roughness, and thermal properties of coating, and the bond strength at the coating-steel interface. The second phase of this study in Tasks 2-5 is to quantify the corrosion performance and understand the corrosion mechanism of enamel-coated steel. The third phase of this study in Task 6-7 is to understand the stress distribution of enamel-coated steel pipes under thermal loading, external pressure, and internal pressure, and evaluate potential SCC in simulated corrosive environment.

1.4. ORGANIZATION OF THIS DISSERTATION

This dissertation consists of nine sections. Section 1 introduces the importance of this research in steel pipelines, literature reviews on related topics (e.g., protective coatings for pipelines, enamel coating application in steel reinforcement, coating methods, identified challenges of enamel coating application in pipelines), and the overall objectives and the scope of work in this study (seven tasks that will be addressed in the following seven chapters). In Section 2, enamel coatings are characterized for thermal properties, thickness, surface roughness, and bonding strength with steel substrate. In Section 3 and 4, the short- and long-term corrosion performances and mechanisms are investigated using small coupon samples in 3.5 wt.% NaCl solution. The main findings from the short- and long-term experimentations have been published in the Journal of Materials Engineering and Performance, and Corrosion (journal), respectively. In Section 5, the performance of large enamel-coated samples is characterized using salt spray tests. In Section 6, the corrosion resistance of steel pipes with damaged enamel coating and cathodic protection

are investigated using electrochemical tests. The main findings have been published in Coatings (journal). In Section 7, a finite element model of enamel-coated pipes under thermal loading, internal pressure, and external pressure is established and analyzed to understand stress distribution in the pipes. In Section 8, the SCC in enameled pipe steel in alkaline solution is studied using electrochemical impedance spectroscopy and slow strain rate tests. The main research findings from this study and future research needs are summarized in Section 9.

Sections 2-8 discuss all technical issues that are interrelated to achieve the objectives of this study. Their relationships can be mapped as delineated in a flow chart in Figure 1.7.

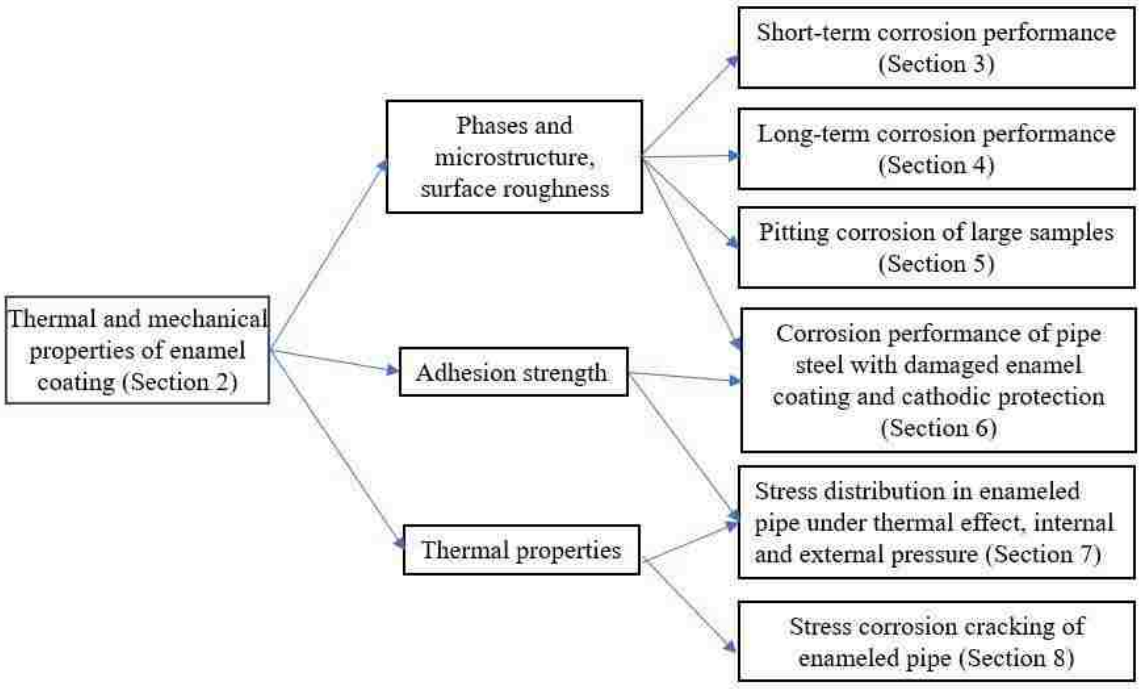

Figure 1.7. Flow chart for the relationship between sections.

2. THERMAL AND MECHANICAL PROPERTIES OF ENAMEL COATINGS

2.1. BACKGROUND

Enamel is a silica glass obtained by fusion at high temperature between 1000°C and 1300°C. In its original state, enamel cannot be used due to high melting point, low coefficient of thermal expansion, and no adhesion to steel. To ensure the durability of enameled parts, silica glass is modified with three main groups of additives in pipeline applications: refractories, fluxes, and adhesion agents. Refractories such as alumina can increase enamel resistance to temperature, chemicals and abrasions. Fluxes such as borax and alkaline oxides have a lower melting point than silica and can thus increase the coefficient of thermal expansion by filling "voids" in the silica structures. Adhesion agents such as titanium, manganese, and barium oxides are involved in chemical oxidation-reduction reactions with iron and carbon in steel and atmospheric oxygen. The wet process of enamel slurry may cause a non-uniform layer of coating under gravity effect. In the case of inside coating in pipelines, the lighter enamel powder (than slurry) would be easier to remain in the crown area of pipe wall under the gravity effect. Furthermore, slurry coating involves drying process that could be time consuming and costly in kilometer-long pipelines. Therefore, the electrostatic process of enamel powder is a practical solution in pipeline applications. This study is focused on the evaluation of the thermal properties, phase composition, microstructure, thickness, surface roughness and the strength of bond with steel of two types of enamel. The first type of enamel powder from PEMCO will be applied on steel samples in a dry electrostatic process. The second type of enamel slurry from Tomatec will be coated on steel samples in a wet spraying process.

2.2. EXPERIMENTAL PROCEDURE

2.2.1. Materials and Specimens. An API 5L X65 steel pipe (MRC Global) with an outside diameter of 323.850 mm and a wall thickness of 9.525 mm was used in this study. The chemical composition and mechanical properties of the steel pipe are given in Table 2.1 and Table 2.2, respectively. Two types of enamel: Tomatec slurry and GP2118 powder were studied. The chemical compound of Tomatec glass frits and GP2118 enamel powder were determined by X-ray fluorescence (XRF) and presented in Table 2.3.

Table 2.1. Chemical composition of steel pipe.

Element	C	Mn	P	S	Si	Cu	Ni	Cr	Mo	Al	V	Fe
Wt.%	0.17	1.15	0.07	0.02	0.26	0.10	0.04	0.07	0.07	0.02	0.02	98

Table 2.2. Mechanical properties of steel pipe.

Grade	Yield Strength (MPa)	Ultimate Strength (MPa)	Yield/Ultimate Strength Ratio	Elongation %
API 5L X65	482	551	0.875	38.2

Table 2.3. Chemical compounds of borosilicate glass Tomatec and GP-2118 (wt.%).

Elements	SiO_2	B_2O_3	Na_2O	CaO	MnO_2	Al_2O_3	TiO_2	K_2O	Fe_2O_3	MgO	BaO	Others
Tomatec	60.3	12.84	7.20	2.37	5.37	4.49	0.14	2.12	3.48	0.17	1.47	0.05
GP2118	57.5	16.95	9.60	3.31	4.70	1.02	1.41	3.63	1.49	0.21	0.04	0.14

2.2.2. Thermal Properties. The thermal properties of glasses Tomatec and GP2118, such as the glass transition temperature (T_g), softening temperature (T_s), and the coefficient of thermal expansion (CTE) were determined using Orton automatic recording dilatometer (model 1500). Three samples of each coating were prepared and tested to understand the variation of test data. The samples of glass enamel were prepared by melting

glass powder in alumina crucibles in air at 1250 °C for 1 h. The melted sample was quenched in air by pouring it into a cylindrical steel mold with a diameter of 1.4 cm and a height of 2.6 cm. The samples were transferred into a furnace and annealed at 450 °C for 4 h. Dilatometric analysis was then performed in flowing synthetic air at a heating rate of 10 °C/min. The steel pipe was first cut into 9 mm × 9 mm × 20 mm coupon specimens. Dilatometric analysis was then performed in flowing inert gas at a heating rate of 10 °C/min.

2.2.3. Enameling Process. The steel pipe was first cut into 25 mm×50 mm coupon specimens. The cut specimens were then steel blasted for 1 min to get rid of mill scale and rusts, and finally cleansed with a commercially available cleansing solvent.

Tomatec slurry and GP2118 powder were applied on the steel coupons as shown in Figure 2.1. The enamel slurry was prepared by first milling glass frits, clay and certain electrolytes, and then mixing them with water until the mixture is in a stable suspension state. The water, glass frits, and clay were mixed in a proportion of 1.00: 2.40: 0.17 by weight. The enamel slurry was manually sprayed on coupon specimens using a spray gun, which was powered by a jet of compressed air as specified in Table 2.4. The specimens were heated at 150 °C for 10 min. to drive off moisture, fired at 815°C for 10 min, and finally cooled to room temperature. For electrostatic spraying, the GP2118 enamel powder with an average particle size of 32.8 um was used. An electric field was formed between a nozzle electrode and the sample. Enamel particles, propelled out of the spray gun by a stream of air, became negatively charged, migrated towards the sample (positive electrode) and were deposited. After power spraying, the steel coupons were moved into a furnace, fired at 843 °C for 10 min, moved out of the furnace, and cooled down to room temperature.

The thickness of the Tomatec coating was controlled by the spraying time while the thickness of the GP2118 coating was controlled by the number of spray guns.

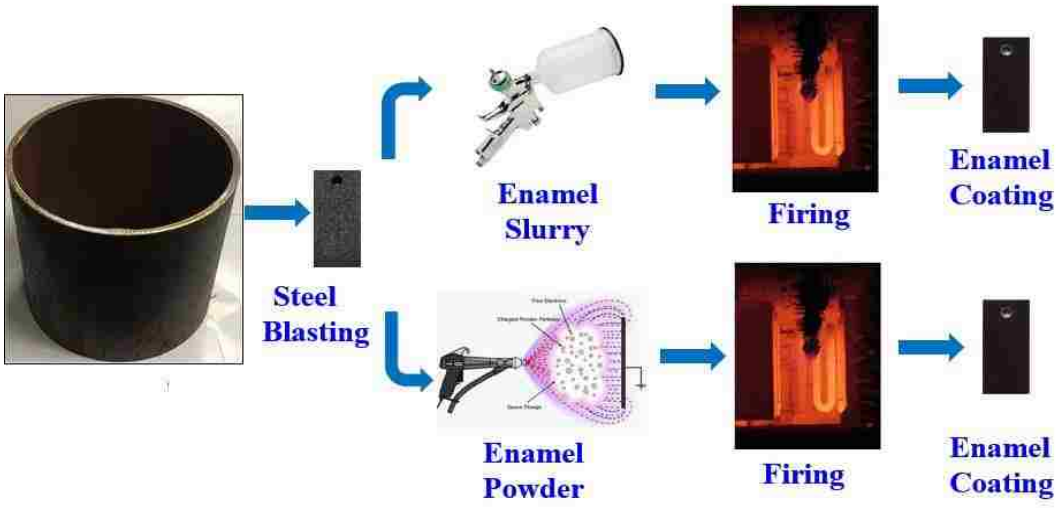

Figure 2.1. Wet vs. electrostatic spraying process of enamel coating.

Table 2.4. Coating parameters.

Coating application parameters	Wet spaying	Electrostatic (dry) spraying
Chain speed (m/min)	-	12FPM
Voltage (kV)	-	80KV
Atomization pressure	3.5	0.65
Slip throughput per guns	0.6	0.35
Number of guns	1	12
Distance gun to work piece (cm)	40	50
Transfer efficiency (%)	40	60-80

2.2.4. Phases in Enamel. The phases in enamel coating were examined directly on the surface of coated steel samples by X-ray diffraction (XRD, Philip X' Pert) with a diffraction angle (2θ) varied between 10° and 55°.

2.2.5. Microstructure at the Enamel-Substrate Interface. Cross sections of the enamel-coated samples were prepared to examine the enamel microstructure and investigate the elemental analysis of the coatings with scanning electron microscopy (SEM, Hitachi S-4700, Tokyo) coupled with an energy-dispersive X-ray spectroscopy (EDS). Each enamel-coated sample was cold-mounted in epoxy resin (EpoxyMount, Allied High Tech Products, Inc.), and cut into a 10-mm thick cross section using a diamond saw. The 10-mm thick slices were then abraded with silicon carbide papers with grits of 80, 180, 320, 600, 800, and 1200. After abrading, all samples were rinsed with deionized water and dried at room temperature prior to SEM imaging. ImageJ was used to calculate the porosity of each coating. The porosity is defined as the ratio between the bubble area and the entire area of a SEM image.

2.2.6. Coating Thickness, Surface Roughness, and Adhesion Strength. The coating thickness and roughness were measured with a coating thickness gauge MiniTest 6008 and optical microscope Hirox, respectively. The bond strength between the coating and its substrate steel were determined using PosiTest following the ASTM D4541-09 [21]. To enhance its bond with the coating, a 20-mm-diameter dolly at its base was roughened with abrasive papers and cleansed with alcohol to remove oxidation and contaminants. The base of the dolly was adhered with a uniform layer of glue to the test coating surface. After curing for 24 h, the coating around the dolly was removed using a 20-mm cutting tool in order to isolate the dolly on a specific test area. The dolly was finally pulled off the sample surface perpendicularly at a stress rate of 0.4 MPa/s. The maximum strength of each coated sample was recorded. For comparison, epoxy-coated steel samples were prepared and tested. In this case, 3M Scotchkote 323 epoxy, which was often used in pipeline industry,

was used to coat the samples. Steel coupons were coated by brushing epoxy at room temperature and then dried in air for three days prior to bond strength tests.

2.3. RESULTS AND DISCUSSION

2.3.1. Thermal Properties. Figure 2.2 shows the thermal elongation in the longitudinal direction of the two glass coatings and steel as a function of temperature. The steel has a measured CTE of 19.7 ppm/℃ while the glass coatings Tomatec and GP2118 have a measured CTE of 13.0ppm/℃ and 10.9 ppm/℃, respectively. The CTE of the steel remains constant over a temperature range of 100 to 600℃, while the CTE of the glass coatings is constant only over a range of 200 to 400℃. The CTE difference between the steel and glass coatings will generate compressive stress on the coatings during cooling, which is desirable. The glasses Tomatec and GP2118 have a similar glass transition temperature ($\boldsymbol{T_g}$) and softening temperature ($\boldsymbol{T_s}$). That is, $\mathbf{506} \leq \boldsymbol{T_g} \leq \mathbf{552}$°C and $\mathbf{578} \leq \boldsymbol{T_s} \leq \mathbf{616}$°C for both types of enamel.

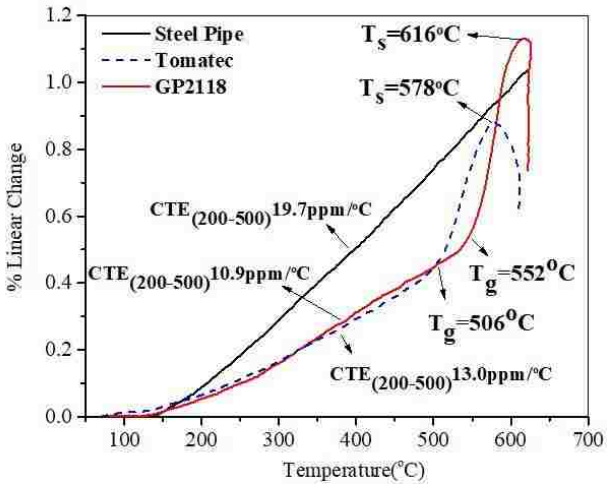

Figure 2.2. Thermal properties of two coatings and steel measured with Orton dilatometer.

2.3.2. Phases in Enamel. XRD patterns on the surface of GP2118 and Tomatec enamel-coated samples are identified and displayed in Figure 2.3. Quartz SiO_2 is present in both types of enamel coatings. The highest intensity peaks of quartz SiO_2 were at 26° and 26.5° for GP2118 and Tomatec enamels, respectively.

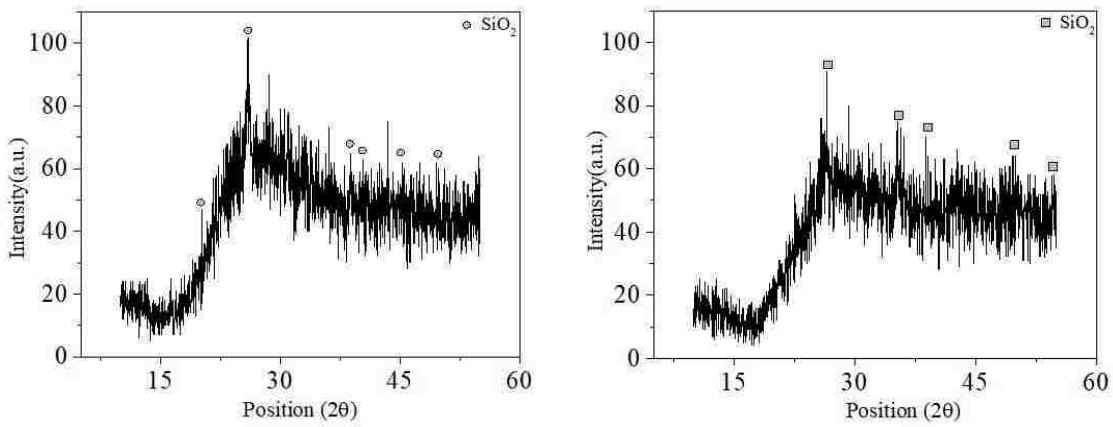

(a) (b)

Figure 2.3. XRD patterns for enamel coating: (a) GP2118, and (b) Tomatec.

2.3.3. Microstructure at the Enamel-Substrate Interface. Cross-sectional SEM images and representative EDS analyses of enamel-coated steel samples are presented in Figure 2.4. EDS analyses were performed on the coating sample taken within the small white square in the respective SEM images. GP2118 enamel coating of approximately 180 μm in thickness as shown in Figure 2.4(a-1) has an amorphous structure with a few isolated air bubbles corresponding to a porosity of 3.51%. The largest air bubble is 41 μm in diameter. The magnified interface layer as shown in Figure 2.4(a-2) shows the extensive formation of an island-like structure in the enamel coating, reinforcing interfacial bond [9]. EDS analysis as shown in Figure 2.4(a-3) indicates that the principal components in the

coating include silicon (Si), sodium (Na), manganese (Mn), potassium (K), calcium (Ca), iron (Fe), titanium (Ti), and aluminum (Al). Boron, a major component of the glass frit, could not be detected by the EDS system due to its light weight. The Tomatec slurry enamel coating as shown in Figure 2.4(b-1) is approximately 235 μm thick and has a porosity of 6.57%. It has more but smaller air bubbles than the powder enamel coating. Figure 2.4(b-2) also shows anchor points growing into the coating, indicating strong chemical bond at the enamel-steel interface. EDS analysis in Figure 2.4(b-3) indicates that silicon (Si), sodium (Na), manganese (Mn), aluminum (Al), iron (Fe), calcium (Ca), potassium (K), and barium (Ba) are the detected principal components. Once again, EDS analysis could not detect boron in the slurry enamel coating. The air bubbles in the coating were formed in the enameling process by entrapped gases such as H_2, CO, and CO_2. During the firing process, the dissolved oxygen reacted with carbons in the steel, releasing gaseous CO/CO_2. The atomic hydrogen diffused into the steel to form hydrogen gas (H_2). In the cooling process, the gas H_2, CO, and CO_2 were no longer able to escape since the gases were entrapped in the solidified enamel [9, 10].

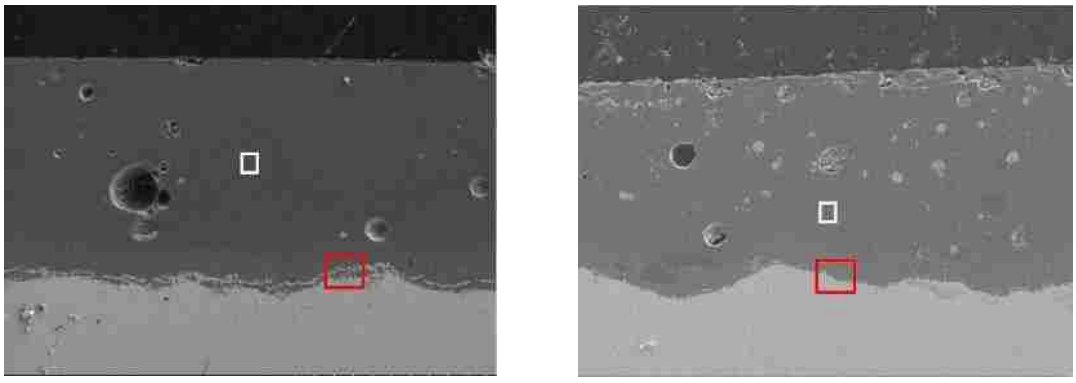

(a-1) (b-1)

Figure 2.4. Cross-sectional SEM images and EDS analysis of (a-1, a-2, a-3) GP2118 enamel-coated sample and (b-1, b-2, b-3) Tomatec enamel-coated sample with different magnifications: (a-1) 250×, (a-2) 2500×, (b-1) 250× and (b-2) 2500×.

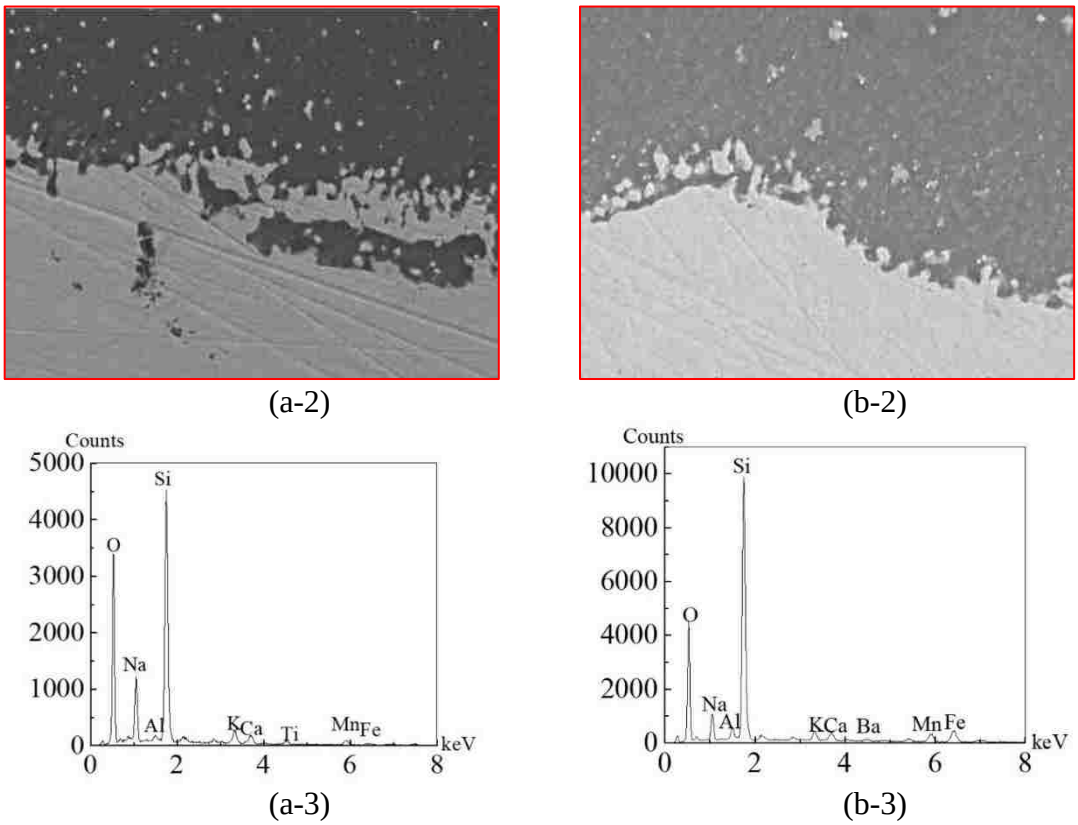

Figure 2.4. Cross-sectional SEM images and EDS analysis of (a-1, a-2, a-3) GP2118 enamel-coated sample and (b-1, b-2, b-3) Tomatec enamel-coated sample with different magnifications: (a-1) 250×, (a-2) 2500×, (b-1) 250× and (b-2) 2500× (cont.).

2.3.4. Coating Thickness, Surface Roughness, and Adhesion Strength. The measured thickness, surface roughness, and bond strength of three types of coatings are summarized in Table 2.5. The average and the standard deviation of the thickness and surface roughness of each coating were calculated from 27 measurements taken from three different samples. The average and the standard deviation of the bond strength of each coating were calculated from the three pull-off tests conducted. It can be seen from Table 2.5 that epoxy coating is the thickest (396 µm) and Tomatec enamel coating is the thinnest (230 µm). The roughness of the three coatings is approximately 1 µm, indicating smooth surfaces in all specimens.

Table 2.5. Coating thickness, surface roughness, and adhesion strength.

Coating	Thickness (μm)	Roughness (μm)	Bond strength (MPa)	Failure mode
GP2118	340±23	1.05±0.33	17.89±0.84	Mixed
Tomatec	230±8	0.85±0.15	16.85±0.73	Mixed
Epoxy	396±45	0.86±0.06	8.01±2.06	Mixed

At the completion of pull-off tests, the dolly and substrate fracture surfaces are shown in Figure 2.5. In a pull-off bond test, there are four possible failure modes including: (1) adhesion break between the coating and its steel substrate; (2) cohesion break within the coating layer; (3) glue break; and (4) mixed break or a combination of the above breaks at multiple locations [22].

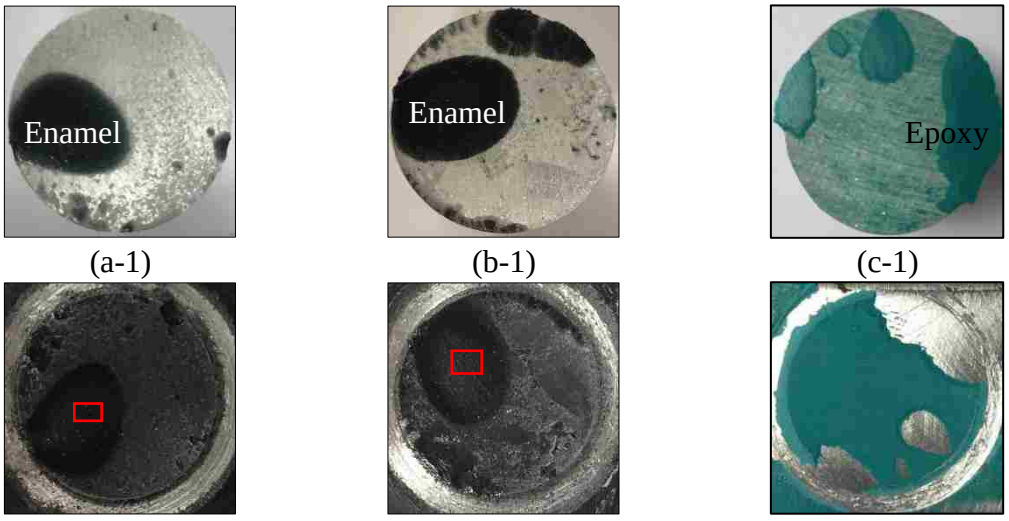

Figure 2.5. Fracture surface morphologies of steel coupons coated with (a) GP2118 enamel, (b) Tomatec enamel, and (c) epoxy: (1) dolly and (2) steel coupons.

Enamel coatings have a mixed failure mode involving a break inside the coating (cohesive break) and a break in glue used to bond the dolly to the specimen. Epoxy coating

also has a mixed failure mode involving a break inside the coating (cohesive break), a break between the coating and the substrate steel (adhesive break), and a glue break. There are no adhesive breaks for enamel coatings since the anchor points on the interface increase the bonding between an enamel coating and its substrate steel as shown in Figure 2.4. Specifically, GP2118 enamel coating has the highest bond strength with an average value of 17.89 MPa, epoxy coating has the lowest bond strength of 8.01 MPa, and Tomatec enamel coating has a bond strength of 16.85 MPa.

Figure 2.6(a) and Figure 2.6(b) represent the magnified fracture surface morphologies of the tested specimens in rectangular areas as shown in Figure 2.5(a-2) and Figure 2.5(b-2), respectively. When the dolly was pulled off the coated specimen at right angle, a crack initiated and propagated across large air bubbles within the coating under increasing loads.

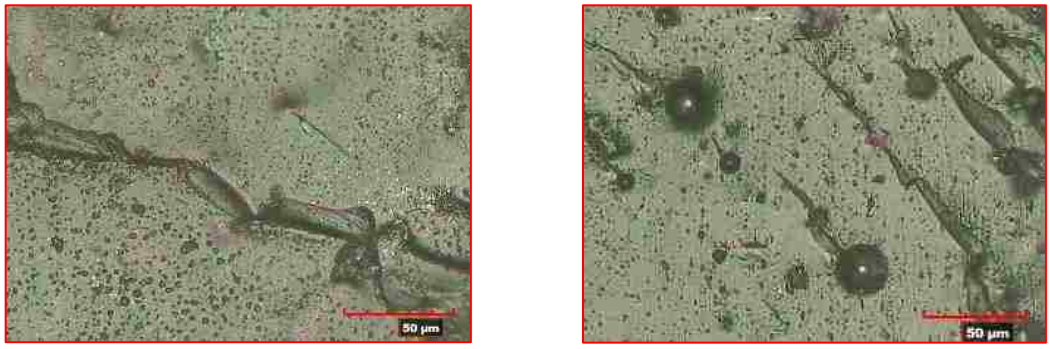

(a) (b)

Figure 2.6. Magnified fracture surface morphologies of (a) GP2118 enamel in Figure 2.5 (a-2) and Tomatec enamel in Figure 2.5(b-2).

Figure 2.7(a) and Figure 2.7(b) show SEM images for the cross sections of the tested specimens in rectangular areas of Figure 2.5(a-2) and Figure 2.5(b-2), respectively. The fracture surfaces of the specimens are generally smooth with the minimum remained

coating thicknesses of approximately 70 μm and 40 μm for GP2118 and Tomatec enamels, respectively. In comparison with Figure 2.4, Figure 2.7(a) and Figure 2.7(b) indicate that the fracture surfaces are far away from their corresponding bonding layers at the enamel-substrate interfaces and pass through the weakest layer connecting large air bubbles in the coating since the adherence of enamel on steel surfaces is chemically strengthened with the growth of epitaxial spinel particles in the enamel during chemical reaction in the firing process [9].

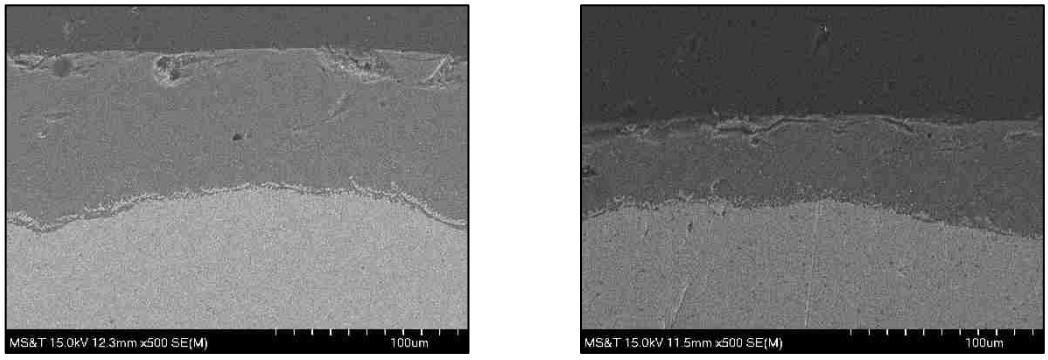

(a) (b)

Figure 2.7. SEM images for the cross sections of remained GP2118 and Tomatec enamel coatings in rectangular areas of Figure 2.5(a-2) and Figure 2.5(b-2).

2.4. SUMMARY

The enameling process, thermal properties, thickness, and surface roughness of two types of enamel coatings, and the bond strength between a coating and its substrate steel were characterized in detail. Based on the test data and analysis, the following conclusions can be drawn:

1. Enamel coating has an amorphous structure with no crystalline phase observed. Only Quartz SiO_2 is present in both types of enamel coatings.

2. The CTE difference between the steel and glass coatings will generate a compressive stress on the coatings during cooling, which is desirable to prevent cracking of the enamel coatings under normal conditions.
3. The powder and slurry enamel coatings are 180 μm and 235 μm thick, corresponding to a porosity content of 3.51% and 6.57%, respectively. The powder enamel coating contains fewer but larger isolated air bubbles than the slurry enamel coating. Both coatings cope well with small iron protrusions, which ensure strong bonding between the coatings and their substrate steel.
4. The enamel coatings applied on steel pipe samples failed in a mixed mode of break inside the coating layer and detachment of the glue from a test dolly. They showed no adhesive break since small Fe protrusions grew into the coatings to form anchor points at the enamel-steel interface. In addition to the breaks in enamel coating, the epoxy coating may also fail at the coating-steel interface due to weak bonding.

3. SHORT-TERM CORROSION PERFORMANCE OF SMALL COUPON SAMPLES IN 3.5 WT. % NACL SOLUTION

3.1. BACKGROUND

Internal corrosion can reduce the wall thickness and load capacity of metal pipes, leading to potential leakage or rupture of pipelines under internal and/or external pressures [23]. Internal corrosion is affected by the chemical ingredients of transported commodities, crude oil or gas flow rate, and operation temperature. To prevent internal corrosion, various measures can be taken during the design and operation of pipelines. For example, the quality of commodity can be controlled to minimize the chemical ingredients that cause or accelerate metal corrosion. Corrosion inhibitors can be added into transported liquids. Perhaps the most effective corrosion protective approach is to apply internal coatings on the surface of metal pipes. In addition to corrosion prevention, internal coatings can reduce the surface roughness of metal pipes, which improves the efficiency of hydraulic flow and thus reduces energy consumption during the transport of liquids. Epoxy lining is vulnerable to cathodic disbondment with metal pipes. Porcelain enamel, as an inorganic material, is chemically bonded to the substrate metal by fusing glass frits at a temperature of 750℃ ~850℃. It has been widely used in industry and domestic applications to protect metals or alloys from corrosion, including chemical reactors, heat exchangers, food-processing vessels, and cookware. In addition to excellent chemical stability and good corrosion resistance, porcelain enamel has excellent resistances to abrasion, heat, and mechanical and thermal shocks particularly in extreme wear and erosion applications [11]. This study aims to select and characterize new enamel coatings so that their corrosion resistances are competitive to the widely-used epoxy coating in specified applications. Two types of

enamel coatings are applied on steel samples in electrostatic and wet spraying processes. Their corrosion behaviors are systematically investigated and compared with that of epoxy-coated samples in 3.5 wt. % NaCl solution with open circuit potential, electrochemical impedance spectroscopy and potentiodynamic polarization tests. Their microstructures are examined with scanning electron microscopy to help interpret electrochemical test results.

3.2. EXPERIMENTAL PROCEDURE

3.2.1. Materials and Specimens. An API 5L X65 steel pipe (MRC Global Inc.) was selected as a substrate material due to its wide applications in pipeline industry. The pipe is 323.850 mm in outer diameter and 9.525 mm in wall thickness. Prior to coating, a full-size pipe was cut into 12 coupon samples (25 mm × 50 mm). The samples were then annealed in a muffle furnace at 850 °C for 2 hours for de-carburation pretreatment. Once taken out of the furnace, all the samples were steel blasted for 1 min, and cleansed with a commercially available cleansing solvent. Steel coupon samples were coated with enamel powder (PEMCO Product) in a dry process and with enamel slurry (Tomatec Product) in a wet process. For repeatability, three samples were prepared with each coating condition. They are designated as P-1, P-2 and P-3 for enamel powder GP2118, and S-1, S-2, and S-3 for enamel slurry Tomatec. For comparison, three uncoated (UN-1, UN-2, and UN-3) and three epoxy-coated (EP-1,EP-2, and EP-3) steel samples were also prepared and tested. The 3M Scotchkote 323 two-part epoxy, which is designed to help protect pipe steel from corrosion, was brushed to the surface of each sample at room temperature and dried in air for 3 days prior to electrochemical tests. The applied coating has a coating thickness of 400 μm, a surface roughness of 0.92 μm, and a pull-off strength of 10 MPa.

3.2.2. Coating Characterization. Cross sections of enamel-coated samples were prepared after corrosion tests to examine the enamel microstructure and investigate the elemental analysis of the coatings with scanning electron microscopy (SEM, Hitachi S-4700, Tokyo) coupled with an energy-dispersive X-ray spectroscopy (EDS). Each enamel-coated sample was cold-mounted in epoxy resin (EpoxyMount, Allied High Tech Products, Inc.), and cut into a 10-mm thick cross section using a diamond saw. The 10-mm thick slices were then abraded with silicon carbide papers with grits of 80, 180, 320, 600, 800, and 1200. After abrading, all samples were rinsed with deionized water and dried at room temperature prior to SEM imaging. ImageJ was used to calculate the porosity of each coating. The porosity is defined to be the ratio between the bubble area and the entire area of a SEM image.

3.2.3. Corrosion Tests. To prepare for electrochemical tests, a copper wire was electrically connected to each sample. All sides of a sample except the enamel- or epoxy-coated surface were covered with Marine epoxy (LOCTITE) to force any electrochemical reaction through the coating surface. The exposed enamel or epoxy coating area was 30 mm by 20 mm in size as shown in Figure 3.1.

For corrosion tests, all samples were immersed in 3.5 wt.% NaCl solution (Fisher Scientific, Inc.), which was prepared by adding purified sodium chloride into distilled water. Steel samples were tested at room temperature with a typical three-electrode setup, including a 25.4 mm×25.4 mm×0.254 mm platinum sheet as the counter electrode, a saturated calomel electrode (SCE) as the reference electrode, and the coated steel coupon as a working electrode. All three electrodes were connected to an Interface1000E Potentiostat (Gamry Instrument) for data acquisition. The open circuit potentials (OCPs)

of the samples were recorded for 1 hour immediately after the samples had been immersed in the solution. Electrochemical impedance spectroscopy (EIS) data were sampled at ten points per decade around the OCP (E_{ocp}) with a sinusoidal wave of 10 mV in amplitude and frequency ranging from 100 kHz to 5 mHz. After the EIS tests, potentiodynamic polarization (PP) tests were conducted from E_{ocp} *-300* mV to E_{ocp} *+1500* mV with a scanning rate of 5.0 mV/s.

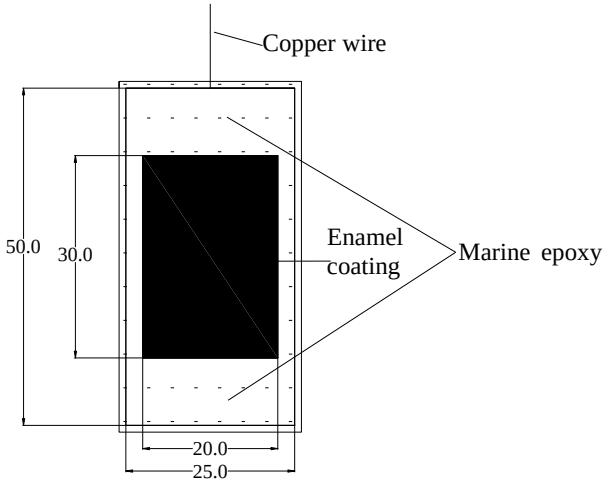

Figure 3.1. Test sample dimension (unit: mm).

3.3. RESULTS AND DISCUSSION

3.3.1. OCP Tests. OCP represents the potential between the working electrode and the reference electrode when no external potential is applied to the test system. Figure 3.2 presents the OCPs of uncoated, enamel- and epoxy-coated steel samples after 1 hour of immersion. The variation in OCP among three identical uncoated samples is much smaller than that of the enamel- and epoxy-coated samples. The average OCP of three uncoated steel samples shows a gradually decreasing trend from the beginning of -0.39 V to the end

of -0.48 V. The average OCPs of the powder and slurry enamel-coated samples increase rapidly in the first 500 seconds due to the capacitive charging of enamel coating and then slowly approach to an asymptotical value of 0.88 V and 0.4 V, respectively. The OCP changing trend of three epoxy-coated samples are inconsistent. However, the OCP of each sample after 1 hour of immersion remains positive with an average value of 0.2 V. Compared with the uncoated steel samples, the enamel- and epoxy-coated samples have higher positive OCP values, thus superior barrier effects to the penetration of electrolyte through the open pores or localized defects and protection of the steel substrate.

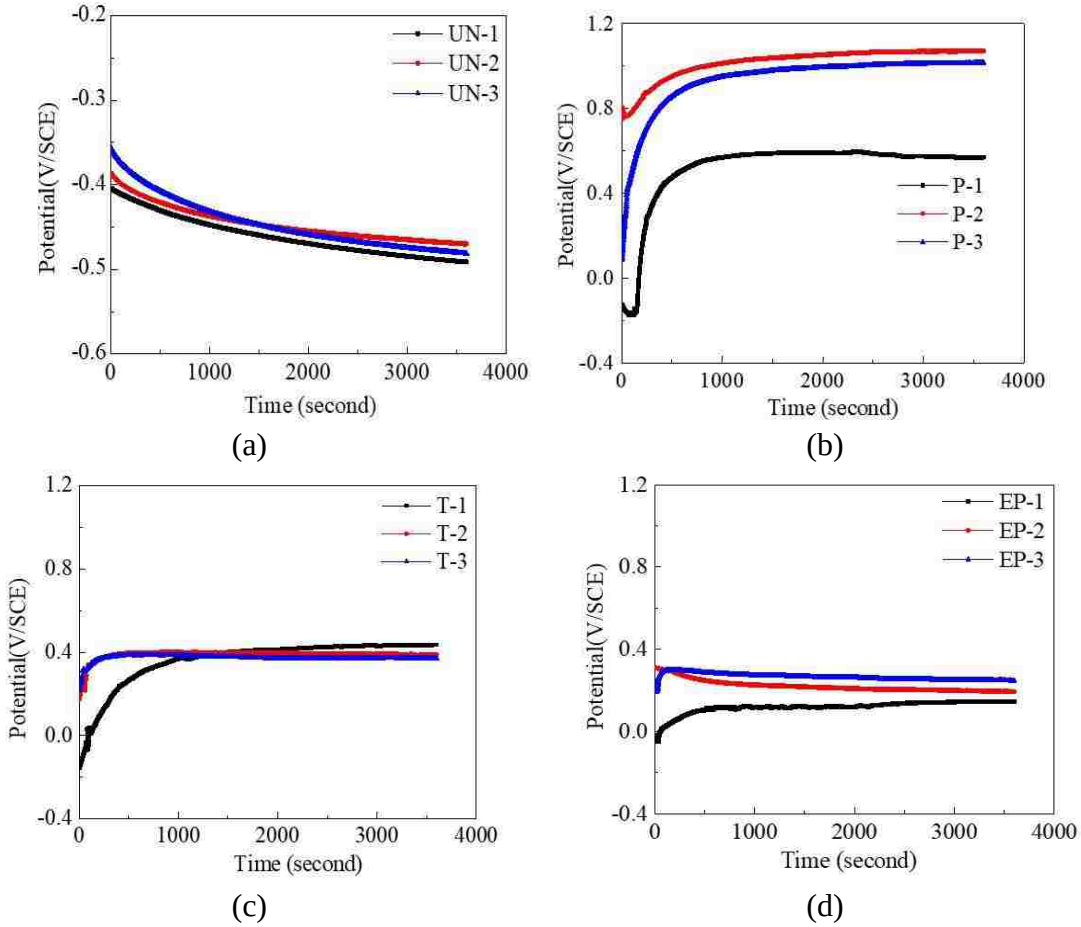

Figure 3.2. The OCPs of various samples in 3.5 wt% NaCl solution: (a) uncoated, (b) GP2118 enamel-coated, (c) Tomatec enamel-coated (d) epoxy-coated steel samples.

3.3.2. EIS Tests. The electrochemical impedances of uncoated, enamel and epoxy coated samples are presented in the format of Bode plots in Figure 3.3. In the Bode diagrams, the impedances and phase angles among the three identical samples with each coating are quite consistent. The impedance diagrams of enamel- and epoxy-coated samples show a 45° slope in a log-log scale while those of the uncoated samples start with a slope of larger than 45° at low frequency and gradually decrease to 0° at high frequency. The impedances of all the enamel- and epoxy-coated samples at a frequency of 0.005 Hz are approximately 4×10^{10} Ω cm^2. Although relatively low due to potential coating defects, the impedances are 10^9 times higher than those of the uncoated samples. In addition, the phase angles of the enamel- and epoxy-coated samples approach to 90° at high frequency while those of the uncoated samples are close to 0°. The phase angle diagrams confirm that both the enamel and epoxy coatings provide high resistances to the penetration of electrolyte and thus satisfactory corrosion protection [24].

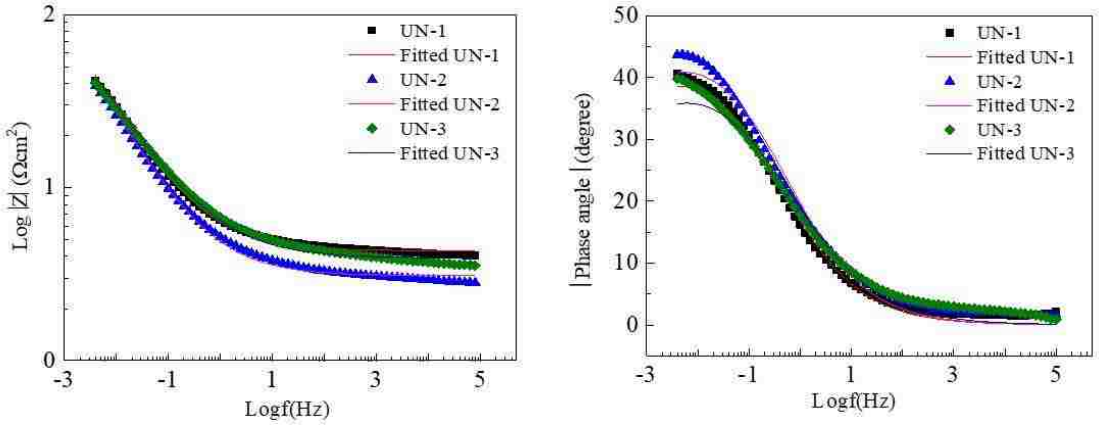

(a-1) (a-2)

Figure 3.3. EIS diagrams (1 and 2: Bode plot) for: (a) uncoated, (b) GP2118 enamel-coated, (c) Tomatec enamel-coated (d) epoxy-coated steel samples.

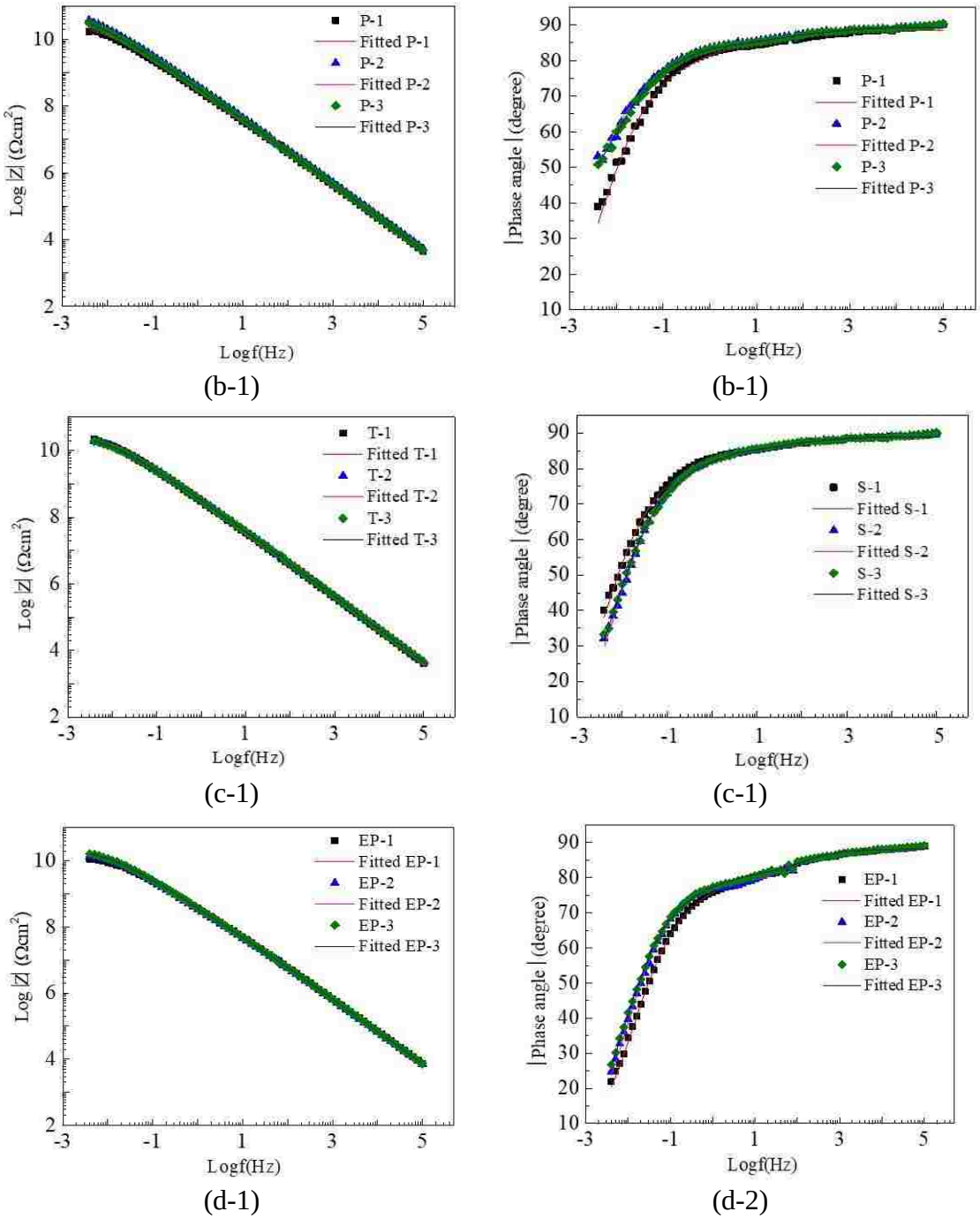

Figure 3.3. EIS diagrams (1 and 2: Bode plot) for: (a) uncoated, (b) GP2118 enamel-coated, (c) Tomatec enamel-coated (d) epoxy-coated steel samples (cont.).

Two electrical equivalent circuit (EEC) models were chosen to fit the experimental data [25, 26] as illustrated in Figure 3.4. Models (a) and (b) were used to simulate the

uncoated and coated samples, respectively. In the two models, R_s represents the solution resistance, R_c and R_{ct} represent the pore resistance of coating and the charge transfer resistance at the steel-electrolyte interface, respectively, and CPE_c and CPE_{dl} represent the contribution of coating capacitance and double layer capacitance to the total impedance, respectively. CPE_c and CPE_{dl} were used to replace pure capacitances because of the non-homogeneity in coating thickness and roughness [27, 28] and a distribution of electrochemical reactivity on the substrate steel, respectively [29]. The impedance of a CPE is defined by two parameters Y and n, and its impedance is represented by:

$$Z_{CPE} = Y^{-1}(jw)^{-n} \tag{3.1}$$

where Y is a CPE constant, ω is the angular frequency, and n ($0 \leq n \leq 1$) is an index that represents the deviation from a pure capacitor [30]. The CPE resembles a pure capacitor when n =1 and a resistor when n=0. The effective capacitance based on the two CPE parameters can be obtained by [31-32]:

$$C = Y^{1/n} R^{(1-n)/n} \tag{3.2}$$

where parameters R_c, Y_c, n_c are used to calculate the effective capacitance of enamel coatings C_c, and R_{ct}, Y_{dl}, n_{dl} are used to calculate the effective capacitance of double layer C_{dl}.

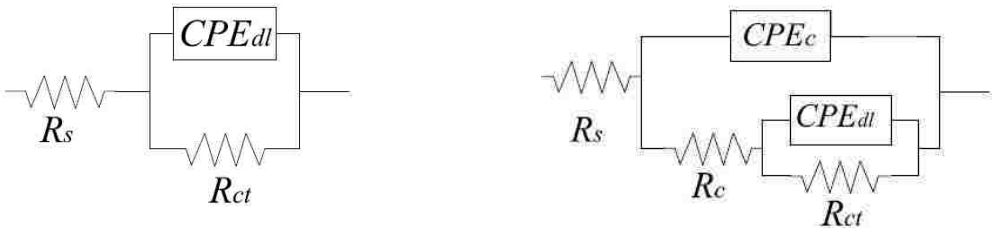

(a) (b)

Figure 3.4. EEC models for: (a) uncoated, (b) GP2118 enamel-coated, Tomatec enamel-coated and epoxy-coated samples.

The solid lines in Figure 3.3 represent curve fitting of the EEC models while the dotted points symbolize the experimental data. For the uncoated samples, there is only one time constant corresponding to the electrochemical reaction at the steel-electrolyte interface. For the enamel- and epoxy-coated samples, there are indeed two time constants, which correspond to the electrochemical reaction at the steel-electrolyte interface and the dielectric properties of coatings [30, 33]. In the Bode plots, the two time constants are not easily identifiable since they are overlapped [34].

ZSimpWin was used to determine the parameters of two EEC models based on the EIS data recorded. The chi-squared values were in the order of 10^{-4} to 10^{-3} for all the samples, indicating a satisfactory fitting of the two proposed EEC models. The parameters obtained from curve fitting are listed in Table 3.1.

Table 3.1. EEC parameters obtained by fitting into experimental data.

	Y_c (Ω-sec^n/cm^2)	n_c	R_c ($\Omega\ cm^2$)	C_c (F/cm^2)	Y_{dl} (Ω-sec^n/cm^2)	n_{dl}	R_{ct} ($\Omega\ cm^2$)	C_{dl} (F/cm^2)
P-1	4.26×10^{-10}	0.98	2.56×10^{7}	3.96×10^{-10}	2.24×10^{-10}	0.65	3.22×10^{10}	6.57×10^{-10}
P-2	3.38×10^{-10}	0.99	4.72×10^{7}	3.22×10^{-10}	1.38×10^{-10}	0.63	4.84×10^{10}	4.24×10^{-10}
P-3	3.71×10^{-10}	0.99	2.71×10^{7}	3.57×10^{-10}	1.70×10^{-10}	0.69	4.44×10^{10}	4.23×10^{-10}
S-1	4.58×10^{-10}	0.99	4.37×10^{7}	4.36×10^{-10}	2.01×10^{-10}	0.64	3.99×10^{10}	6.43×10^{-10}
S-2	4.21×10^{-10}	0.99	3.40×10^{7}	4.00×10^{-10}	2.06×10^{-10}	0.63	2.94×10^{10}	5.80×10^{-10}
S-3	4.06×10^{-10}	0.99	3.54×10^{7}	3.84×10^{-10}	1.88×10^{-10}	0.64	2.87×10^{10}	4.87×10^{-10}
EP-1	2.84×10^{-10}	0.98	3.42×10^{7}	2.56×10^{-10}	3.09×10^{-10}	0.67	1.46×10^{10}	6.40×10^{-10}
EP-2	3.12×10^{-10}	0.98	6.39×10^{7}	2.83×10^{-10}	3.11×10^{-10}	0.71	1.83×10^{10}	6.29×10^{-10}
EP-3	2.91×10^{-10}	0.98	3.78×10^{7}	2.64×10^{-10}	2.79×10^{-10}	0.69	2.26×10^{10}	6.34×10^{-10}
UN-1	-	-	-	-	0.15	0.52	386	6.54
UN-2	-	-	-	-	0.17	0.53	422	7.31
UN-3	-	-	-	-	0.13	0.49	337	7.56

In general, the pore resistance represents the ability of coating to resist the penetration of electrolyte solution while the coating capacitance indicates the ease of electrolyte diffusion into the coating. Both parameters are closely related to the dielectric property and microstructure of the coating [17, 35]. As shown in Table 3.1, the pore resistances of all the enamel- and epoxy-coated samples are between 10^7 and 10^8 Ω cm^2. The coating capacitances for all the enamel- and epoxy-coated samples range from 10^{-10} to 10^{-9} F/cm^2. The large pore resistance and small coating capacitance indicate that both the enamel and epoxy coatings are strong barriers against the penetration and diffusion of electrolyte. The index n_c of all the coatings are close to 1, which means that the coatings behave like pure capacitors.

The corrosion rate at the metal surface is inversely proportional to the charge transfer resistance (R_{ct}) of the metal sample, which is an indication of how easy electrons can transfer across the metal surface [17, 37]. Among all the samples tested, the uncoated steel samples have the lowest charge transfer resistance of 381±42 Ω cm^2. The charge transfer resistances of all the coated samples range from 10^{10} to 10^{11} Ω cm^2, which is approximately 10^8 times larger than those of the uncoated samples. The double layer capacitance (C_{dl}) is also a measure of the ease of charge transfer across the interface between the substrate steel and electrolyte. The double layer capacitances of all the coated samples (10^{-10} - 10^{-9} F/cm^2) are approximately 10^{10} times smaller than those (7.14±0.53 F/cm^2) of the uncoated samples. The substantially higher charge transfer resistance and lower double layer capacitance of the enamel- and epoxy-coated samples clearly demonstrate their superior performance in resisting the transfer of electrons across the metal surface.

3.3.3. PP Tests. Potentiodynamic polarization plots of the uncoated, enamel-coated and epoxy-coated samples immersed in 3.5 wt.% NaCl solution are presented in Figure 3.5 to illustrate the overall kinetics of the corrosion process. It can be seen from Figure 3.5 that the anodic portion of polarization curves for all the samples tested show the same changing trend although some fluctuations can be observed from the uncoated steel samples. The fluctuations are likely because the existing rusts or corrosion products formed on the surface of uncoated steel samples affect the diffusion of oxygen and water molecule [37].

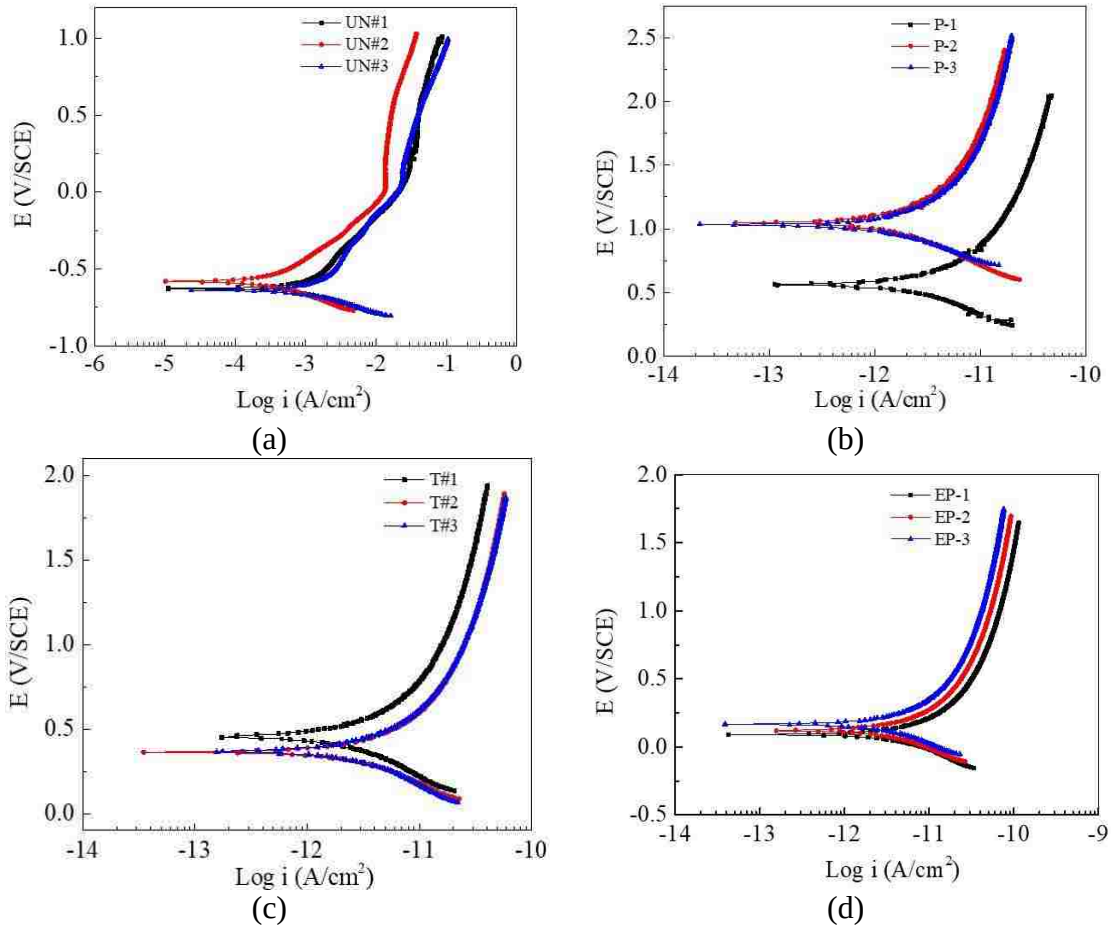

Figure 3.5. Potentiodynamic polarization curves for: (a) uncoated, (b) GP2118 enamel-coated, (c) Tomatec enamel-coated and (d) epoxy-coated steel samples.

The corrosion potential (E_{corr}) and corrosion current density derived from the potentiodynamic polarization plots are presented in Figure 3.6. These bar charts show the average plus/minus one standard deviation of each electrochemical parameter from the tests of three identical samples.

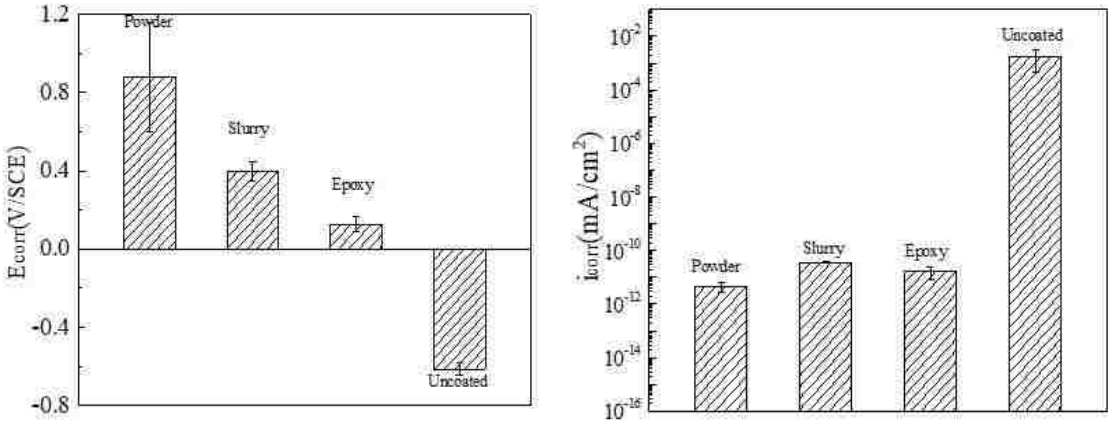

(a) (b)

Figure 3.6. Electrochemical parameters extracted from potentiodynamic polarization curves: (a) corrosion potential and (b) corrosion current density.

The corrosion potentials of all the enamel- and epoxy-coated samples are positive with the highest value of 0.88 V for the powder enamel coating while those of the uncoated samples are negative with an average value of -0.62 V. The corrosion potentials of powder and slurry enamel-coated samples as shown in Figure 3.6(a) are consistent with the OCPs as displayed in Figure 3.2. The corrosion potentials of the uncoated and epoxy-coated samples are smaller than their OCPs. The uncoated and epoxy-coated samples are thus more susceptible to the disturbance of charging currents than the enamel-coated samples. This is because the changing polarization leads to a continuous variation of the charging current density stored at the substrate-electrolyte interface and the potentiodynamic

polarization curve is easily distorted around the corrosion potential where the charging current is hard to be separated directly from the small faradaic current [38]. The average corrosion currents of all the enamel- and epoxy-coated samples are around 10^{-12} A, which are about 10^{9} times smaller than that of the uncoated samples. Thus, all the coatings can protect the substrate metal from corrosion.

3.3.4. Coating Characterization after Corrosion Tests. Cross-sectional SEM images and representative EDS analyses of enamel-coated steel samples after corrosion tests are presented in Figure 3.7. Compared with the SEM images and EDS analyses before corrosion tests in Figure 2.4, the coating microstructure, bonding interface between the coating and steel, and principal components remain basically the same in powder and slurry enamel coatings. The sodium content changes little and chloride is not detected by EDS analyses. Therefore, the electrolyte did not penetrate through the coatings during corrosion tests, and the enamel coatings are effective barriers to protect substrate steel from corrosion.

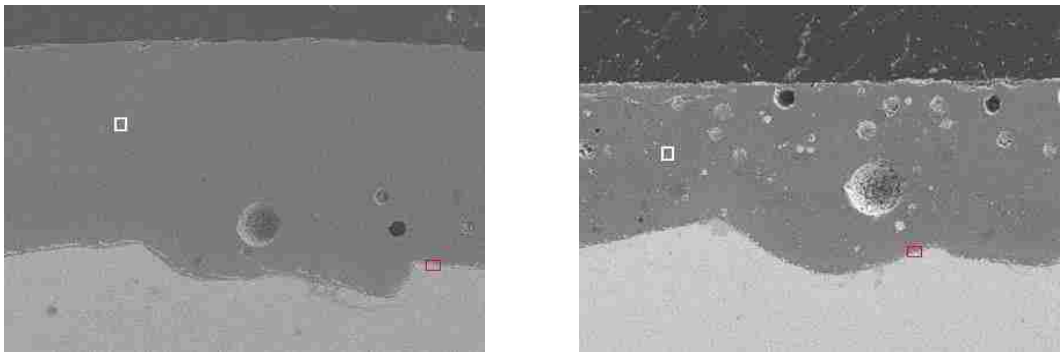

(a-1) (b-1)

Figure 3.7. Cross-sectional SEM images and EDS analysis of (a-1, a-2, a-3) GP2218 enamel-coated sample and (b-1, b-2, b-3) Tomatec enamel-coated sample after corrosion tests with different magnifications: (a-1) 250×, (a-2) 2500×, (b-1) 250× and (b-2) 2500×.

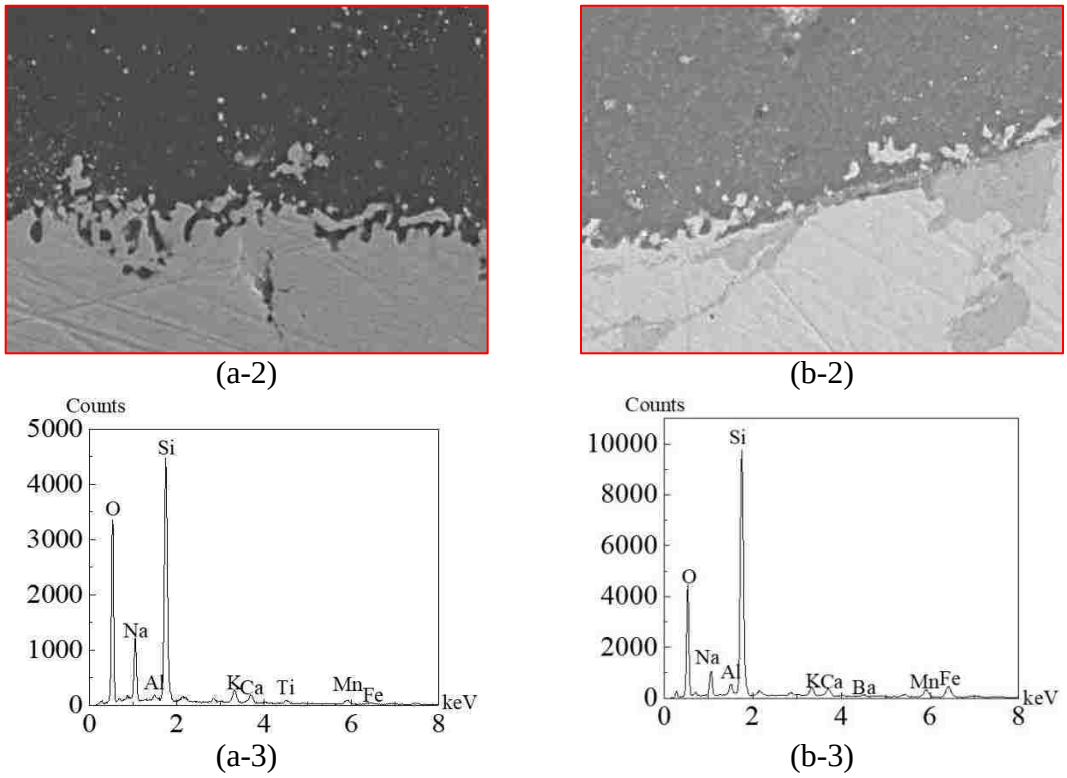

Figure 3.7. Cross-sectional SEM images and EDS analysis of (a-1, a-2, a-3) GP2218 enamel-coated sample and (b-1, b-2, b-3) Tomatec enamel-coated sample after corrosion tests with different magnifications: (a-1) 250×, (a-2) 2500×, (b-1) 250× and (b-2) 2500× (cont.).

3.4. SUMMARY

In this study, the microstructure and corrosion resistance of GP2118 and Tomatec enamel-coated and epoxy-coated samples have been investigated. Based on the test results and analysis, the following conclusions can be drawn:

1. The open circuit potentials of three uncoated steel samples decreased to an average value of -0.48 V after 1 hour of immersion in 3.5wt.% NaCl solution while those of the enamel- and epoxy-coated samples are positive. This comparison implies that both the enamel and epoxy coatings behave like a barrier for corrosion protection.

2. EIS tests showed that the impedances of both enamel- and epoxy-coated samples at a low frequency of 5 mHz were approximately 10 GΩ cm^2, and the phase angles at high frequency approached to 90°. These results demonstrate that these coatings provided excellent corrosion protection for the substrate steel.
3. Potentiodynamic polarization tests showed that all the enamel- and epoxy-coated samples had a positive corrosion potential and a significantly lower corrosion current than the uncoated samples.
4. Comparison of the SEM images and EDS analyses of two enamel-coated steel samples before and after corrosion tests shows nearly the same coating microstructure and the same enamel-steel interface with no presence of chloride. Therefore, the electrolyte did not penetrate through either the powder or slurry enamel coating during corrosion tests, both effectively protecting substrate steel from corrosion.
5. The powder enamel coating applied through the electrostatic spray process has a smoother surface and higher corrosion resistance than the slurry enamel coating. In addition, the electrostatic process requires less coating time and is thus a practical solution in pipeline field applications.

4. LONG-TERM CORROSION PERFORMANCE OF SMALL COUPON SAMPLES IN 3.5 WT. % NACL SOLUTION

4.1. BACKGROUND

Natural gas, oil and hazardous liquid transmission and gathering pipelines have reached 484,000 miles in the U.S. [1]. Aging pipelines face with reduced service life and reliability due to corrosion. They can be protected from corrosion by protective coating, cathodic protection, and use of corrosion inhibitors. Coating as a physical barrier to electrolyte penetration is one of the most effective and efficient methods in corrosion mitigation.

When internally applied to steel pipelines, coating has several advantages. First, the internal coating can prevent fluid or gas production from interacting and reacting with underlying steel. Second, the coated steel pipes reduce microbiological deposits and bacteria biofilm formations since the higher surface roughness of uncoated pipes help shield the bacteria and provide growth conditions for bacterial colonies [39]. Third and last, the internal coating can reduce pressure drop over a long distance of a pipeline and thus power required to transmit oil and gas. The pressure drop in coated pipes was experimentally demonstrated to be 31% lower than that in bare steel pipes at a Reynolds number of 1×10^7 [40]. Today, two-part solvent based epoxy coatings, solvent free and fusion bonded coatings, and polyamide coatings are widely used in crude oil and natural gas pipelines [41-43]. These coatings are weakly bonded with their steel substrate and thus prone to under-film corrosion [44].

Porcelain enamel, as an inorganic material, is chemically bonded to substrate metals at a temperature of 750 °C~850 °C. It can not only be finished with a smooth and aesthetical

surface, but also provide excellent chemical stability, good corrosion resistance, and durability in various harsh environments [11]. Unlike epoxy coating, enamel coating has no under-film corrosion when locally breached due to its chemical bond with metal substrates [12]. It has been widely used for household cooking utensil protection or steel container protection in industries. Its corrosion resistance as a protective coating for steel reinforcement in concrete structures has been investigated in previous studies and demonstrated to be satisfactory in general [26, 45].

In this study, the corrosion behavior of steel pipes internally coated with two types of enamel (Tomatec slurry and GP2118 powder) was examined in 3.5wt.% NaCl solution. The microstructure of enamels was characterized with scanning electron microscopy (SEM). The electrochemical behaviors were studied with open-circuit potential (OCP), linear polarization resistance (LPR), and electrochemical impedance spectroscopy (EIS) tests. Visual inspections were made on tested samples for any obvious signs of corrosion. The corrosion resistance of enamel-coated steel is compared with that of epoxy-coated steel.

4.2. EXPERIMENTAL PROCEDURE

4.2.1. Materials and Specimens. An API 5L X65 steel pipe (MRC Global) with 323.85 mm in outer diameter and 9.53 mm in wall thickness was used as substrate metal in this study. The steel pipe was first cut into 18 25 mm×50 mm coupon specimens.

The cut specimens were then steel blasted for 1 min to get rid of mill scale and rusts, and finally cleansed with a commercially available cleansing solvent. Two types of enamel were applied on the steel coupons: Tomatec slurry and GP2118 powder. For

comparison, epoxy-coated steel samples were prepared and tested. In this case, 3M Scotchkote 323 epoxy, which was applied in pipeline industry, was used to coat the samples. Steel coupons were coated by brushing epoxy at room temperature and then dried in air for three days prior to electrochemical tests.

4.2.2. Coating Characterization. Cross-sections of the enamel-coated samples were prepared for microstructure analysis with a scanning electron microscopy (SEM, Hitachi S4700). Each enamel-coated sample was first cold mounted in epoxy resin (EpoxyMount, Allied High Tech Products, Inc.) and cut into a 10 mm-thick cross section using a diamond saw. Then, the cross section was abraded with carbide papers to 1200 grit, rinsed with deionized water, and finally dried in air at room temperature prior to examination. SEM images were analyzed with ImageJ software for porosity evaluation.

4.2.3. Electrochemical Tests. Each sample was soldered with a copper wire for electrochemical measurements as illustrated in Figure 4.1. All sides of the sample except the enamel- or epoxy-coated face were covered with Marine epoxy. The exposed enamel or epoxy area was 30 mm by 20 mm in size.

All samples were immersed in 3.5 wt.% NaCl solution and tested at room temperature for 69 days. The solution was prepared by adding purified sodium chloride (Fisher Scientific, Inc.) into distilled water. At the time of 1, 3, 6, 13, 27, 41, 55, and 69 days, open circuit potential (OCP), linear polarization resistance (LPR), and electrochemical impedance spectroscopy (EIS) tests were carried out to monitor the corrosion evolution of the enamel- and epoxy- coated steel samples. A standard three-electrode system was used for electrochemical tests, including a 25.4 mm × 25.4 mm × 0.254 mm platinum sheet as a counter electrode, saturated calomel electrode (SCE) as a

reference electrode, and the coated sample as a working electrode. All three electrodes were connected to a Gamry, 1000E Potentiostat/Galvanostat for data acquisition.

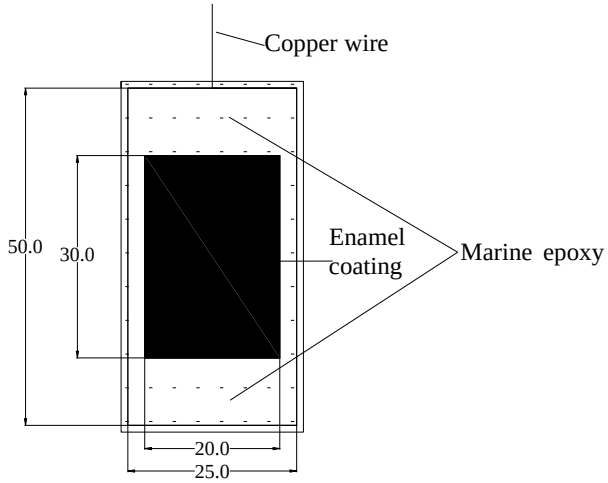

Figure 4.1. Test sample dimension (unit: mm).

After each stable OCP was recorded, an EIS test was performed with a sinusoidal potential wave of 10 mV in amplitude around the OCP and a frequency of 100 kHz to 5 mHz. The LPR test was conducted by scanning a range of $\pm$15 mV around the OCP at a scan rate of 0.167 mV/s. The LPR curves are used to determine the polarization resistance R_p, which is equal to the slope of the linear region of a polarization curve around zero current [46]:

$$R_p = \Delta E / \Delta i \tag{4.1}$$

where ΔE and Δi represent the voltage and current increments, respectively, in the linear portion of the polarization curve at i=0. LPR measurements were used to calculate the corrosion current density by the Stern-Geary equation [46]:

$$i_{corr} = \beta_a \beta_c / [2.303(\beta_a + \beta_c) R_p] \quad (4.2)$$

where β_a and β_c represent the anodic Tafel constant and the cathodic Tafel constant, respectively, and i_{corr} is the corrosion current.

4.3. RESULTS AND DISCUSSION

4.3.1. Microstructure at Enamel-Substrate Interface. Cross-sectional SEM images at the steel-coating interface with different magnifications are presented in Figure 4.2. The enamel coatings have a solid structure with disconnected air bubbles through the coating thickness (Figure 4.2 a-1 and Figure 4.2 b-1).

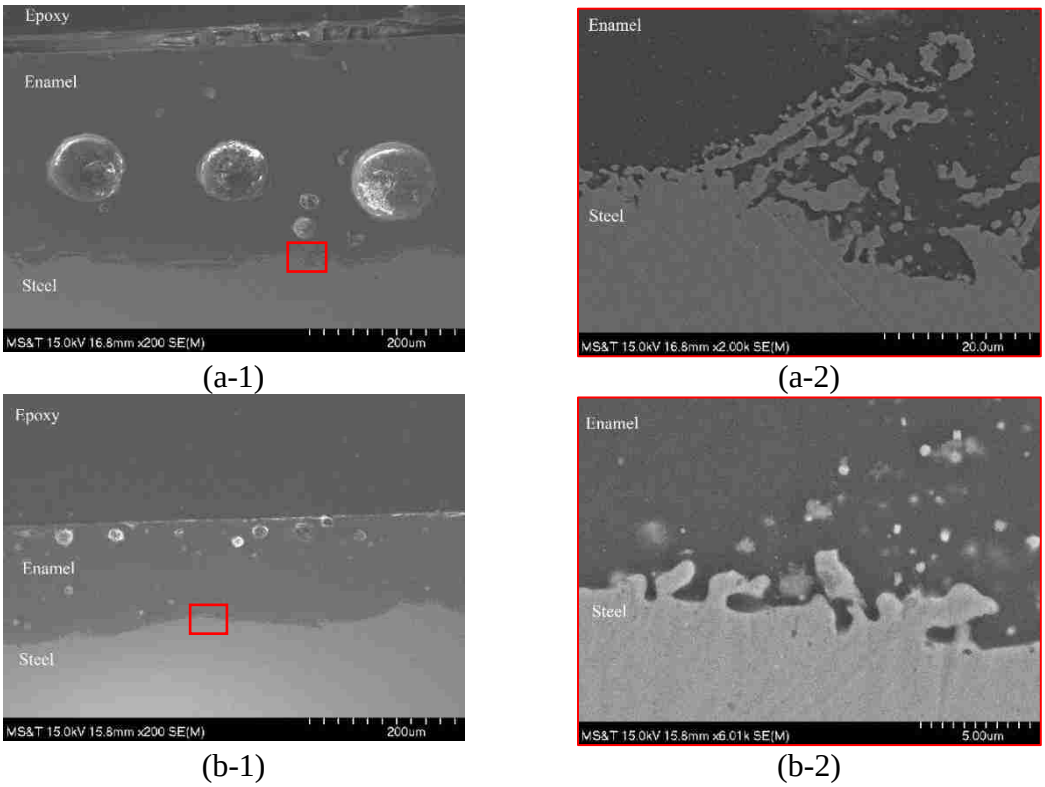

Figure 4.2. Cross-sectional SEM images of (a) GP2118, and (b) Tomatec with different magnifications: (a-1) 200×, and (a-2) 2k×, (b-1) 200×, (b-2) 6k×.

The air bubbles were formed during the high-temperature chemical reaction of the enamel glass frit with the steel during firing process [10, 25]. The enamel coatings have numerous isolated small pores with the exception of GP2118 enamel that has a few large pores with a diameter of approximately 105 μm. The porosity content of Tomatec enamel was measured to be 4.26%, which is lower than 12.72% for the GP2118 enamel. Figure 4.2 a-2 and Figure 4.2 b-2 show the magnified enamel-steel interfaces at which small-Fe protrusions grow into the enamel coating to form various anchor points. These epitaxial spinel particles improve the bonding between the enamel and its steel substrate [9].

4.3.2. Corrosion Potential and Resistance. Three Tomatec enamel-coated, three GP2118 enamel-coated, and three epoxy-coated specimens were tested in 3.5 wt.% NaCl solution up to 69 days. The OCP, LPR, and EIS values were recorded at different times. The average and standard deviation of three measurements for each type of coating were calculated over time.

4.3.2.1. OCP. Figure 4.3 presents the average ± standard deviation of OCP values when each coated sample was immersed in the sodium chloride solution up to 69 days. In general, the variation of three data points for each test coating is large in the first 6 days and reduced afterward. The average OCP values of the GP2118 and Tomatec enamel-coated samples decrease significantly in the first 13 days, and then approach an asymptotic value of –0.25 V/SCE and –0.3 V/SCE, respectively. The average OCP of the epoxy-coated samples decreases dramatically in the first 6 days, and gradually approaches –0.32 V/SCE. According to ASTM C876 [47], the GP2118 enamel-coated samples with their OCPs in between –127 mVSCE and –276 mVSCE were likely not corroded with uncertain probability. The Tomatec enamel- and epoxy-coated samples with their OCPs less than –

276 mVSCE were likely corroded with over 90% probability. The initial rapid drop of OCP values as displayed in Figure 4.3 was a result of the penetration of electrolyte through the defects in coating. As corrosion products formed over time gradually clogged the defects, the corrosion process decelerated and became stabilized eventually.

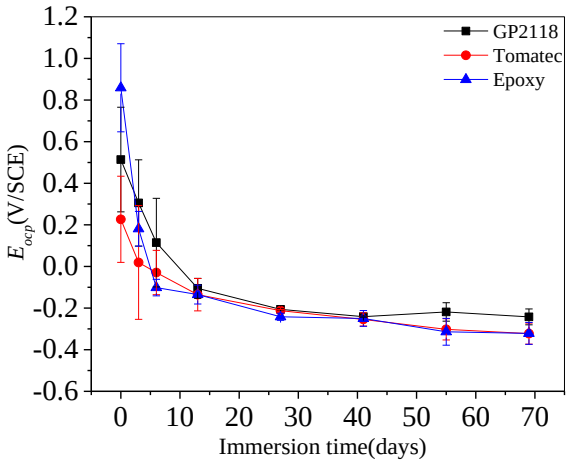

Figure 4.3. OCP values of various samples in 3.5 wt% NaCl solution for up to 69 days.

4.3.2.2. LPR. Figure 4.4 displays the average ± standard deviation of corrosion current densities of three identical samples for each coating, calculated from Eq. (4.2), as a function of immersion time up to 69 days. Overall, the average corrosion current densities of the enamel- and epoxy-coated samples share a similar trend of increase over time because the gradual penetration of electrolyte through the coating increases the corrosion current in the samples. Specifically, the average corrosion current densities of GP2118 and Tomatec enamel-coated samples significantly increase from 7.05×10^{-13} A/cm^2 and 1.03×10^{-12} A/cm^2 in 1 day of corrosion tests to 6.76×10^{-10} A/cm^2 and 6.25×10^{-10} A/cm^2 in 27 days, and then are gradually stabilized at 6.82×10^{-9} A/cm^{2}and 5.76×10^{-9} A/cm^2,

respectively. For the epoxy-coated samples, the starting corrosion current density (3.24×10^{-13} A/cm^2) in 1 day of immersion and the ending corrosion current density (2.00×10^{-8} A/cm^2) in 69 days are respectively lower and higher than their corresponding values of the enamel-coated samples. Consistent with the OCP evolution over time, LPR data indicate that the epoxy-coated samples degrade more rapidly than the enamel-coated samples. According to the Durar Network Specification [45], the corrosion level may be divided into four levels, passivity when $\boldsymbol{i_{corr}}$ < 0.1μA/cm^2, low corrosion when 0.1μA/cm^2 <$\boldsymbol{i_{corr}}$ < 0.5μA/cm^2, high corrosion when 0.5μA/cm^2 <$\boldsymbol{i_{corr}}$ < 1μA/cm^2, and very high corrosion when 1μA/cm^2 <$\boldsymbol{i_{corr}}$. For all the enamel and epoxy coated samples, the corrosion current densities are less than 0.1μA/cm^2, which indicates that all the enamel and epoxy coatings can provide good corrosion protection for the substrate steel.

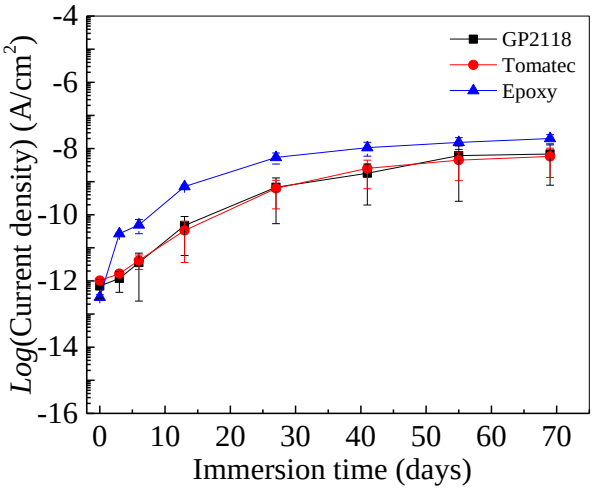

Figure 4.4. Corrosion rates of various samples in 3.5 wt% NaCl solution for up to 69 days.

4.3.2.3. EIS. Figure 4.5 shows the EIS Bode diagrams of 3 representative sample with 2 types of enamel coatings and 1 epoxy coating when immersed in 3.5 wt.% NaCl

solution up to 69 days. Overall, the Bode diagrams of enamel- and epoxy-coated samples are similar, indicating similar corrosion performance of the coated samples. Specifically, the impedance values of enamel-coated samples at low frequency 5 mHz drop slightly from $\mathbf{10^{11}}$ Ω cm^2 in the first 6 days, rapidly in the following 5 weeks, and then slowly to over $\mathbf{10^{6}}$ Ω cm^2 in the final 4 weeks. These impedances are still higher than $\mathbf{10^{5}}$ Ω cm^2 [24], a threshold value below which the protection of coatings as barriers is basically lost. The horizontal platform in impedance diagrams gradually extends from very low frequency at the beginning of tests to middle frequency over time. Therefore, the impedance spectra gradually deviate from those that represent pure capacitive behavior, indicating that the coating resistance and coating capacitance decreased and increased, respectively, as a result of electrolyte penetration through the coating [30]. The phase angles always approach to 90° at high frequency but decrease quickly with immersion time at low and middle frequencies, which is mainly due to the rapid reduction of coating resistance [24].

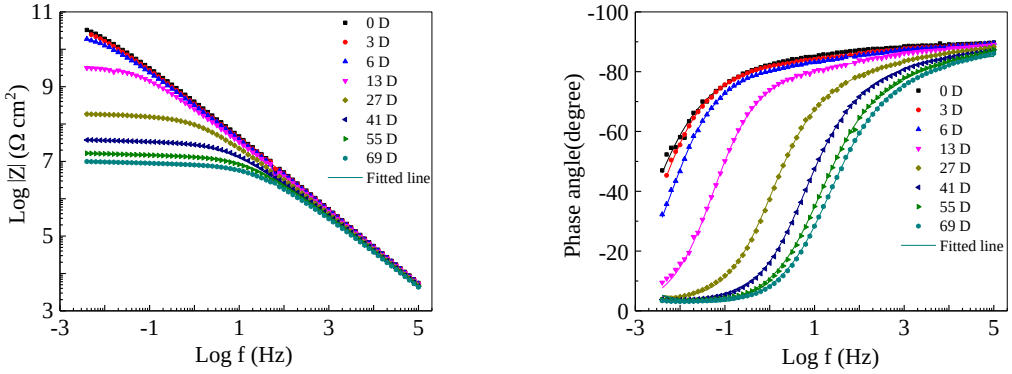

(a-1) (a-2)

Figure 4.5. Bode diagrams for (a) GP2118-, (b) Tomatec-, and (c) epoxy-coated steel samples: (1) impedance and (2) phase angle.

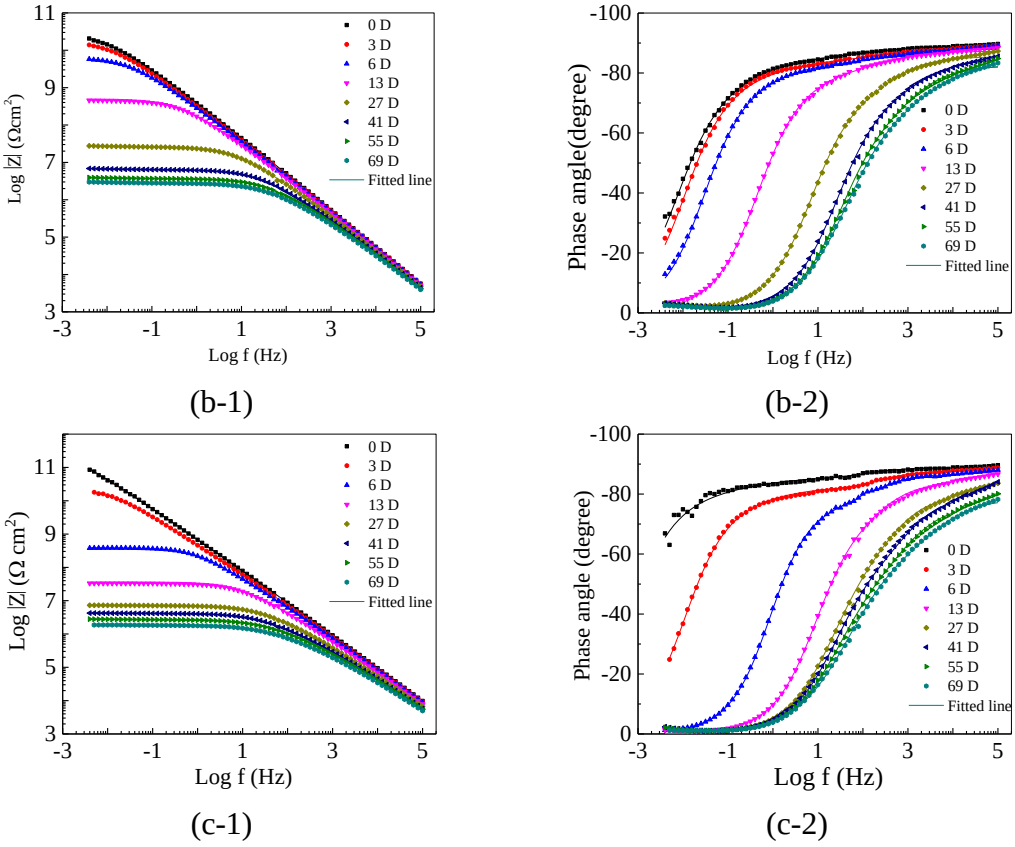

Figure 4.5. Bode diagrams for (a) GP2118-, (b) Tomatec-, and (c) epoxy-coated steel samples: (1) impedance and (2) phase angle (cont.).

In the Bode diagrams, the dotted data points in various symbols mean measurements taken at different times of corrosion tests while the solid lines represent curve fitting by two equivalent electric circuit (EEC) models as shown in Figure 4.6. Model (a) in Figure 4.6 was used to fit the EIS test data up to 13 days of immersion with water and oxygen molecules arriving at the substrate surface and reacting with the steel [33, 48]. However, only one capacitive loop was observed in phase-angle diagrams. This is likely because the two time constants corresponding to electrochemical reactions on the substrate steel/electrolyte interface and the dielectric properties of enamel coatings are nearly in the same order of magnitude [34]. After 27 days of immersion, Model (b) in Figure 4.6 was

used to fit the EIS test data till the end of corrosion tests in 69 days [30]. In this case, a Warburg impedance *W* was included to take into account the diffusion behavior, which was caused by accumulation of corrosion products on the corrosion active sites [33, 48].

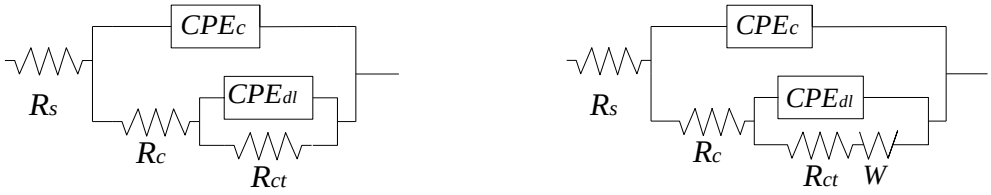

Figure 4.6. EEC models of enamel- and epoxy-coated samples: (a) in the first 13 days and (b) from 27th day to the end of tests.

ZSimpWin was used to determine the parameters in the two EEC models based on the EIS test data recorded. A chi-squared value of 10^{-4} to 10^{-3} achieved indicated a satisfactory fitting goodness. Specifically, R_s represents the solution resistance, R_c and CPE_c mean the coating resistance and capacitance, R_{ct} and CPE_{dl} represent the charge transfer resistance and the double layer capacitance at the electrolyte-steel interface. A constant phase element (CPE) was introduced to signify the deviation from a pure capacitor. For example, CPE_c took into account the non-homogeneity in coating thickness and roughness [27, 28], and CPE_{dl} accounted for a non-uniform distribution of potential [29]. A CPE is defined by two parameters *Y* and n, and its impedance is represented by:

$$Z_{CPE} = Y^{-1}(j\omega)^{-n} \tag{4.3}$$

where *Y* is proportional to the pure capacitance, ω is the angular frequency, *j* is the imaginary unit, and *n* is an index that represents the deviation from a pure capacitor [17]. The effective capacitance based on the CPE parameters can be obtained from [31, 32]:

$$C = Y^{1/n} R^{(1-n)/n} \tag{4.4}$$

where parameters R_c, Y_c, n_c are used to calculate the effective capacitance of enamel coatings C_c; R_{ct}, Y_{dl}, n_{dl} are used to calculate the effective capacitance of double layer C_{dl}.

Figure 4.7 shows the properties of enamel and epoxy coatings: coating resistance R_c and coating capacitance C_c, in which the average $\pm$ standard deviation values were determined from the measurements taken from three samples of identical condition. In general, the coating resistance measures the performance of a coating as a barrier against electrolyte penetration, which is closely related to coating microstructures such as open pores and pinholes. The coating capacitance indicates the diffusion of electrolyte solution into the coating, which is associated with the dielectric property, microstructure, and thickness of the coating.

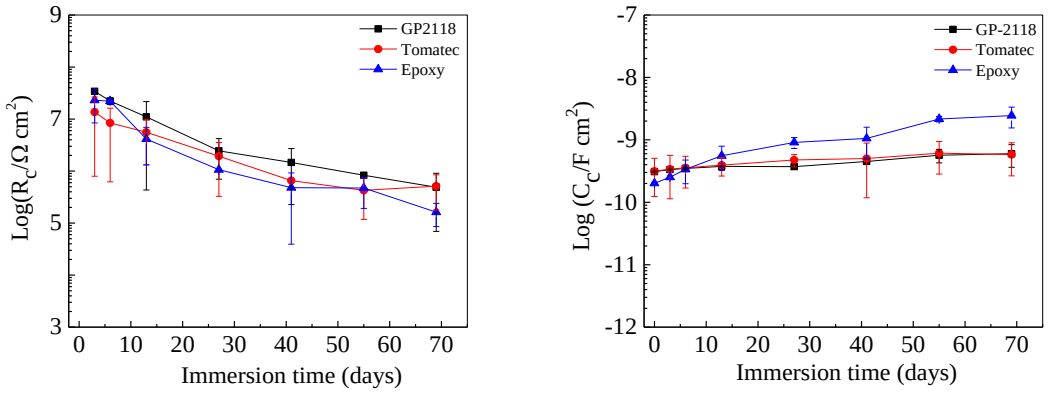

(a) (b)

Figure 4.7. Comparison of coating properties: (a) coating resistance R_c and (b) coating capacitance C_c.

It can be observed from Figure 4.7 that resistances of the two enamel coatings decrease gradually while the coating capacitances slightly increase with the immersion time. The reason is that electrolyte solution gradually penetrates into the coating, thus

increasing the coating capacitance [30, 33, 48]. The properties of epoxy coating follow the same changing trend as the enamel coatings. However, after 13 days of immersion, the resistance and capacitance of the epoxy coating are smaller and larger, respectively, than those of the enamel coatings. Therefore, enamel can more effectively prevent electrolyte from penetrating through the coating than epoxy.

Figure 4.8 displays the steel-solution interfacial properties of enamel- and epoxy-coated samples: charge transfer resistance R_{ct} and double layer capacitance C_{dl}, in which the average ± standard deviation values were determined from the measurements taken from three samples of identical condition. The charge transfer resistance is a measure of how easily electrons can transfer across the metal surface, which is inversely proportional to the corrosion rate [36]. It can be seen from Figure 4.8 that the charge transfer resistances of the enamel- and epoxy-coated samples decrease rapidly with immersion time since more electrochemically reactive spots appear on the substrate interface over time. After 3 days of immersion, the GP2118 enamel-coated samples have the highest charge transfer resistance among three types of coating, which is in general agreement with the low corrosion rates as presented in Figure 4.4. The double layer capacitance C_{dl}, calculated from Eq. (4.4), is also a measure of the ease of charge transfer. The C_{dl} of epoxy-coated samples increases rapidly with immersion time up to 13 days and gradually arrives at 33.29 nF cm^{-2} after 69 days of immersion. The C_{dl} of Tomatec enamel-coated samples slightly fluctuates over time and finally reaches to 3.85 nF cm^{-2}. The C_{dl} of GP2118 enamel-coated samples is quite stable throughout the corrosion tests with a value of 0.77 nF cm^{-2}, which is the lowest among the three coatings at the end of corrosion tests in 69 days. Among three types of coatings, GP2118 enamel most effectively protects its substrate steel from

corrosion since its charge transfer resistance and double layer capacitance are respectively the highest and the lowest.

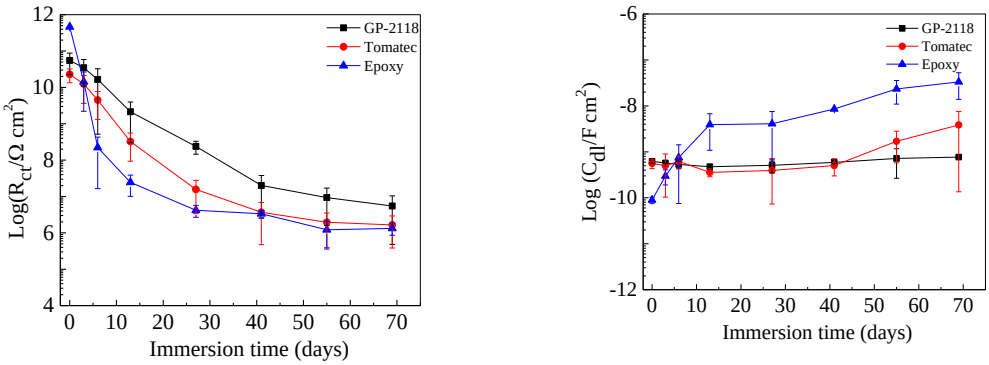

(a) (b)

Figure 4.8. Comparison of steel-solution interfacial parameters: (a) charge transfer resistance and (b) double layer capacitance.

4.3.3. Visual Observation after Corrosion Tests. After corrosion tests, the surface conditions of all tested samples were examined visually as shown in Figure 4.9. No corrosion products were observed on the surface of enamel and epoxy coatings. All the coatings can provide excellent corrosion protection for the substrate steel. This observation is consistent with the electrochemical test data such as the lowest corrosion resistances exceeding their threshold value.

(a) (b) (c)

Figure 4.9. Surface conditions of (a) GP2118 enamel-, (b) Tomatec enamel-, and (c) epoxy-coated samples after corrosion tests.

4.4. SUMMARY

In this study, the microstructure and corrosion resistance of GP2118 and Tomatec enamel-coated and epoxy-coated samples have been investigated. Based on the test results and analysis, the following conclusions can be drawn:

1. The enamel coatings on steel samples have solid structures with disconnected pores, resulting in a porosity content of 12.72% and 4.26%, respectively.
2. The results from three electrochemical tests (OCP, LPR, and EIS) are in general agreement. As electrolyte gradually penetrates through various coatings over time, the OCP values of all coated samples decreased, the corrosion current densities increased, and the coating resistance and charge transfer resistance decreased while the coating capacitance and double layer capacitance increased. The epoxy coating degraded more rapidly than the enamel coatings tested. Overall, there is no obvious sign of corrosion in all coated samples tested in 69 days as confirmed by visual inspection.
3. The Bode diagrams of GP2118 enamel-, Tomatec enamel-, and epoxy-coated samples evolve over time in similar ways. At the completion of corrosion tests in 69 days, the average impedances of the three types of samples at 5 mHz were reduced to 9.04 MΩ cm^2, 3.12 MΩ cm^2, and 1.88 MΩ cm^2, respectively, while their phase angles at high frequency all approached to 90°. The coatings are good barriers against electrolyte penetration and can protect substrate steel from corrosion in sodium chloride solution. The enamel coatings revealed the same corrosion protective behavior as the epoxy coating.

5. PITTING CORROSION PROTECTION OF LARGE ENAMEL-COATED SAMPLES WITH SALT SPRAY TEST

5.1. BACKGROUND

Salt spray test, as an accelerated corrosion test, produces a corrosive attack to coated samples in order to evaluate the performance of coating for corrosion protection. Coated samples are placed in and periodically taken out of a chamber for examination on the potential formation of corrosion products on the surface of the samples. In general, the more corrosion-resistant the coating is, the longer the test lasts prior to the appearance of corrosion products.

Large specimens are more prone to pitting corrosion due to more exposed surface areas. During the wet coating process, the coating applied on the curved internal surface at the crown area of a steel pipe is likely thinner than elsewhere due to gravity. This may influence the uniformity and corrosion resistance of the enamel coating. While electrochemical tests are widely used to evaluate the corrosion resistance and study the corrosion mechanism of coated steel substrates in controlled small areas, salt spray tests are ideal for evaluating the corrosion performance of enamel-coated pipes with large exposed surface areas.

In this study, large specimens were cut from an API 5L X65 steel pipe (MRC Global Inc.). Three damaged points were created on half of the specimens for each type of enamel coating. The undamaged samples were tested in the salt spray chamber for six weeks and the damaged samples are tested for one week. After the salt spray test, coating morphology was evaluated through visual and microscopic cross-sectional examinations.

5.2. EXPERIMENTAL PROCEDURE

5.2.1. Materials and Specimens. Twelve 75 mm × 150 mm pipe samples were prepared. On their inside curve surface, six samples were coated with enamel GP2118 and the other six samples were coated with enamel Tomatec. Each enamel-coated sample was covered with marine epoxy (LOCTITE) on all sides except the enamel-coated surface. Three impact points were created on half of the enamel-coated samples to simulate mechanical damage.

5.2.2. Salt Spray Test. The salt spray test was conducted according to the standard operation practice (ASTM B1187-16) using the Q-FOG cyclic corrosion tester as shown in Figure 5.1 [49]. A salty fog was continuously supplied from salt water under a steady stream of clean compressed air, and injected into the enclosed chamber through a nozzle (or atomizer) located in the middle of the chamber's floor. The salt solution that gradually accumulated inside the chamber was disposed through a drain positioned on the chamber floor. Besides, an elevated temperature was maintained inside the chamber using the built-in heating units.

(a) (b)

Figure 5.1. Salt spray chamber.

The specimens were spaced approximately 75 mm from each other and placed on the panel with holes for accumulated solution to flow away. The salt fog was constantly distributed throughout the chamber and the average fall-out rate was approximately 70 mL for each 8000 sq-mm of horizontal surface area over a period of 48 h. The solution was made by adding 5% USP grade sodium chloride into distilled water by weight. The temperature within the chamber was maintained at 35 ±2 °C throughout the whole testing period.

During the test, the chamber was opened periodically for sample surface examination. The undamaged samples were tested for 6 weeks and retrieved after corrosion spots had been observed on all the sample surfaces. The damaged samples were tested for one week only since the mechanically damaged spots were corroded more rapidly.

5.2.3. Coating Characterization. After the salt spray test, coating morphology was evaluated through visual and microscopic cross-sectional examinations. Each enamel-coated sample was first cold-mounted in epoxy resin (EpoxyMount, Allied High Tech Products, Inc.), and cut into a 10.0 mm thick cross section with a diamond saw. The cross-section of the exposed steel was held against a 203 mm-diameter rotating platform and polished with carbide papers from the coarsest to the finest with 180, 320, 600, 800, and 1200 grits. A steady stream of water was used to continually saturate the surface of the polishing paper fixed on the rotating platform.

After abrading, all samples were rinsed with deionized water and dried at room temperature. Examination of a finished cross section was then conducted using a scanning electron microscopy (SEM, Hitachi S-4700, Tokyo).

5.3. RESULTS AND DISCUSSION

5.3.1. Surface Observation. Figure 5.2 shows the surface conditions of six undamaged specimens after each week of salt spray test. The left three samples were coated with GP2118 enamel and the right three samples were coated with Tomatec enamel.

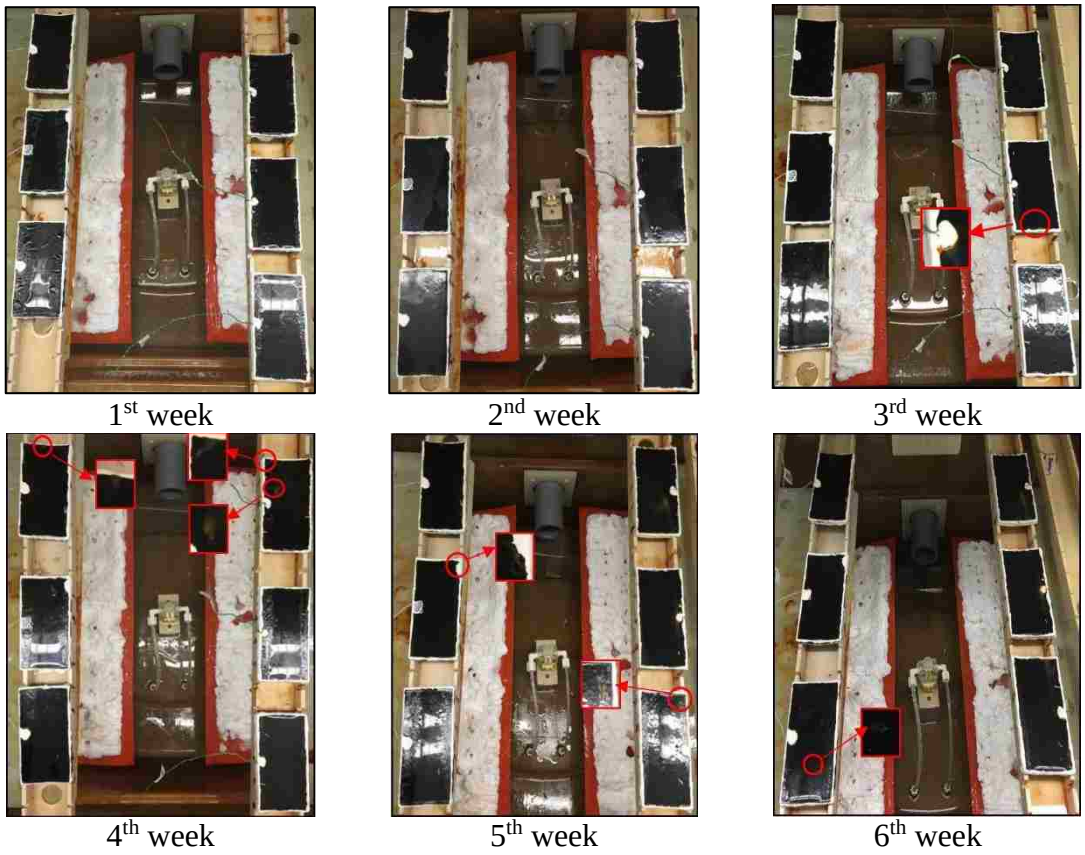

Figure 5.2. Undamaged specimen surface conditions after each week of salt spray test. (Left: enamel GP2118; Right: enamel Tomatec).

After two weeks of testing, none of the samples showed any sign of corrosion. By the end of the third week, the second Toamtec enamel-coated sample showed one corrosion spot. After four weeks of testing, the first GP2118 enamel-coated sample showed one corrosion spot and the first Tomatec enamel-coated sample showed two corrosion spots.

After five weeks of testing, the corrosion spots were observed on the second GP2118 enamel-coated sample and the third Tomatec enamel-coated sample. By the end of the sixth week, a tiny corrosion spot started on the third GP2118 enamel-coated sample surface. Thereafter, all the samples had corrosion spots of various size. Figure 5.3 showed the surface condition of each sample at the completion of the salt spray test. In Figure 5.3, the red circles showed the exact corrosion spots and all the corrosion spots were relatively small. Only pitting corrosion was generated and no extensive corrosion occurred during the entire salt spray tests.

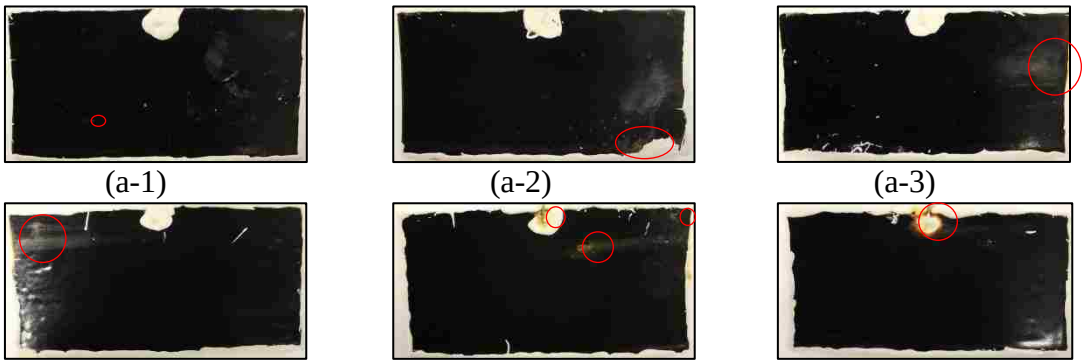

Figure 5.3. Damaged specimen surface conditions after 6 weeks of salt spray test. (a: GP2118 enamel; b: Tomatec enamel).

Figures 5.4(a) and 5.4(b) show the surface conditions of six damaged specimens prior to the salt spray test and after 48 hours of salt spraying, respectively. After 48 hours of testing, brown corrosion products were clearly observed on damaged points of all the tested samples except that the third Tomatec enamel-coated sample showed minor corrosion on the damaged points. Figure 5.5 shows the sample surface conditions after one week of the salt spray test. Severe corrosion happened around the impact points with corrosion products flowing down.

(a) (b)

Figure 5.4. Damaged specimen surface conditions (a) prior to salt spray test; (b) after 48 hours of salt spray test. (Left: GP2118 enamel; Right: Tomatec enamel).

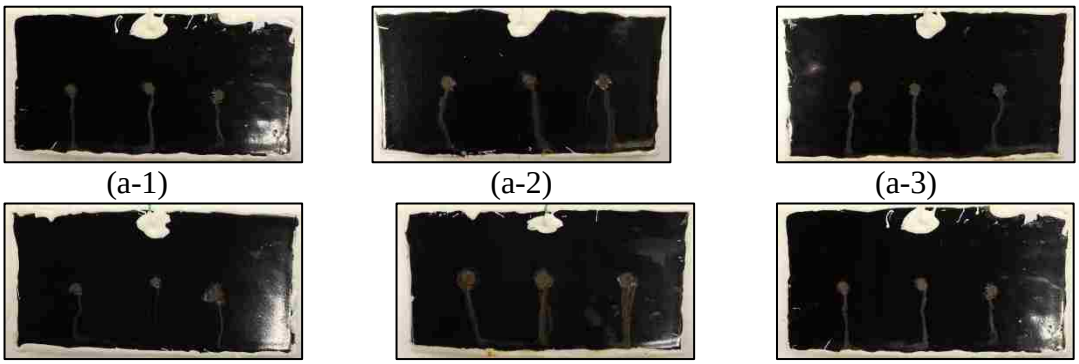

(a-1) (a-2) (a-3)

(b-1) (b-2) (b-3)

Figure 5.5. Specimen surface conditions after one week of the salt spray test (a: damaged GP2118 enamel; b: damaged Tomatec enamel).

5.3.2. Microstructure of GP2118 and Tomatec Enamel-Coated Samples. Cross sectional SEM images of representative enamel-coated steel samples are presented in Figure 5.6. Figures 5.6(a-1) and 5.6(b-1) present the microstructures of the intact coatings and Figures 5.6(a-2) and 5.6(b-2) show the microstructures of the damaged coatings. As shown in Figure 5.6(a-1), the GP2118 enamel coating, approximately 180 μm thick, has an amorphous structure. The air bubbles in the coating are disconnected and the porosity

content is approximately 3.51%. The coating contains several big air bubbles with a diameter of up to 41 μm.

For the Tomatec enamel-coated sample as shown in Figure 5.6(b-1), the coating thickness is approximately 235 μm. It has more air bubbles with a porosity content of 6.57% and the largest diameter smaller than that of the GP2118 enamel. Figures 5.6(a-2) and 5.6(b-2) show the cross sections in damaged areas. The steel substrate remains still covered with enamel coating, although significantly thinner.

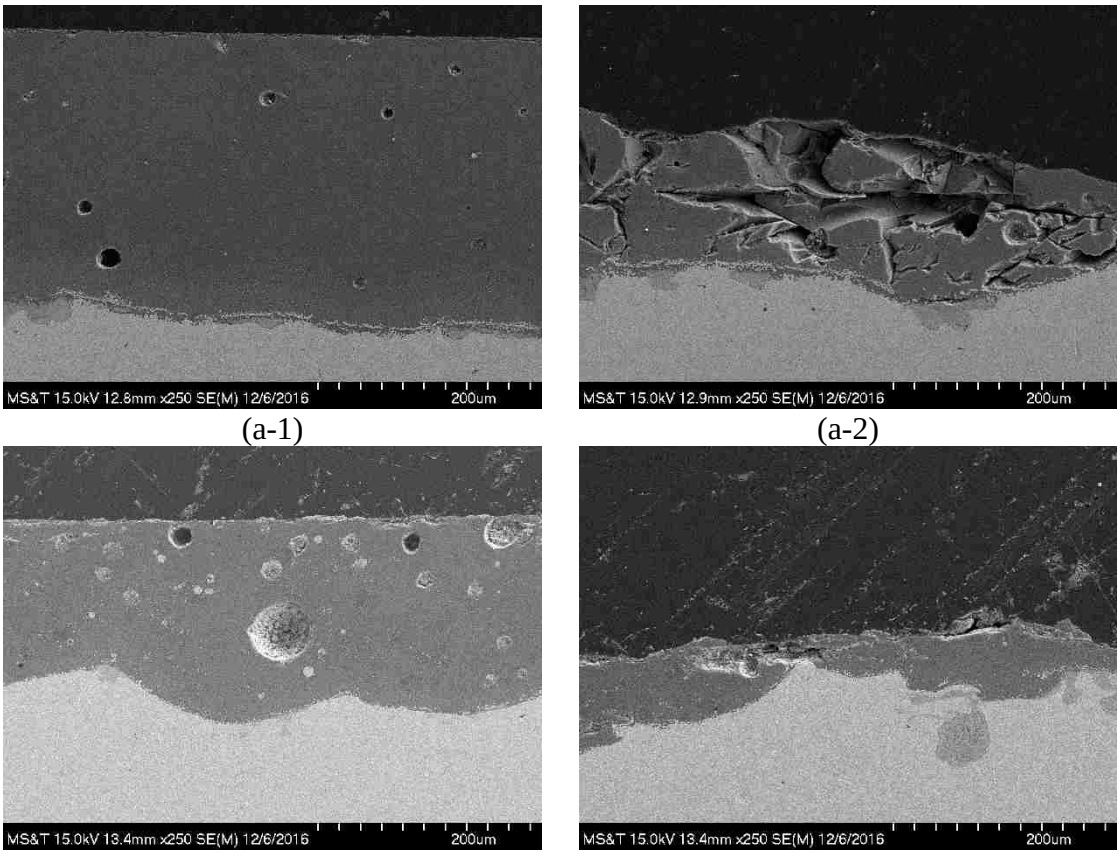

(a-1) (a-2)

(b-1) (b-2)

Figure 5.6. Cross-sectional SEM images of (a) GP2118 enamel and (b) Tomatec enamel for (1) intact area and (2) damaged area with magnification of 200×.

5.4. SUMMARY

In this study, the corrosion performance of GP2118 and Tomatec enamel-coated samples and the microstructure of both coatings after the salt spray test have been investigated. Based on the test results and analysis, the following conclusions can be drawn:

1. Intact enamel-coated samples performed well throughout the salt spray test. Only minor corrosion spots appeared on the surface of samples after six weeks of testing. No significant corrosion occurred during the entire salt spray test.
2. For the damaged samples, brown corrosion products around the damaged points of all tested samples were clearly observed after 48 hours of testing.
3. At the damaged area, the steel substrate was covered by the enamel coating with reduced thickness.

6. CORROSION RESISTANCE OF PIPELINE STEEL WITH DAMAGED ENAMEL COATING AND CATHODIC PROTECTION

6.1. BACKGROUND

Organic coatings such as epoxy are widely used to prevent steel pipelines from corrosion in combination with supplementary cathodic protection (CP). When a coating has defects or is damaged during pipeline installations and operations, its substrate steel is directly exposed to the surrounding environment. In this case, the exposed steel can still be prevented from corrosion through the CP as a secondary defense system [30, 50]. However, the effect of a CP makes the exposed metal surface strongly alkaline because of water reduction, which causes organic coating delamination through the hydrolysis of coating or coating-substrate interface [30, 52].

Porcelain enamel, as an inorganic material, is chemically bonded to its substrate metal by fusing glass frits at a temperature of 750℃~850℃. It can not only be finished with a smooth and aesthetical surface, but also provide good chemical stability, high corrosion resistance, and excellent resistance to abrasion in an extreme erosion environment [11]. When applied in pipeline lining, enamel coating can not only extend the service life of steel pipes but also increase the pipeline operating temperature to 400 °C with a safety factor of approximately 1.25 [52].

The previous studies on the steel samples with intact enamel coating [25, 53] indicated that the enamel coating could protect steel from corrosion in NaCl solution by providing an effective barrier to electrolyte penetration. In real-world operation conditions, solids may flow with fluids in a pipeline and generate abrasive forces and impact on internal enamel coating, resulting in small-scale chipping and coating erosion [54]. The

exposed steel would have been further protected by the CP, if present. However, the corrosion resistance of pipe steel with damaged enamel coating and the CP, and the CP effect on the interface condition between the enamel coating and its substrate steel have never been investigated previously.

Electrochemical tests are widely used to study the degradation process of coatings. However, electrochemical responses are concentrated on the local areas where coatings are damaged, since their impedance is much lower than that of the surrounding areas with intact coating. In this study, a dual-cell test setup was used to separate 3.5 wt. % NaCl solution in contact with the damaged and intact coating areas during response measurements [55, 56] by potentiostatic and electrochemical impedance spectroscopy (EIS) tests, respectively. Therefore, the potential effect of the damaged coating area on the corrosion process of the intact coating area, as alluded from epoxy coating, can be investigated. To help interpret the CP effect on the condition of coating-substrate interfaces, coating microstructures are examined with scanning electron microscopy (SEM).

6.2. MATERIALS AND METHODS

6.2.1. Sample Preparation. An API 5L X65 steel pipe (MRC Global) with 323.9 mm in outer diameter and 9.53 mm in wall thickness was selected as substrate metal in this study. The steel pipe was cut into 9 25 mm×50 mm coupon samples. The cut samples were steel blasted for 1 min to remove mill scales and rusts, and then cleansed with acetone.

The steel coupons were coated with enamel slurry Tomatec. The enamel slurry was prepared by first milling glass frits, clay and certain electrolytes together, and then mixing

them with water until the mixture is in a stable suspension state. The water, glass frits, and clay were mixed in a proportion of 1.00: 2.40: 0.17 by weight. The enamel slurry was manually sprayed on the surface of each coupon sample. All the samples were heated at 150 °C for 10 mins to drive off moisture, fired at 815°C for 10 min, and finally cooled to room temperature. An optic microscope Hirox was used to measure the coating surface roughness with an average value of 1μm. The PosiTest following ASTM D4541-09 was used to measure the bond strength between the coating and the substrate steel with an average value of 17 MPa. Due to the roughness at steel surface, the thickness of enamel coating at different locations varies slightly with a standard deviation of 19 μm.

To study the effect of damage on the corrosion resistance of enamel coating, one damage area as shown in Figure 6.1 was created at the center of each enamel-coated sample using an impact test apparatus according to the ASTM Standard G14 [57]. The apparatus consists of a 0.91 kg steel rod with a hemispherical head and a vertical section of hollow aluminum tubing to guide the rod. The weight rod was dropped from a height of 84 cm to damage the coatings. A close-up view in Figure 6.1 shows the detail around the damaged area.

Figure 6.1. Impact induced coating damage.

6.2.2. Characterization of Enamel Coatings. The coating microstructure was characterized with scanning electron microscopy (SEM, Hitachi S4700). Each enamel-coated sample with the damage as shown in Figure 6.1 was cold mounted in epoxy resin (EpoxyMount, Allied High Tech Products, Inc.). A 10 mm-thick cross section was cut from the damaged coating area of the sample, and abraded with carbide papers with grits of 80, 180, 320, 600, 800, and 1200. After abrading, all samples were cleansed with deionized water and dried at room temperature prior to SEM imaging.

6.2.3. Electrochemical Tests. Each coupon sample was embedded into the mount epoxy except the surface of enamel coating to be tested for corrosion performance, as shown in Figure 6.2(a). The mount epoxy was over 2 mm thick to ensure that the enamel coating surface is the response site during electrochemical tests. A PVC funnel (1 cm in diameter) was attached onto the coating surface covering the damage area as shown in Figure 6.2(b). The sample was placed in a large plastic container with the funnel faced up. The funnel and container were filled with 3.5 wt. % NaCl solution to ensure that the funnel is completely submerged. The solution was prepared by adding purified sodium chloride (Fisher Scientific, Inc.) into distilled water. CP was introduced for the entire coated area.

During electrochemical tests, the 3.5 wt. % NaCl solution around the damaged coating area was separated by the funnel from the solution around the remaining intact coating area. Otherwise, the electrochemical responses would have been concentrated on the damaged area since its impedance would be much lower than that of the other area and, thus, the measured responses would be representative to neither the damaged coating areas nor the other intact coating area. For the same reason, the damaged and intact coating areas were tested up to 10 days and 70 days, respectively.

The electrochemical tests were conducted at room temperature every 5 days in a classic three-electrode system with a saturated calomel electrode (SCE) as the reference electrode, a graphite rod as the counter electrode, and a coupon sample as the working electrode. The three electrodes were connected to an Interface1000E Potentiostat (Gamry Instrument) for measurement. The SCE and graphite rods were immersed in the large container for the intact enamel coating area, as shown in Figure 6.2, and in the funnel for the damaged enamel coating area (not shown in Figure 6.2 for clarity).

One sample was subjected to zero cathodic potential (under the open circuit potential), another one to a cathodic potential of -0.85 vs. SCE/V and the third one to a cathodic potential of -1.15 vs. SCE/V. Potentiostatic tests were first conducted to measure currents for 1,000 seconds at -0.85 vs. SCE/V or -1.15 vs. SCE/V. EIS tests were then conducted under a sinusoidal potential wave (10 mV in amplitude and a frequency range of 10^5 to 10^{-2} Hz) around a cathodic potential of zero, -0.85 vs. SCE/V and -1.15 vs. SCE/V. EIS test data were simulated with classical electrical equivalent circuits (EEC) and analyzed with the software ZSimpWin.

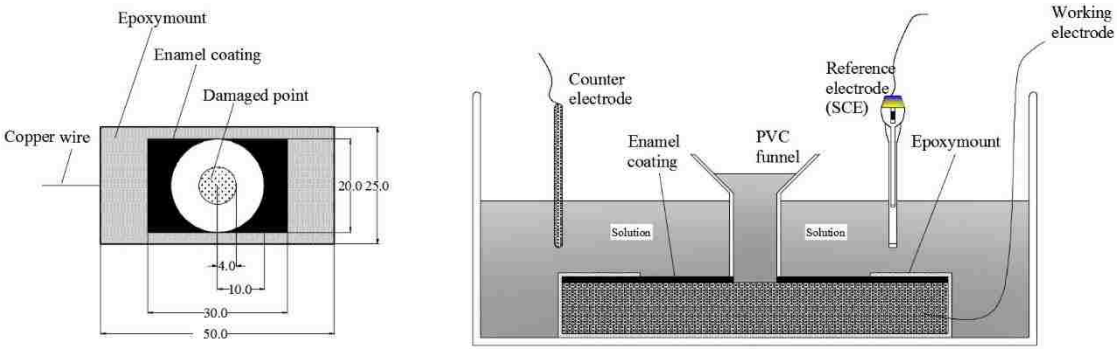

(a) (b)

Figure 6.2. Schematic representation of the double electrochemical cell (unit: mm).

6.3. RESULTS AND DISCUSSION

6.3.1. Coating Microstructure. Cross-sectional SEM images of enamel-coated steel samples tested under the OCP and CP (-1.15V/SCE) conditions are presented in Figure 6.3. In general, the enamel coatings have amorphous structures with isolated air bubbles. Gaseous CO, CO_2, and H_2 are generated during the firing process of enameling. When cooled down, these gases are trapped as a thick layer of enamel is solidified, and generate the isolated air bubbles [10, 58].

Figures 6.3(a) and 6.3(b) represent the stitched images of five SEMs taken along a radial direction of the damaged coating area as shown in Figure 6.1. Due to the falling-off of chipped coating after impact tests, the coating thickness decreased gradually from 244 µm to 4 µm for samples to be tested under the OCP, and from 190.48 µm to 4 µm for samples to be tested under -1.15 V/SCE. However, the substrate surface is still covered with a thin layer of enamel coating at the center of damaged area as indicated in Figure 6.1.

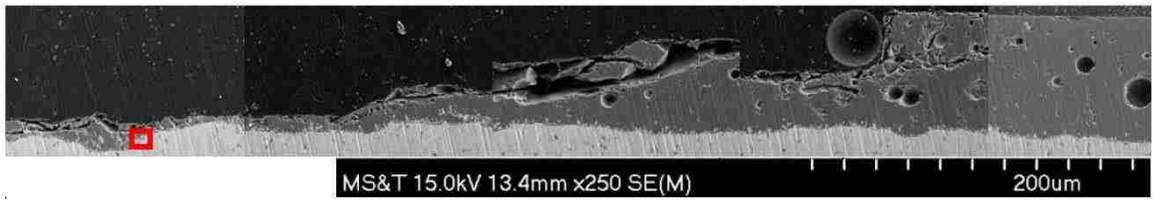

(a)

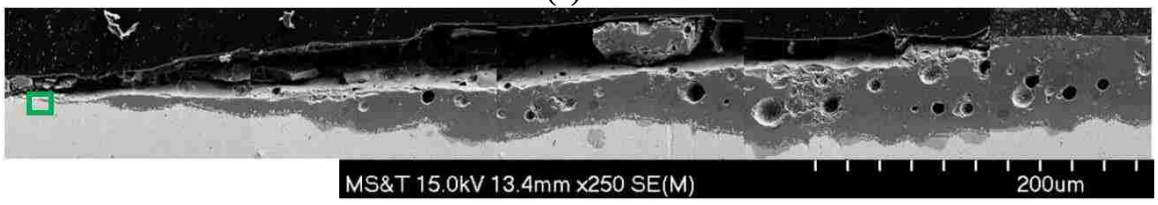

(b)

Figure 6.3. Cross-sectional SEM images of enamel-coated samples under the OCP (a and c) and -1.15 V/SCE (b and d) with a magnification of 250× (a and b) and 2500×(c and d).

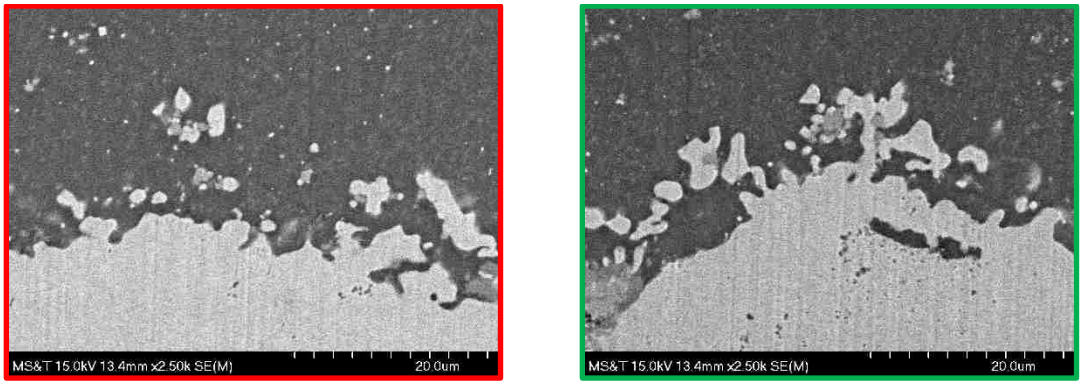

(c) (d)

Figure 6.3. Cross-sectional SEM images of enamel-coated samples under the OCP (a and c) and -1.15 V/SCE (b and d) with a magnification of 250× (a and b) and 2500×(c and d) (cont.).

Figures 6.3(c) and 6.3(d) are the magnified details at enamel-steel interfaces from Figures 6.3(a) and 6.3(b). They show the extensive formation of an island-like structure in the enamel coating during the firing process, thus forming a durable enamel-steel interface transition zone [9]. The island-like structure are the iron-alloys formed as a result of the chemical reactions of metal oxides in the enamel and the carbon and iron in the steel. No delamination was found after the corrosion tests, and the CP thus did not affect the mechanical condition of the interface between the enamel coating and steel substrate.

6.3.2. EIS. Figure 6.4 shows the EIS Bode diagrams of 3 representative samples tested under a cathodic potential of -1.15 V/SCE and -0.85 V/SCE, and an OCP, respectively, in intact enamel coating (a-1, b-1 and c-1) and damaged enamel coating (a-2, b-2 and c-2). Both the measured (Meas.) data in various symbols and their fitted (Ftd.) curves are presented in Figure 6.4. On a log-log scale, the impedance of the sample tested under -1.15 V/SCE in the first 40 days decreased linearly with the frequency; this relation was independent of the day of testing as indicated in Figure 6.4(a-1). Starting from the 50th day, the impedance experienced a gradual decrease at low frequency but remained over 10

GΩ cm^2 at a frequency of 0.02 Hz. The phase angles in the high and middle frequency ranges were close to 90° during the entire immersion time and increased with the frequency in the low frequency range. For the sample tested under a cathodic potential of -0.85V/SCE, as shown in Figure 6.4(b-1), the impedance on a log-log scale decreased linearly in the first 10 days and then showed a gradually-expanding horizontal platform in the low to middle frequency range over time. The impedance at a frequency of 0.02 Hz decreased from 24 GΩ cm^2 at the beginning to 0.76 GΩ cm^2 at the end of the test. The phase angle increased with the frequency from the low to middle frequency range and remained 90° till 70 days of immersion time in the high frequency range. The phase-frequency curves in the low frequency range were shifted towards the middle frequency range over the immersion time.

For the sample tested under a cathodic potential of -0.85V/SCE, as shown in Figure 6.4(b-1), the impedance on a log-log scale decreased linearly in the first 10 days and then showed a gradually-expanding horizontal platform in the low to middle frequency range over time. The impedance at a frequency of 0.02 Hz decreased from 24 GΩ cm^2 at the beginning to 0.76 GΩ cm^2 at the end of the test. The phase angle increased with the frequency from the low to middle frequency range and remained 90° till 70 days of immersion time in the high frequency range. The phase-frequency curves in the low frequency range were shifted towards the middle frequency range over the immersion time.

The impedance and phase angle of the sample tested under the OCP, as shown in Figure 6.4(c-1), showed a similar trend to the sample tested under a cathodic potential of -0.85V/SCE, particularly towards the end of corrosion tests. However, the horizontal platform was further extended to the middle frequency range and the impedance at a frequency of 0.02 Hz was 0.26 GΩ cm^2 after 70 days of test.

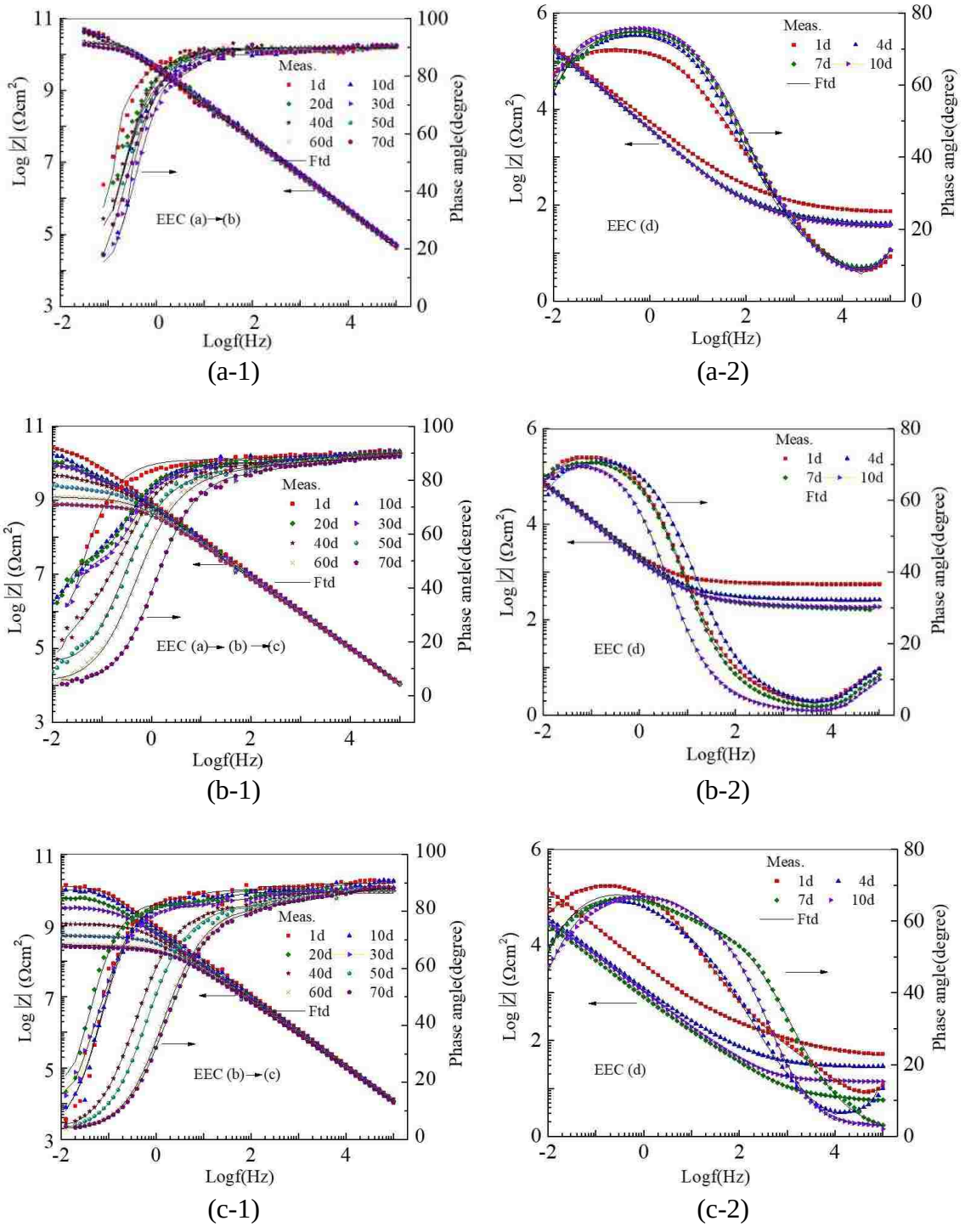

Figure 6.4. Bode diagrams of enamel-coated samples immersed in 3.5 wt.% NaCl solution up to 70 days at (1) intact coating zone, and up to 10 days at (2) damaged coating zone under a cathodic potential of (a) -1.15 vs. SCE/V, (b) -0.85 vs. SCE/V, and (c) the OCP.

Figures 6.4(a-2), 6.4(b-2) and 6.4(c-2) show the Bode diagrams of the samples tested in the damaged-coating zone. Overall, the Bode diagrams of the samples tested under the CP and the OCP are similar, indicating comparable corrosion performances of all the samples in the damaged zone. The impedance became stable after 4 days of immersion in the solution. Because of the damage made on the coating, the impedance at 0.02 Hz was approximately 0.1 MΩ cm^2, which is 10^6 times smaller than that of the samples tested in the intact coating zone. On a log-log scale, the impedance linearly decreased in the low frequency range and gradually approached an asymptotic value in the high frequency range. The maximum phase angle, lower than 80°, appeared in the low frequency range, indicating that corrosion had already taken place in the steel substrate.

Figure 6.5 shows four equivalent electrical circuit (EEC) models used to fit the EIS test data taken from different samples under various test conditions. In this study, a constant phase element (CPE) was used instead of a pure capacitor due to the non-homogeneity in coating thickness and roughness [27, 28] or the electrochemical reactivity on the substrate steel [29]. A CPE is defined by two parameters Y and n, and its impedance is represented by:

$$Z_{CPE} = Y^{-1}(j\omega)^{-n} \tag{6.1}$$

where $j = \sqrt{-1}$ is the imaginary unit, Y is a CPE constant, ω is the angular frequency, and n ($0 \leq n \leq 1$) is an index that represents the deviation of the CPE from a corresponding pure capacitor [30].

The EEC models used to fit into the EIS data from various tested samples are included in Figure 6.5. Model (a) [33, 48] was used for the samples with intact coating tested under -1.15V/SCE up to 40 days, considering the decrease in coating resistance and

increase in coating capacitance as water begins to seep through the channels in enamel coating. Here, R_s represents the solution resistance, R_c and CPE_c mean the pore resistance and capacitance of the coating, respectively. After 40 days of immersion when water and oxygen molecules arrived at the substrate surface and reacted with the substrate steel, the EIS data was fitted with Model (b) till the end of corrosion tests [33, 48, 60]. Here, R_{ct} is the charge transfer resistance and CPE_{dl} is the double layer capacitance at the steel-electrolyte interface. However, only one capacitive loop was observed in the phase-frequency diagram. This is likely because the time constant associated with the dielectric properties of enamel was difficult to distinguish from that of the electrochemical reaction at the steel-electrolyte interface [34, 48].

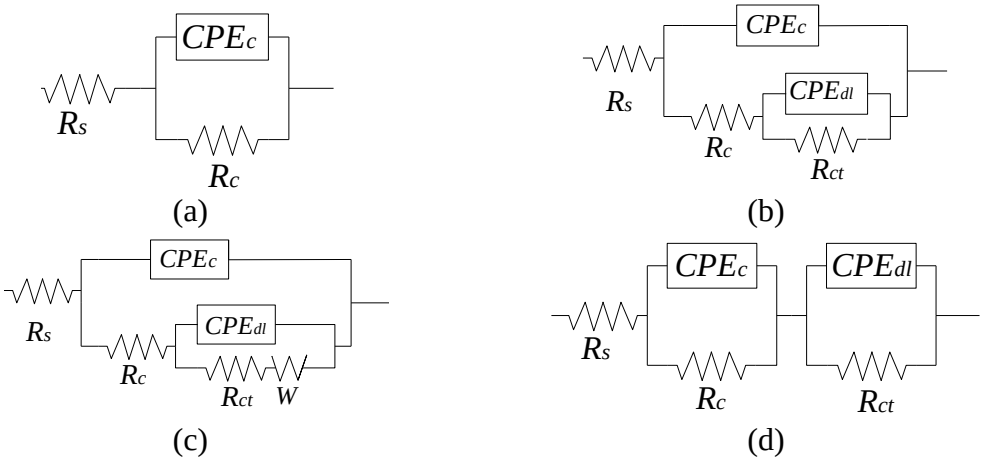

Figure 6.5. Equivalent electrical circuit models.

For the intact enamel coating zone under -0.85V/SCE, Model (a) was used in the first 10 days of immersion, Model (b) was applied from the 15th day to the 45th day, and Model (c) was used till the last day of test. A Warburg impedance *W* in Model (c) was included to take into account the diffusion behavior, which was induced by the

accumulation of corrosion products at the corrosion active sites. For the intact coating zone under the OCP, Model (b) was used for tests up to 40 day and Model (c) for the remaining tests. For all the damaged coating zones, two time constants can be clearly observed in the phase-frequency diagram and Model (d) was thus used to fit the test data [12]. While Model (b) was applicable for the intact coating zone when the solution has penetrated through the channel in the coating and is in contact with the substrate steel, Model (d) is more appropriate for the damaged-coating zone since the coating layer becomes thinner and the solution can penetrate into the coating easily. The electrochemical reactivity occurred uniformly on the damaged coating surface.

Figure 6.6 shows the changes of pore resistance R_c and capacitance CPE_c of intact coatings. In general, the pore resistance measures the ease of electrolyte penetration into the coating, which is related to the number and distribution of open pores and pinholes in the enamel coating. The coating capacitance also indicates the extent of electrolyte diffusion into the coating, which is associated with the thickness and dielectric property of the coating [17]. The R_c value of the sample tested under -1.15 V/SCE decreased from 57.6 $G\Omega\ cm^2$ to 4.92 $G\Omega\ cm^2$ while the R_c value of the samples tested under -0.85V/SCE and the OCP decreased more rapidly from 20.9 $M\Omega\ cm^2$ to 1.57 $M\Omega\ cm^2$ over 70 days. The coating capacitance of all the samples increased with immersion time since the electrolyte solution gradually penetrated into the coating, thus increasing the coating capacitance. All the samples tested under the CP have larger coating resistances than the samples under the OCP. Thus, the CP improved the coating performance [30]. The sample tested under -1.15 V/SCE has a larger coating resistance and smaller coating capacitance than its respective values of the sample under -0.85 V/SCE. This result indicates that the higher cathodic

potential used in tests does not affect adversely the coating property; it can decelerate the degradation process of the coating. Figure 6.7 shows the pore resistance and double layer capacitance of damaged coating.

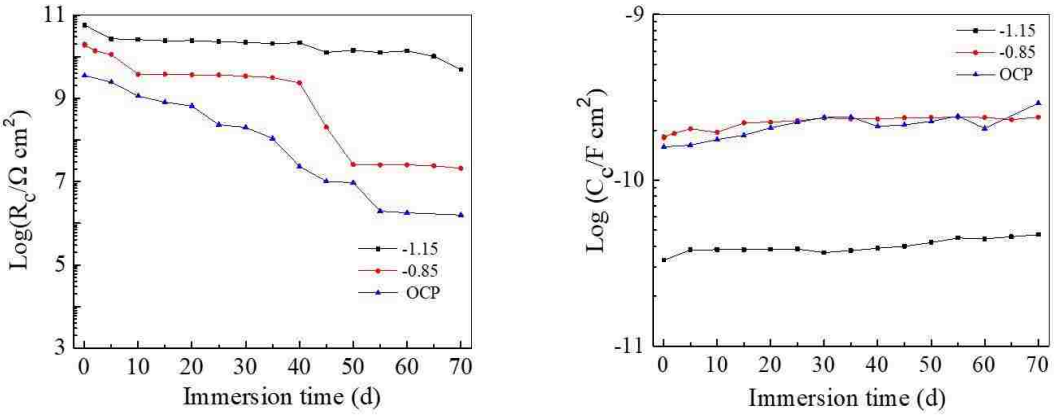

(a) (b)

Figure 6.6. Properties of intact coating under various CP levels: (a) pore resistance R_c and (b) capacitance CPE_c.

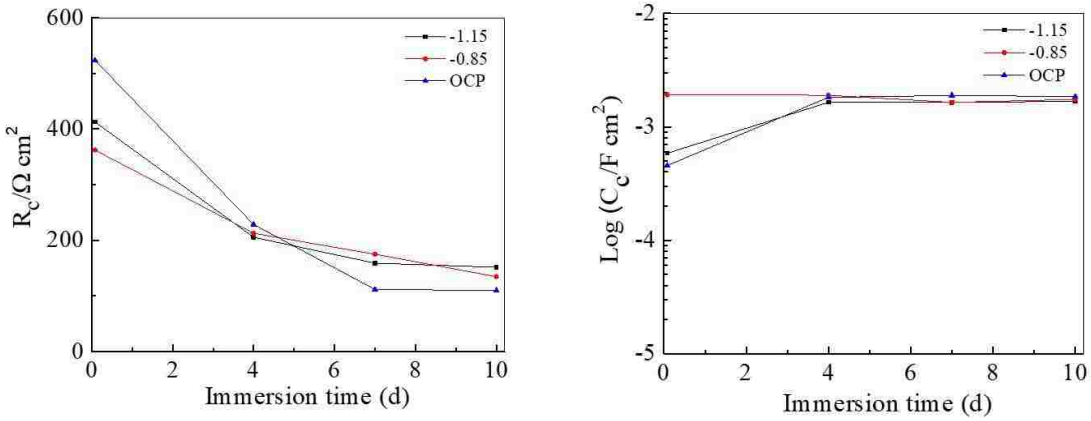

(a) (b)

Figure 6.7. Damaged coating properties: (a) pore resistance R_c and (b) capacitance CPE_c.

The R_c values of the damaged coating decreased rapidly over immersion time in days. Specifically, the R_c value of the samples under the CP dropped from approximately

400 Ω cm^2 to 150 Ω cm^2 while the R_c value of the sample under the OCP reduced more dramatically from 500 Ω cm^2 in one day to 110 Ω cm^2 in 10 days, indicating the failure of coating in protecting the substrate steel. The CPE_c values of all the tested samples reached nearly the same value of 2 mF· cm^2 after 4 days of immersion. Therefore, after coating has damaged, the CP has little effect on the coating performance.

Figure 6.8 displays the properties of the steel-electrolyte interface under intact coating: charge transfer resistance R_{ct} and double layer capacitance CPE_{dl}. The charge transfer resistance is the resistance against electrons transferring across the steel surface, which is inversely proportional to the corrosion rate [23]. For the samples tested under -1.15 V/SCE, -0.85V/SCE and the OCP, the charge transfer resistances were reduced to 1.13 GΩ cm^2, 0.7 GΩ cm^2, and 0.14 GΩ cm^2, respectively, at the end of tests in 70 days. This comparison indicated increasing electrochemical reactions on the steel-electrolyte interface over time as the level of CP decreased.

The double layer capacitance CPE_{dl} is also a measure of the ease of charge transfer across the steel-electrolyte interface. The CPE_{dl} of the samples tested under -1.15 V/SCE, -0.85V/SCE and the OCP were increased to 6.523×10^{-11} F cm^{-2}, 1.613×10^{-10} F cm^{-2}, and 4.314×10^{-10} F cm^{-2}, respectively, at the end of tests in 70 days. The sample tested under -1.15 V/SCE has the highest charge transfer resistance and the lowest double layer capacitance. Thus, the higher the cathodic potential, more effectively the electrochemical reactions can be delayed at the steel-electrolyte interface [30].

After enamel coating was damaged, as shown in Figure 6.9, the charge transfer resistances of the samples tested under -1.15 V/SCE, -0.85V/SCE and the OCP slightly decreased to 4.96×10^5 Ω cm^2, 3.78×10^5 Ω cm^2, and 6.67×10^4 Ω cm^2 after 10 days of

immersion, respectively, which is about 10^4 times smaller than that of the intact coating tested after 70 days of immersion. The double layer capacitances of the samples tested under -1.15 V/SCE, -0.85V/SCE and the OCP also changed slightly, which are 1.37×10^{-4} F cm^{-2}, 6.08×10^{-4} F cm^{-2}, and 5.48×10^{-4} F cm^{-2} after 10 days of immersion, respectively. They are approximately 10^6 times larger than those of the samples with intact enamel coating tested after 70 days of immersion.

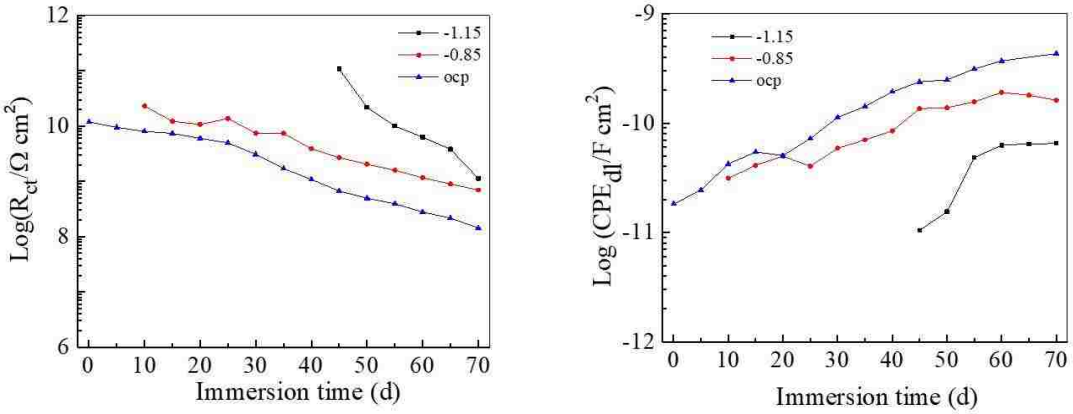

(a) (b)

Figure 6.8. Properties of the steel-electrolyte interface under intact enamel coating: (a) charge transfer resistance R_{ct} and (b) double layer capacitance CPE_{dl}.

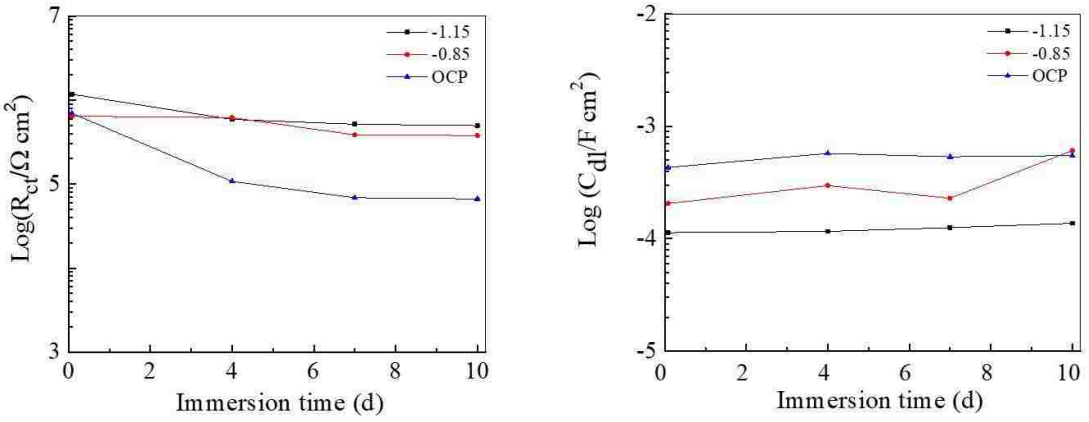

(a) (b)

Figure 6.9. Properties of the steel-electrolyte interface under damaged enamel coating: (a) charge transfer resistance R_{ct} and (b) double layer capacitance CPE_{dl}.

6.3.3. Potentiostatic. Figure 6.10(a) shows the variation of current taken from the intact enamel coating zone under -0.85 vs. SCE/V and -1.15 vs. SCE/V. Each dot represents one measurement data per day till the end of tests in 70 days. The current fluctuated around -0.2 nA from the beginning to 45 days of immersion for both samples. Then, the sample tested under -1.15 V/SCE decreased slowly to approximately -0.3 nA at the end of tests while the sample tested under -0.85 V/SCE decreased dramatically to approximately -0.8 nA at the end.

Similarly, Figure 6.10(b) presents the variation of current on the samples with the damaged enamel coating. The currents of both samples eventually reached to approximately -5 μA after 10 days of immersion, which are about 10^4 times larger than those of the respective tested samples with the intact enamel coating as more electrochemically reactive spots are generated. In all test cases, the measured current is always negative, implying that the CP current can flow through the coating along electrolyte pathways to reach the metal substrate and protect the steel from corrosion [61].

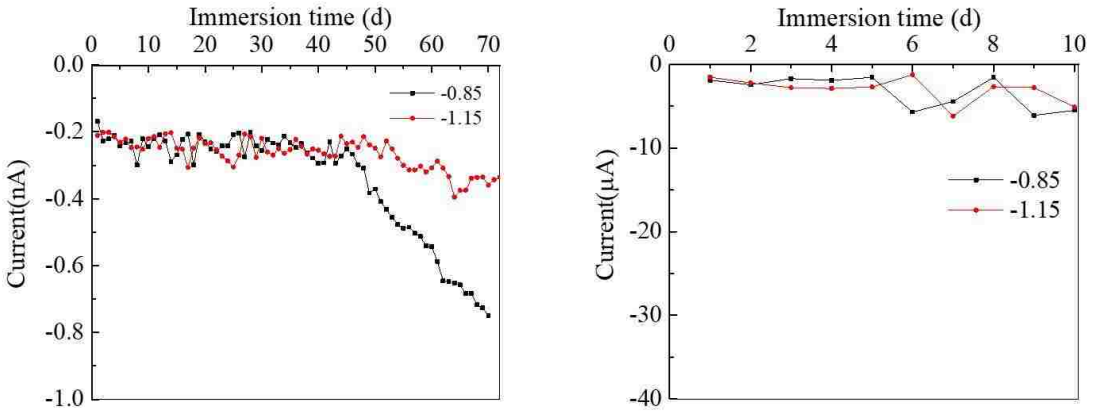

(a) (b)

Figure 6.10. Variation of current measured on various samples under -0.85 vs. SCE/V and -1.15 vs. SCE/V: (a) intact coating zone and (b) damaged coating zone.

6.3.4. Visual Observations after Corrosion Test. At the conclusion of corrosion tests, the damaged spots of all tested samples were examined visually as shown in Figure 6.11. No corrosion products were observed on the damaged surface under the cathodic potential of -1.15V/SCE. Brown corrosion products can be clearly seen on the damage point of the samples tested under the OCP.

(a) (b) (c)

Figure 6.11. Damaged surface conditions of the samples tested under (a) -1.15 vs. SCE/V, (b) -0.85 vs. SCE/V and (c) the OCP after corrosion tests.

6.4. SUMMARY

Based on the experimental results and analysis from one representative sample in each test condition, the following conclusions can be drawn:

1. Enamel residuals remained between anchor points of the substrate steel after the enamel coating had been chipped off due to impact loading. During all the corrosion tests, no further delamination was found, and the CP did not change the coating properties and the mechanical condition at the coating-substrate interface.
2. At the intact coating areas, the higher potential (up to -1.15 V/SCE) applied in CP, the higher the coating resistance and charge transfer resistance. The CP

does not cause debonding between the coating and its steel substrate, decelerates the degradation process of the coating and delay the electrochemical reactions at the steel-electrolyte interface.

3. The resistances of all the damaged coatings are less than 1k Ω cm^2, indicating the loss of their barrier effect in protecting the substrate steel from corrosion. The introduction of CP does not improve the coating performance once damaged.
4. The resistances against electrolyte penetration into the enamel coating and charge transfer through the steel-electrolyte interface in the intact and damaged enamel coating areas differed by at least 10^4 times after 70 days of test. It is thus important to separate the electrochemical processes in the intact and damaged zones during corrosion tests.

7. STRESS DISTRIBUTION IN ENAMEL-COATED PIPELINES UNDER THERMAL EFFECT, EXTERNAL PRESSURE, AND INTERNAL PRESSURE

7.1. BACKGROUND

An existing pipeline is usually buried underground and subjected to external forces from top 1~2 m soils and ground movement. During operation, the steel pipe is also subjected to internal pressure from the transported oil or gas. When internally enameled at high temperature, thermal stress can retain in enamel coating and steel pipe since the coating material is inevitably dissimilar to its substrate steel. If the residual stress exceeds chemical adhesion at the enamel-steel interface, the coating will delaminate from its substrate and thus promote under-film corrosion.

Both residual thermal stress and stress concentration can contribute to the stress corrosion cracking (SCC) of enamel-coated steel pipes in an even mildly corrosive environment. SCC can lead to an unexpected sudden failure of steel pipes subjected to tensile hoop stress under internal pressure. Therefore, it is important to understand the thermal stress distribution of enamel-coated pipelines and control residual stress at the enamel-steel interface within the interfacial shear strength in order to ensure the durability of enameled pipelines. Due to excavation or other reasons, thin wall of the existing pipelines is sometimes uneven and not smooth prior to enamel coating. In this case, the stress concentration may occur around various dents due to thermal effect and internal pressure. Therefore, the stress concentration of the overall pipeline under residual thermal stress, internal pressure, and external pressure must be studied to ensure the safety of pipelines. In this study, a finite element model of enamel-coated steel samples is developed

using the commercial software ABAQUS to understand the effect of enameling process on the residual thermal stress in the enamel coating and the steel substrate. The model is also used to understand the effect of a surface dent on the stress concentration of the enamel-coated samples under the residual thermal stress, internal pressure, and external pressure. Parametric studies are conducted to ensure that the model is convergent and reliable as the element size is reduced, and the coating thickness is changed.

7.2. FINITE ELEMENT MODEL

7.2.1. Enameling Process. Enamel bonds to steel at a temperature of 830 °C for 10 min. The enameling process can be divided into a firing process and a cooling process. During the firing process, enamel powder dry-sprayed on steel will not chemically react with steel until the powders behave as viscous fluids at 830 °C. Hence, the powders will not affect the thermal deformation of the steel substrate. During the cooling process, residual thermal stress is generated between the enamel and its steel substrate due to any mismatch of the coefficient of thermal expansion as shown in Figure 7.1. Since the coefficient of thermal expansion of enamel is smaller than that of steel, the enamel and the steel will be in compression and tension, respectively, as the temperature cools down to 25 °C. The initial compression can prevent enamel coating from cracking under normal operation.

Consider a 3-m long steel pipe internally coated with porcelain enamel. The steel pipe has an outside diameter of 323.850 mm and a wall thickness of 9.525 mm. The enamel coating is considered to be 0.1 mm, 0.2 mm, and 0.4 mm thick in order to study its effect on the residual thermal stress. The enamel-coated pipe was discretized into meshes and

modelled using three-dimensional hexahedral eight-node (C3D8R) elements in ABAQUS. In particular, eight elements were used to simulate the pipe wall in radial direction so that each pipe element is 1.191 mm thick. In circumferential direction, each pipe element is a square in shape. Similarly, four elements were used to simulate the enamel coating in radial direction so that each coating element is a square shell of 0.025 mm, 0.05 mm or 0.1 mm thick. All the elements were subjected to an identical temperature condition that represents the enameling process. In the firing process, the steel pipe was linearly heated from room temperature (25 °C) to 830 °C in 26 s [62]. An enamel coating layer in viscous fluid state was then created on the thermally deformed model of the pipe at 830 °C, which was then cooled down at a uniform rate to room temperature in 26 s.

Enamel powder was assumed to attach to its steel substrate with no stress until the powder was melted, cooled, and perfectly bonded to the steel. Specifically, the enamel remained no stress above a glass softening temperature of 550 °C because it behaved like a viscous fluid [63]. Its Young's modulus was thus assumed to be zero above 550°C. Figure 7.2 shows the Young's modulus for the steel pipe and enamel coating [62-63].

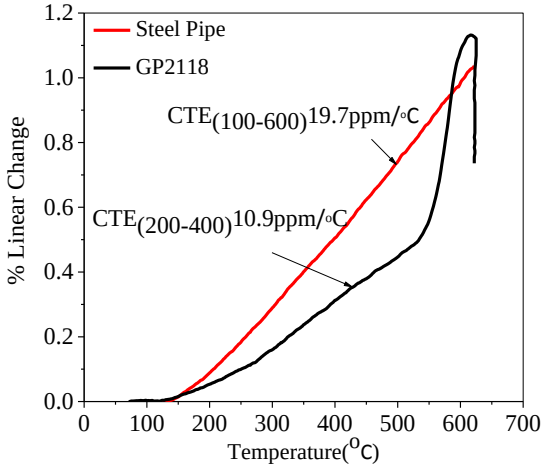

Figure 7.1. Coefficients of thermal expansion of enamel and steel.

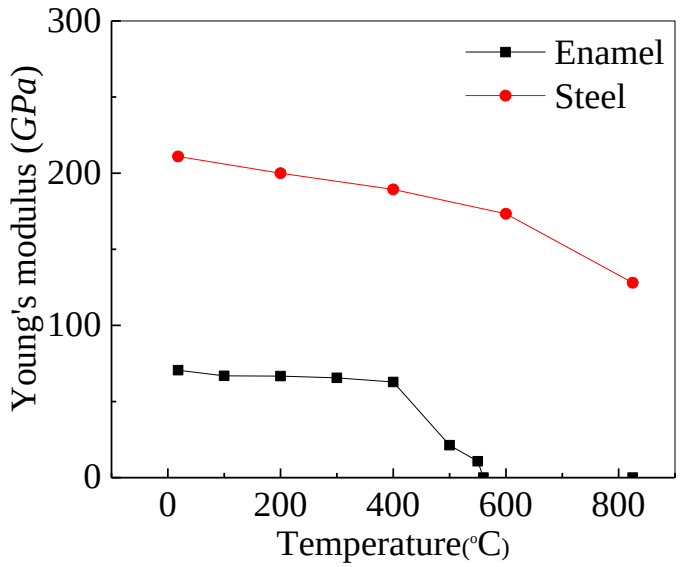

Figure 7.2. Young's modulus of enamel coating and steel at elevated temperature.

In this study, the mesh size (a) was taken from 40 to 20 mm in 10 mm increment to ensure that the model was convergent and stable. Based on the sensitivity study, the final mesh size was set to be a = 20 mm in mid-thickness plane of the pipe wall. Figure 7.3 shows the mesh model of a steel pipe internally coated with enamel (0.2 mm thick) with a total number of 26264 elements.

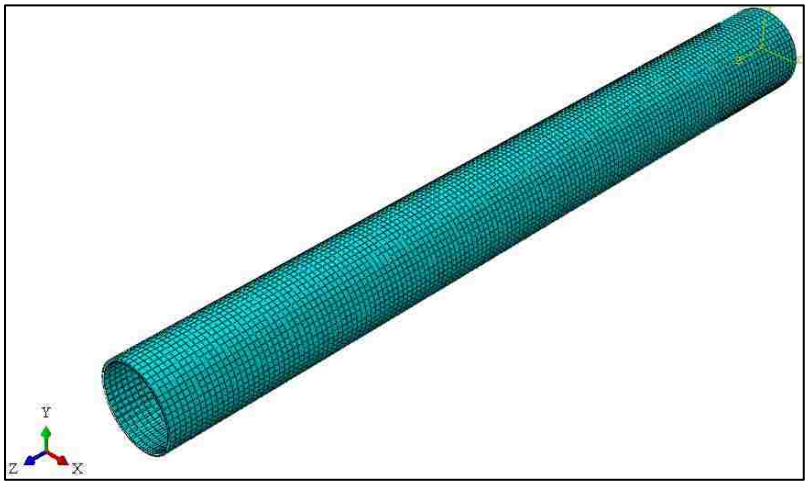

Figure 7.3. ABAQUS mesh model of a steel pipe internally coated with enamel.

7.2.2. Steel Pipe with a Locally Reduced Thickness. Locally reduced pipe wall thickness was taken into account to represent the mechanically induced dents prior to enameling. The so-called defect may cause local stress concentration. In the finite element model, the defect was simulated by removing elements. Specifically, an 80 mm long and 1.191 mm deep defect was considered in the simulation. Figure 7.4 shows the mesh model of the steel pipe internally coated with enamel (0.2 mm thick) when the mesh size of the pipe wall in mid-thickness was set to be a = 20 mm.

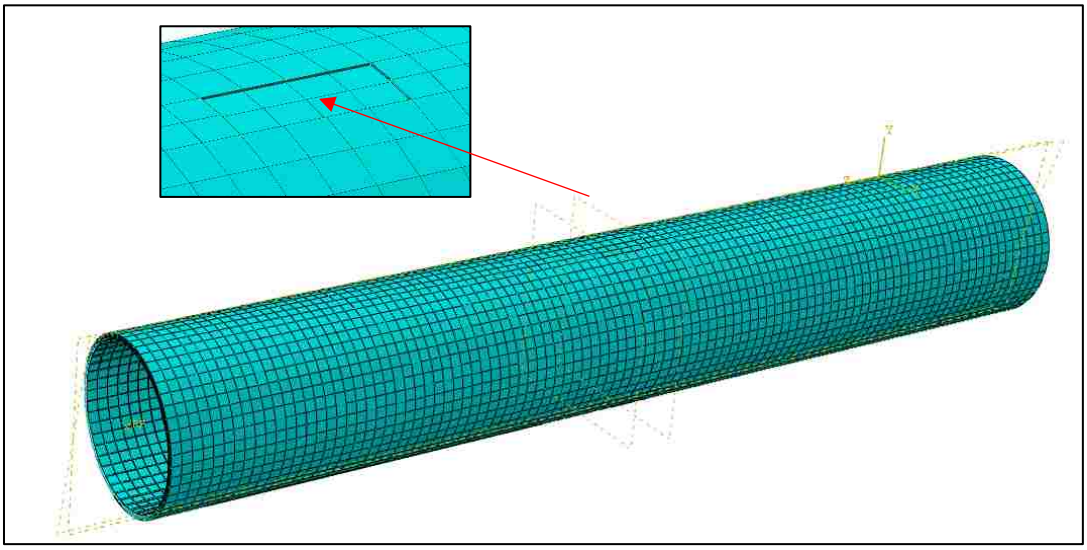

Figure 7.4. ABAQUS mesh model of steel pipe with surface defect.

7.2.3. Loading Condition of a Steel Pipe. During operation, the internal pressures of a steel pipe are usually 15, 20 or 25 MPa, which correspond to a pipe hoop stress of 255, 340, or 425 MPa and thus represent 46%, 62% and 77% of the specified minimum yielding strength of the steel, respectively [64]. Underground pipelines are also subjected to soil induced strains due to ground movement, which usually ranges from 0 to 2.5% [64].

In the finite element model, the internal pressure of the pipe was set to be 0, 5, 10, 15, 20 and 25 MPa. A 0.2% tensile and compressive strain was applied on the cross section of the pipe wall or in axial (longitudinal) direction of the steel pipe to simulate the soil-induced strain due to ground movement. After each analysis, minimum principal stress in the enamel coating will be checked to understand the residual thermal stress. The von Mises stress at the defect of the pipe will be checked to understand the level of stress concentration under the combined effect of the residual thermal stress, internal pressure and external pressure.

7.3. RESULTS AND DISCUSSION

7.3.1. Residual Thermal Stress. Table 7.1 shows a summary of the largest value of minimum principal stresses at the interface between the enamel coating and steel. Figure 7.5 to Figure 7.13 show the minimum principal stress of internal enamel coating with different mesh sizes and coating thicknesses. Overall, the minimum principal stress in the enamel coating is approximately -2.5 MPa (compression). The enamel coating thickness and mesh size have insignificant influences on the residual stress. This is mainly because the steel pipe (9.525 mm) is 48 times thicker than the enamel coating (200 μm).

Table 7.1. The minimum principal stress (MPa) of internal enamel coating layer.

Element size (m) / Coating thickness (μm)	0.04	0.03	0.02
100	-2.55	-2.46	-2.46
200	-2.51	-2.47	-2.48
400	-2.49	-2.49	-2.50

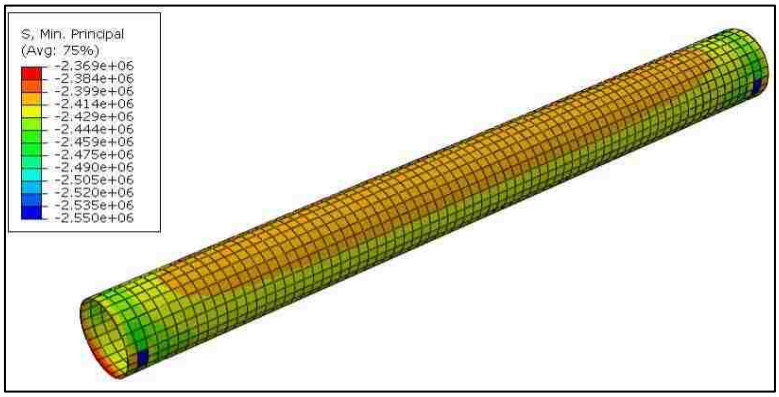

Figure 7.5. Minimum principal stress of internal enamel coating with a mesh size of 40 mm and a coating thickness of 0.1 mm.

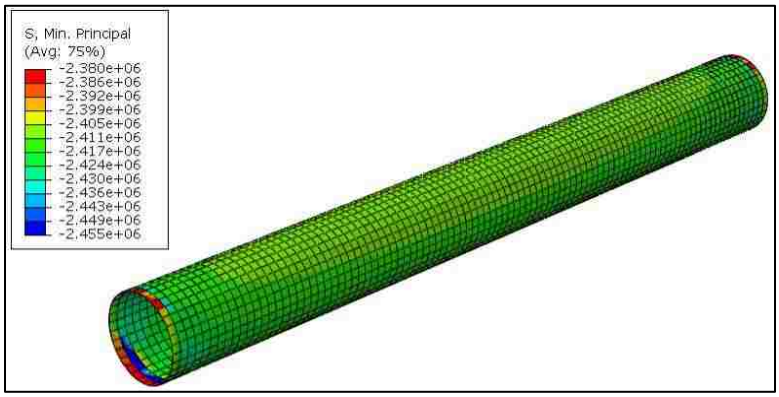

Figure 7.6. Minimum principal stress of internal enamel coating with a mesh size of 30 mm and a coating thickness of 0.1 mm.

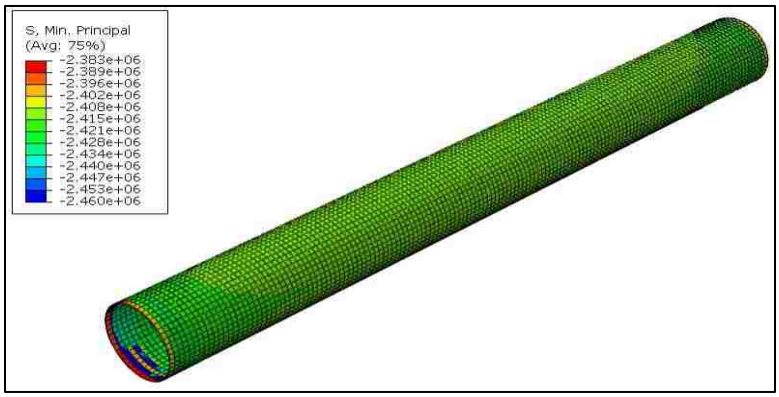

Figure 7.7. Minimum principal stress of internal enamel coating with a mesh size of 20 mm and a coating thickness of 0.1 mm.

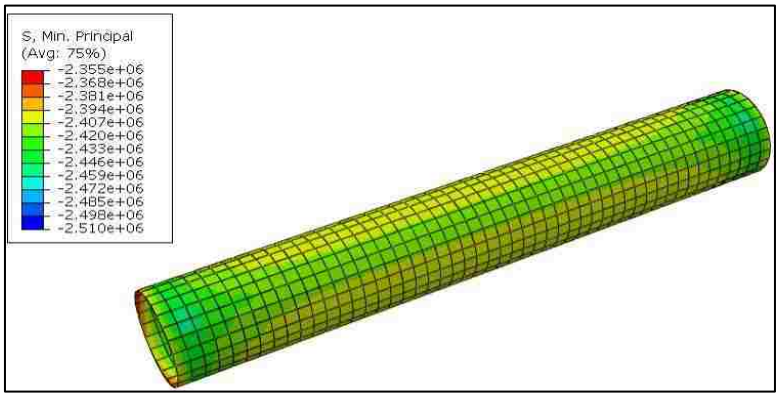

Figure 7.8. Minimum principal stress of internal enamel coating with a mesh size of 40 mm and a coating thickness of 0.2 mm.

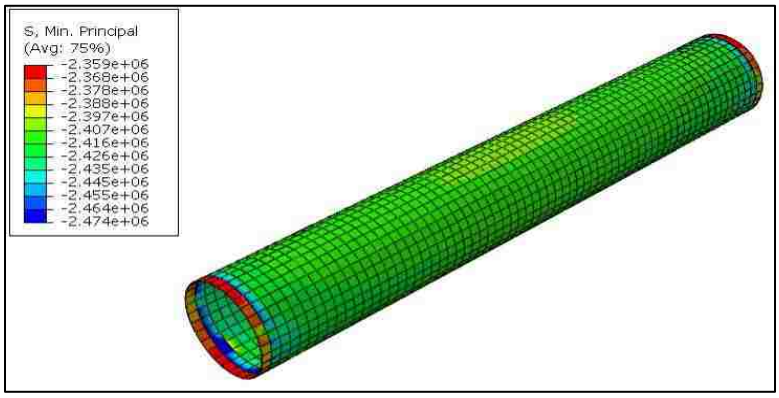

Figure 7.9. Minimum principal stress of internal enamel coating with a mesh size of 30 mm and a coating thickness of 0.2 mm.

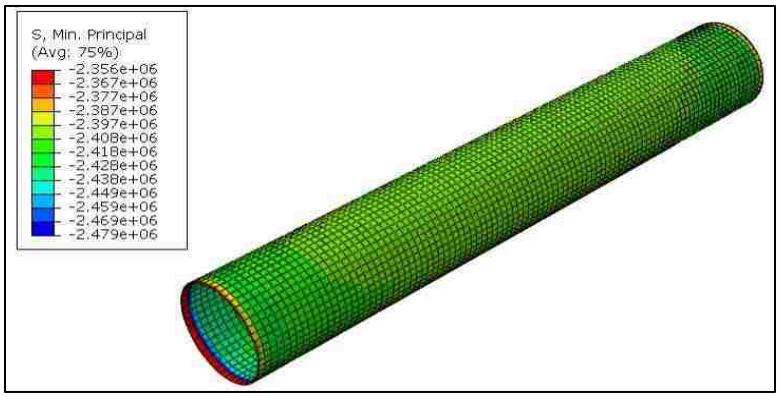

Figure 7.10. Minimum principal stress of internal enamel coating with a mesh size of 20 mm and a coating thickness of 0.2 mm.

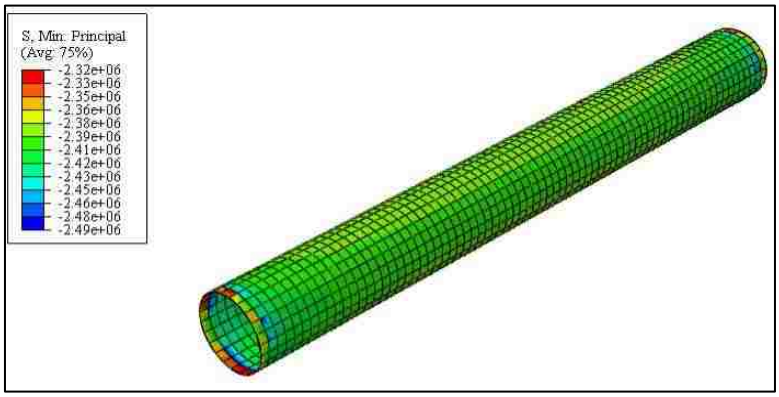

Figure 7.11. Minimum principal stress of internal enamel coating with a mesh size of 40 mm and a coating thickness of 0.4 mm.

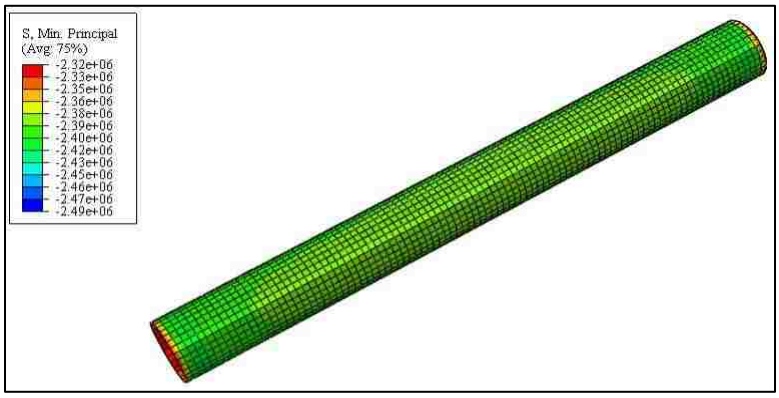

Figure 7.12. Minimum principal stress of internal enamel coating with a mesh size of 30 mm and a coating thickness of 0.4 mm.

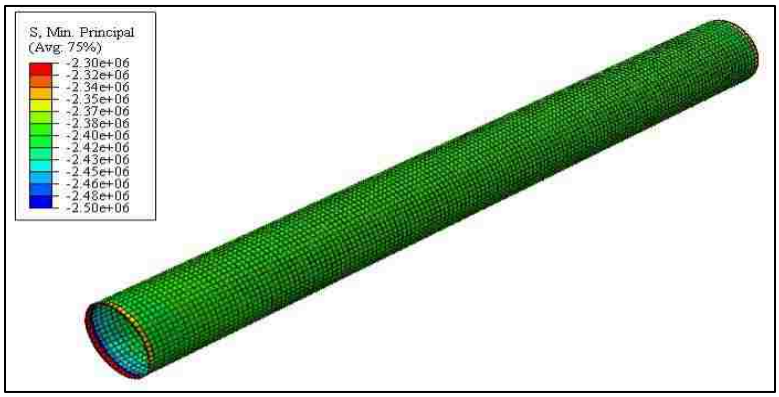

Figure 7.13. Minimum principal stress of internal enamel coating with a mesh size of 20 mm and a coating thickness of 0.4 mm.

The minimum principal stress represents the residual thermal stress in the coating. The stress distributes uniformly along the longitudinal direction of the steel pipe except at both ends of the pipe. Since the residual stress is so small, enameling basically has no effect on the steel. Steel deforms little during the enameling process since steel is much thicker than the coating layer. Thermal heat can be conducted quickly to the surrounding area. Based on the previous pull-off test, the bond strength between the coating and the steel ranged from 16.12 MPa to 18.73 MPa. The maximum thermal residual stress is 2.55 MPa, which is much smaller than that of the chemical adhesion between the enamel and steel. Thus, the coating will not delaminate from its substrate during operation.

7.3.2. Stress Distribution on a Pipe Containing a Local Defect. Figure 7.14 and Figure 7.15 show the stress distribution of the steel pipe model containing a local defect under a combined effect of residual thermal stress, external soil strain, and internal pressure. The external soil strain considered is compressive in Figure 7.14, and tensile in Figure 7.15.

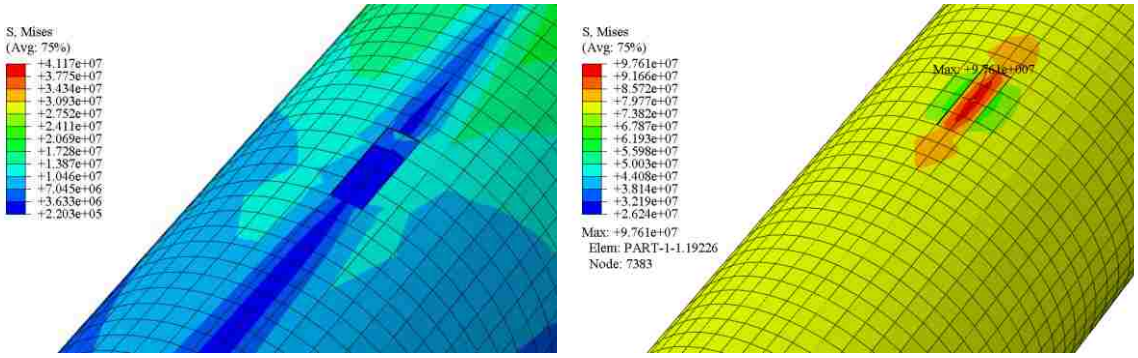

(a) Internal pressure 0 MPa (b) Internal pressure 5 MPa

Figure 7.14. Distribution of stress on the defected pipe with a compressive soil strain of 0.2% and various internal pressures of 0, 5, 10, 15, 20 and 25 MPa for (a) to (f).

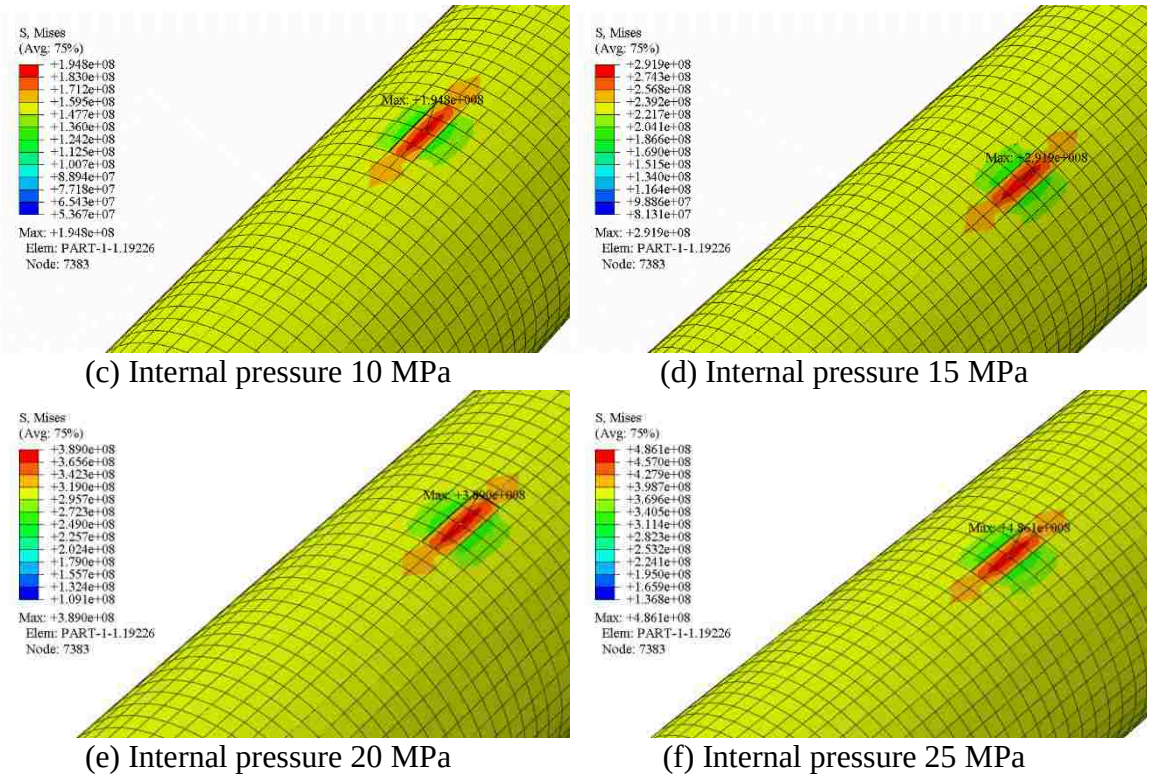

(c) Internal pressure 10 MPa (d) Internal pressure 15 MPa

(e) Internal pressure 20 MPa (f) Internal pressure 25 MPa

Figure 7.14. Distribution of stress on the defected pipe with a compressive soil strain of 0.2% and various internal pressures of 0, 5, 10, 15, 20 and 25 MPa for (a) to (f) (cont.).

It can be seen that the stress distribution around the defect is not uniform. The propagation of the stress distribution in longitudinal direction is different from that in circumferential direction. The highest stress concentration occurs at the center of the defect. The stress concentration is zero, when the internal pressure is zero, and increases with the internal pressure regardless whether the external soil strain is in tension or compression. This stress concentration may result in a rapid fracture of the pipe wall if the local stress exceeds the material strength.

The internal pressure has a large impact on the stress concentration as shown in Figure 7.16. With the increase of internal pressure, the stress concentration increases

linearly to approximately 480 MPa under an internal pressure of 25 MPa, which is close to the yield strength of the pipe steel. Further increase in internal pressure will put the pipe into the plastic stage and later may induce cracking at the defect. The stress concentration at the defect can contribute to stress corrosion cracking even in mildly corrosive environment, which can lead to an unexpected sudden failure of steel pipe during operation.

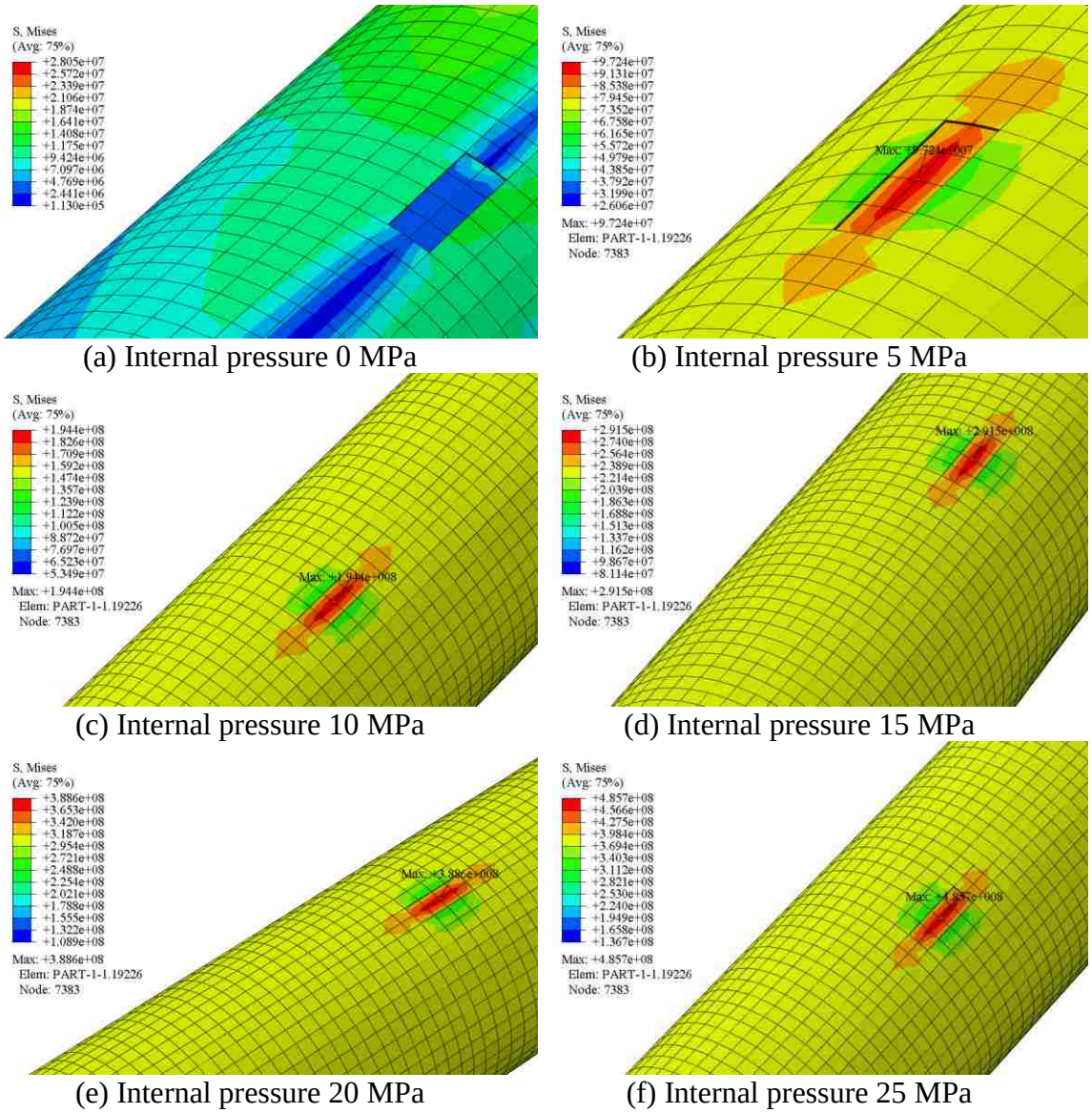

(a) Internal pressure 0 MPa (b) Internal pressure 5 MPa

(c) Internal pressure 10 MPa (d) Internal pressure 15 MPa

(e) Internal pressure 20 MPa (f) Internal pressure 25 MPa

Figure 7.15. Distribution of stress on the defected pipe with a tensile soil strain of 0.2% and various internal pressures of 0, 5, 10, 15, 20 and 25 MPa for (a) to (f).

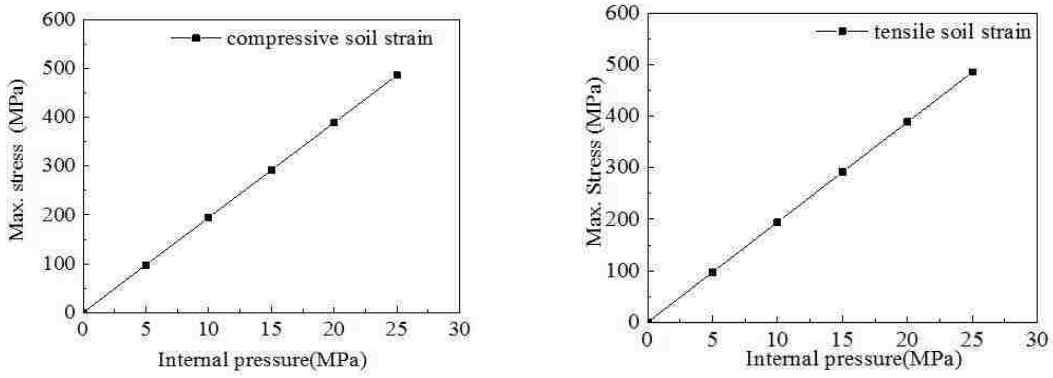

(a) (b)

Figure 7.16. Maximum stress of the steel pipe as a function of internal pressure.

7.4. SUMMARY

Based on the extensive finite element analysis, the following conclusions can be drawn:

1. The thermal residual stress in the enamel coating distributes uniformly along the longitudinal direction of the steel pipe except at its both ends. The maximum thermal residual stress is 2.55 MPa, which is much smaller than that of the chemical adhesion between the enamel and the steel. Thus, the coating will not delaminate from its substrate after the enameling process.
2. The maximum stress increases linearly with the internal pressure, reaching approximately 480 MPa at an internal pressure of 25 MPa, which is close to the yield strength of the steel pipe.

8. STRESS CORROSION CRACKING OF ENAMEL-COATED STEEL PIPES UNDER CATHODIC PROTECTION IN AN ALKALINE SOIL ENVIRONMENT

8.1. BACKGROUND

Stress corrosion cracking (SCC) is a cracking process of susceptible metals under a simultaneous action of corrosive environment and sufficient tensile stress. It poses a great threat to the safe operation of pipelines and has, since 1965, contributed to major failures in pipelines around the world [65]. The buried pipelines have generally experienced two main forms of SCC: high-pH and near-neutral pH SCC [66]. The high-pH SCC develops in a high-pH carbonate-bicarbonate electrolyte under a disbonded coating due to the CP (cathodic polarization)-driven cathodic reduction of water and the generation of hydroxyl ions [67]. At the early stage of coating disbondment, corrosion pits initiated due to the presence of Cl^-, which prevents the formation of stable passivation and increases the anodic sensitivity of steel [68, 69]. The corrosion pits increase the stress concentration, which facilitates the transformation from a pit to crack [70]. Then the stress will concentrate at the crack tips, rupture the passive film over the crack tips and activate dislocation to form slip bands or dislocation pile-ups, which significantly promotes crack propagation [67, 71].

The nearly neutral-pH SCC of pipelines develops in anaerobic, diluted groundwater containing primarily bicarbonate ions due to ineffective CP to the pipe surface [72]. SCC colonies are initiated on the outside surface with pitting due to the fluctuation of cathodic potential [73-78]. The fluctuation results in a temporary anodic potential field and leads to anodic dissolution at local defects, thus initiating the corrosion pits [79]. During SCC, the crack tips have always been closed to fresh, bare steel while the crack wall is covered with

a corrosion products layer, which enhances the anodic dissolution and hydrogen evolution [79-82]. A critical hydrogen concentration results in steel embrittlement and promotes crack propagation [83].

Cathodic protection applied to the pipeline surface is a factor that influences the SCC mechanism [84, 85]. More internal cracks were seen in the steel with the highest level of cathodic protection applied, contributing to cracking associated with the so-called hydrogen embrittlement effect. The aim of this work is to evaluate the effect of cathodic polarization on the SCC of API X65 steel pipelines in terms of mechanical and electrochemical behavior in a simulated soil environment with a pH of 10 at room temperature. Relation between the mechanical properties and susceptibility to SCC is established.

8.2. MATERIALS AND METHODS

8.2.1. XRD. The API 5L X65 steel pipe has an external diameter of 323.850 mm and wall thickness of 9.525 mm. The steel pipe was cut into two small samples, 1 cm × 1 cm in size. One of the samples was then coated with enamel GP2118. The enameled steel sample and the as-received sample were polished up to 1200 grit finish to expose the shining steel surface. The phases were examined on the polished surface of the as-received steel and the enameled steel by X-ray diffraction (XRD, Philip X' Pert) with a diffraction angle (2θ) of 10° to 90°.

8.2.2. Potentiodynamic Test. The potentiodynamic tests of enameled steel were conducted in a simulated alkaline soil solution at a scan rate of 50 mV/s and 0.5 mV/s, respectively, to investigate the electrochemical polarization on the occurrence of stress

corrosion cracking (SCC). Two small samples were cut from the enameled steel pipe and used as the working electrodes. One surface of the samples was polished up to 1200 grit finish to expose the shining steel surface. The samples were covered with Marine epoxy except the polished surface with an exposed working area of 1.0 cm2. A saturated calomel electrode (SCE) was used as the reference electrode and a Pt plate as the counter electrode. All three electrodes were connected to an Interface1000E Potentiostat (Gamry Instrument) for data acquisition. The potentiodynamic tests were conducted from Eocp -300 mV to Eocp +1500 mV after the open circuit potential (OCP) had reached a stable value. The simulated ground water solution (NS4) was used to simulate a corrosive environment. The pH of the solution was adjusted to 10 by adding NaOH. Table 8.1 shows the chemical composition of the NS4 solution used in this study.

Table 8.1. Chemical composition of the NS4 solution (g/l).

$NaHCO_3$	$CaCl_2 \cdot H_2O$	$MgSO_4 \cdot 7H_2O$	KCl
0.483	0.181	0.131	0.122

8.2.3. Slow Strain Rate Test. Slow strain rate tests (SSRT) were carried out on smooth cylindrical tensile samples inside the autoclave as shown in Figure 8.1. The enameled steel pipe was cut into coupons and then machined according to the ASTM E8 Standard [86]. The sample surface in the gauge section was polished up to 1200 grit finish in the loading direction of the SSRT. This ensured similar surface conditions for all tests. The INSTRON 5965 load frame was used to perform the SSRT at a strain rate of 0.000254 mm/s. All the tests were carried out at room temperature. After all the coupons tests had been completed in air and at different cathodic potentials, the fracture surfaces of the

coupons were examined using scanning electron microscopy (SEM) to study the SCC susceptibility.

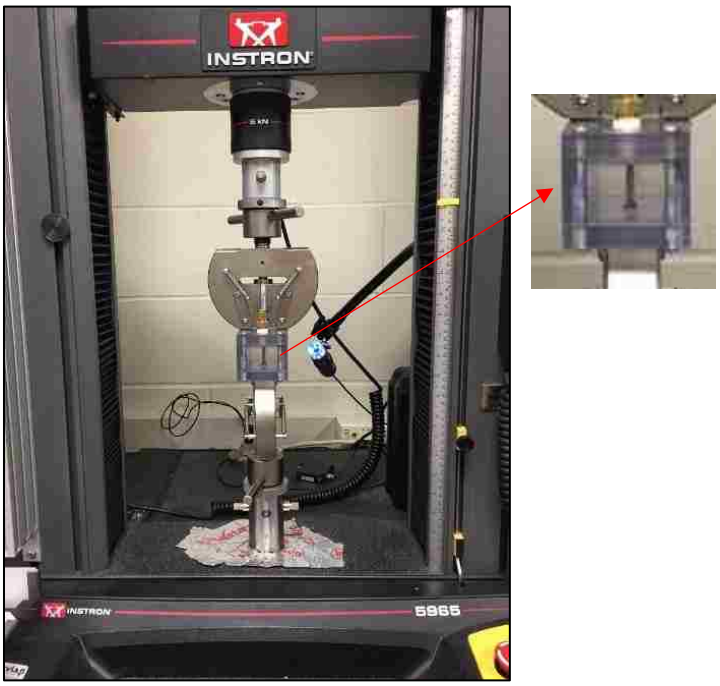

Figure.8.1. Glass autoclave and INSTRON5965 load frame used to perform the SSRT in the NS4 solution.

8.2.4. Electrochemical Impedance Spectroscopy. The electrochemical tests were performed simultaneously with the SSRTs on the same coupon samples in the autoclave with an Interface1000E Potentiostat (Gamry Instrument). A standard three-electrode system was used with the cylindrical tensile sample as the working electrode, a platinum sheet as the counter electrode, and an Ag/AgCl electrode as the reference electrode. The electrochemical impedance spectroscopy (EIS) measurements were taken at different impressed potentials. In all EIS tests, a sinusoidal wave of potential (10 mV in amplitude) with a frequency of 0.01 Hz to 10 kHz was used. Ten points per decade

(sampling rate) were recorded. The EIS was obtained after stationary conditions have been reached and measurements continued till the failure of each SSRT specimen.

8.3. RESULTS AND DISCUSSION

8.3.1. XRD. Figure 8.2 shows the XRD patterns for the as-received steel and the enameled steel. They have the same ferrite microstructure based on the XRD test results, which is due to a short time duration at the firing temperature.

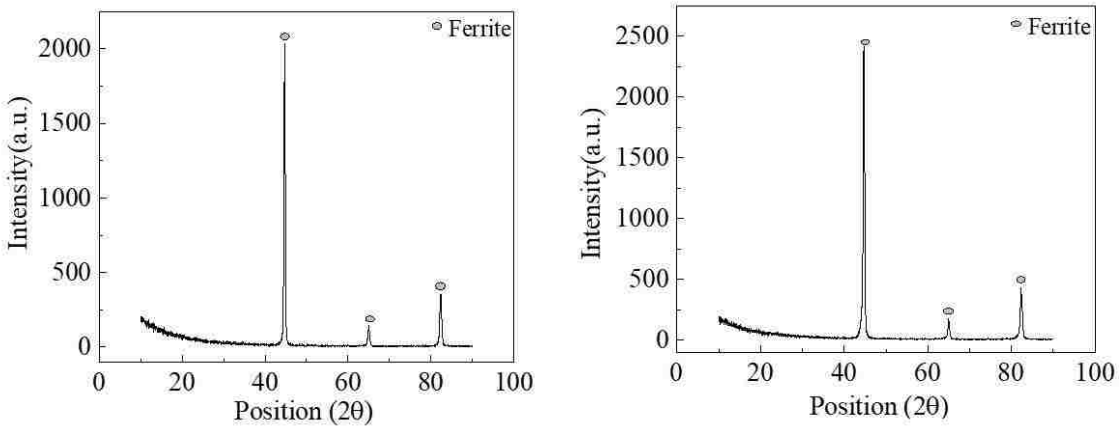

Figure 8.2. XRD patterns for (a) as-received steel and (b) enameled steel.

8.3.2. Potentiodynamic Test. Figure 8.3 compares the two polarization curves measured at fast and slow scanning rates. It can be seen from Figure 8.3 that the null-current positions divide the potential range into three zones. The so-called anodic reaction dominates Zone I (> -0.75V), the cathodic reaction dominates Zone III (< -0.833 V), and both the anodic and cathodic reactions co-exist in Zone II (-0.75 V ~ -0.833V). The open circuit potential was measured to be approximately -0.68 V, which falls in Zone I. The

cathodic potentials chosen in SSRTs are -0.79 V/SCE in Zone II, and -0.90 V/SCE and -1.20 V/SCE in Zone III.

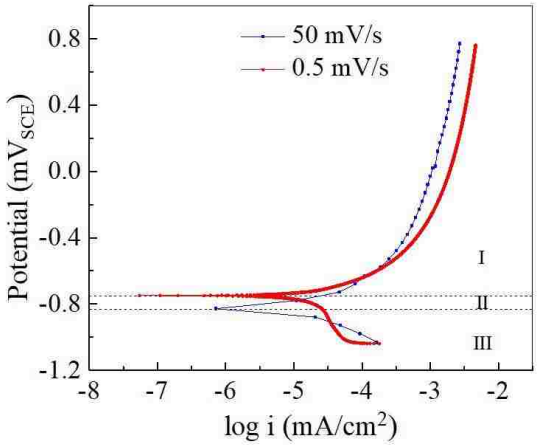

Figure 8.3. Polarization curves of the steel samples measured at high (50 mV/s) and low (0.5 mV/s) potential scanning rates in NS4 solution.

8.3.3. Slow Strain Rate Test. Figure 8.4 shows the stress-strain curves of X65steel obtained from the SSRTs with different applied potentials in alkaline soil solution. Table 8.2 shows a summary of the mechanical properties related to the SCC susceptibility.

When the coupon samples were tested in the solution, both the yield strength and the ultimate strength increased. The yield strength and ultimate strength of the sample tested under the open circuit potential (OCP) were higher than those of the sample tested in air. An obvious passive film was observed on the surface of the sample tested under the OCP. Such a passive film likely delayed the initiation of crack on the surface of a coupon sample, thus requiring a higher tensile stress to rupture the sample under test. This result represented a combined action of anodic dissolution at grain boundaries and tensile stress. The sample tested under the OCP had relatively higher yield strength and ultimate strength

than those tested under cathodic potentials because passive films were less likely formed on the surface of the samples tested under cathodic potentials. The enhanced strength of the steel coupons tested under cathodic potentials in the alkaline solution than in air was attributed to the fact that hydrogen atoms penetrated into the steel and block the dislocation movement [87]. The steel sample was thus hardened with reduced ductility.

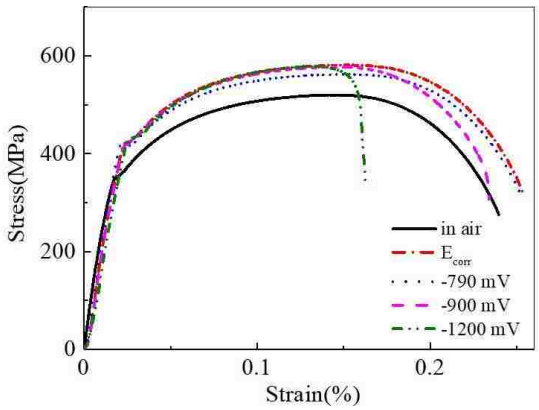

Figure 8.4. Stress vs. strain curves obtained from SSRTs.

Table 8.2. Summary of the mechanical properties obtained from SSRTs.

Condition	Yield strength (YS) (MPa)	Ultimate strength (US) (MPa)	Plastic elongation (mm)	Plastic strain (%)	Time to failure (s)
in Air	351	520	3.63	0.20	44340
OCP	421	581	4.26	0.23	47040
-0.79 V	411	562	4.25	0.23	46830
-0.90 V	419	577	3.89	0.21	43305
-1.20 V	417	578	2.51	0.14	30045

Since the INSTRON loading frame measures the displacement of its crosshead, the plastic elongation of a sample was used to limit the displacement in the shoulders of the

sample [88]. The plastic elongation of the sample tested under the OCP was close to that under a cathodic potential of -0.79 V. The plastic elongations and the time to failure of the samples tested under cathodic potentials decreased as the cathodic potential decreased, indicating more serious hydrogen embrittlement at the more negative cathodic potential. Figure 8.5 shows the dependence of change in cross-sectional area on the applied potential of steel coupon samples in the alkaline NS4 solution. The reduction in cross-sectional area (RA in %) is defined as [88]:

$$RA(\%) = \frac{D_I^2 - D_F^2}{D_I^2} \times 100 \tag{8.1}$$

where D_I and D_F represent the initial and final gauge section diameter at the fracture location. When the tensile tests were performed in air, the RA was measured to be 81.8%, which is larger than all the other samples tested in the solution. This indicated that the X65 steel was susceptible to environmentally assisted cracking, depending on the applied potential. The more negative the applied potential, the higher susceptibility to SCC the X65 steel in the simulated solution.

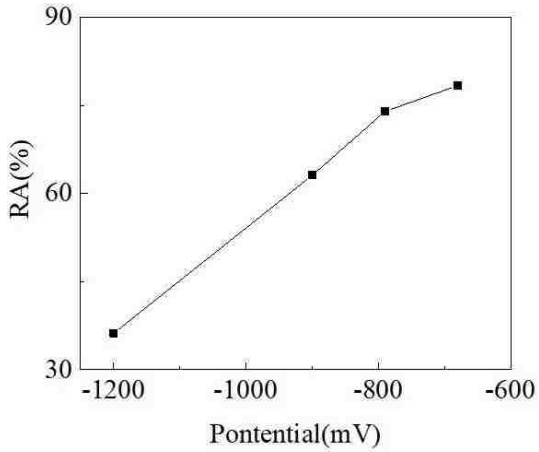

Figure 8.5. Dependence of RA on the applied potential of steel coupon samples in alkaline NS4 solution.

The relationship between the SCC susceptibility of the steel under cathodic potentials and the electrochemical reaction mechanism is presented in Figure 8.6. When the applied potential falls in Zone I, the polarization curves measured at both low and fast scanning rates are within the anodic polarization range, indicating that the cracking process is controlled by the anodic dissolution (AD).

When the applied potential falls in Zone III, both polarization curves are in the cathodic polarization range. The cathodic reaction charges hydrogen to the steel, causing embrittlement. Therefore, the SCC is referred to as a hydrogen embrittlement (HE) mechanism. When the applied potential falls in Zone II, the steel is in non-equilibrium state. The steel is in cathodic polarization when the scan rate is low, and in anodic polarization when the scan rate is high. In this case, the SCC is due to a combination of anodic dissolution and hydrogen embrittlement (AD+HE).

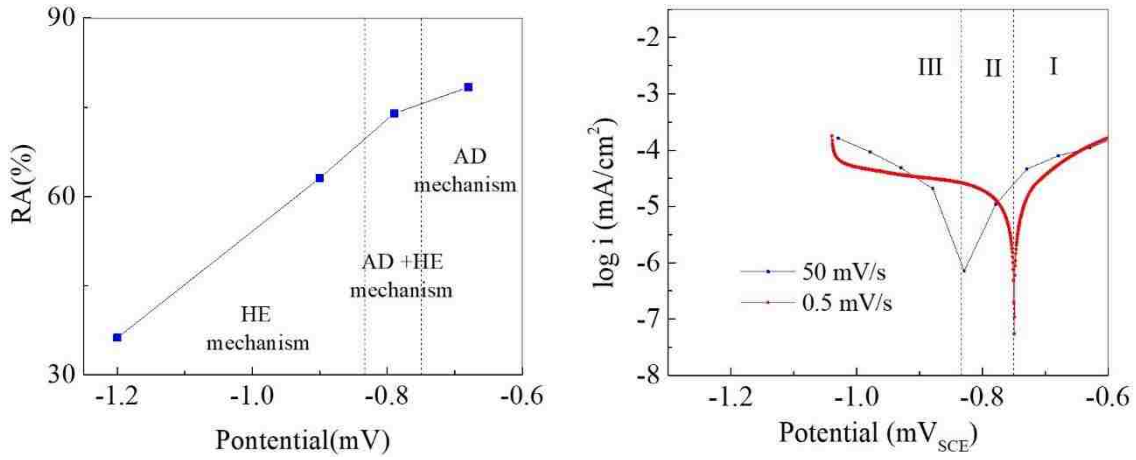

(a) (b)

Figure 8.6. SCC susceptibility of the steel coupon samples in NS4 solution as a function of the cathodic potential (a) and the corresponding polarization curves (b) measured at slow and fast potential scanning rates.

8.3.4. EIS Test. The corresponding corrosion test results are presented in Figure 8.7. The Nyquist plots of all the tested samples with different potentials applied show different forms of semicircle arcs. The coupon sample surface is assumed to be quasi-stable so that the EIS test was conducted from the beginning to the fracture of the coupon sample. The semicircle arc of the sample tested under the OCP increases significantly from 0.7 h to 3.4 h of immersion, and then stabilized till 8.9 h, which is slightly increased afterwards. The radii of semicircle arcs of the samples tested under a cathodic potential of -0.79 V/SCE and -0.90 V/SCE and the sample tested under -1.2 V/SCE are larger than and similar to those under the OCP, respectively. The radii of semicircle arcs of all the samples tested under cathodic potentials decrease as the cathodic potentials decrease. Therefore, the cathodic potential can change the corrosion behavior of the steel pipeline. An equivalent circuit model (EEC) was used to fit into the impedance data. Model $R_s(Q(R_{ct}W))$ and Model $R_s(QR_{ct})$ were used for the samples tested under the OCP and the CP, respectively. Here, R_s represents the solution resistance and R_{ct} represents the charge transfer resistance at the steel-electrolyte interface. A constant phase element (CPE) representing the double layer capacitance was used to replace a pure capacitor because of uneven roughness and a distribution of electrochemical reactivity on the surface of steel samples. A Warburg impedance W was included in the model to take into account the diffusion behavior, which was induced by the accumulation of corrosion products on the corrosion active sites. Figure 8.8 shows the extracted charge transfer resistance over time. Overall, R_{ct} of all the samples tested under cathodic potentials show a slow increase over time. It drops slightly when the cathodic potential decreases from -0.79 V/SCE to -0.9 V/SCE but dramatically from -0.9 V/SCE to -1.2 V/SCE. The charge transfer resistance against electrons transferring across

the steel surface is inversely proportional to the corrosion rate. Therefore, the sample tested under -0.79 V/SCE has the lowest corrosion rate while the sample tested under -1.2 V/SCE has the highest corrosion rate among all the samples tested under the CP. As there is no cathodic protection for the sample tested under the OCP, the sample has the highest corrosion rate.

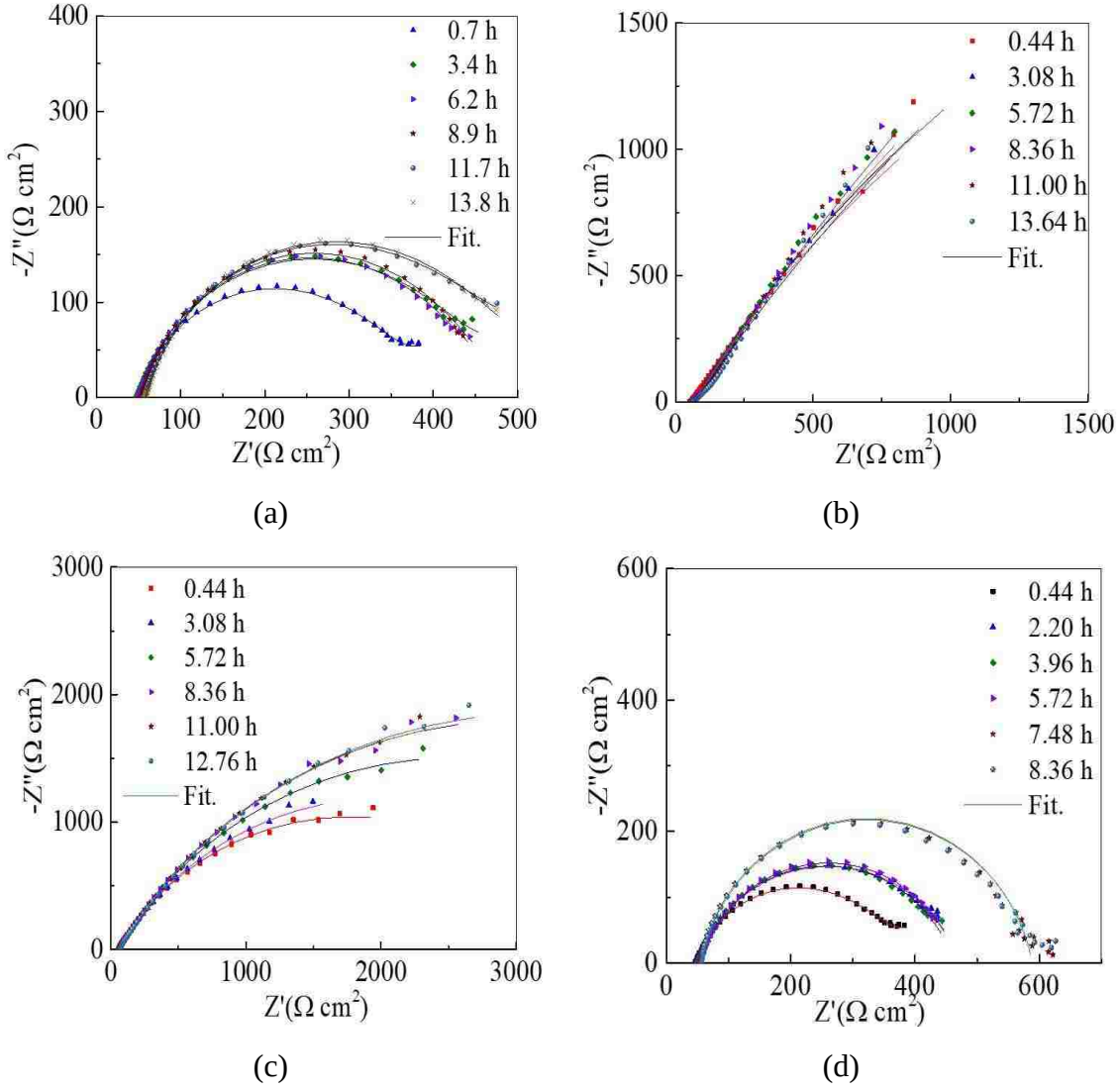

Figure 8.7. Nyquist plots from samples tested under a cathodic potential of (a) 0 (open circuit condition); (b) -0.79 vs. SCE/V; (c) -0.90 vs. SCE/V; (d) -1.2 vs. SCE/V.

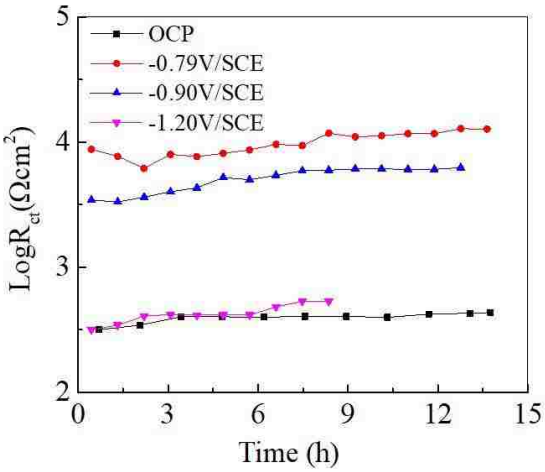

Figure 8.8. Charge transfer resistance over time for different samples tested under various cathodic potentials.

8.3.5. Fracture Surface Morphology. Figure 8.9 shows a suite of SEM images for the understanding of fracture characteristics. The surfaces fractured in air consist of a number of small dimples and micro-voids. Apparent necking can be observed with no cracks on the side wall, which demonstrates a totally ductile fracture. For the fracture surfaces of the coupon tested under the OCP, dimples and micro-voids can still be observed but corrosion products cover one fracture surface, which means the anodic dissolution dominates the cracking process. Some side wall cracks demonstrate that the coupon is susceptible to SCC.

The surfaces fractured under a cathodic potential of -0.79 V/SCE still have micro-voids and small dimples that are covered by crystallization of the chemical compositions. A mixture of quasi-cleavage and dimples appeared on the surface so the fracture contains both ductile and brittle fracture. For the coupon tested under a cathodic potential of -0.9 V/SCE, the necking is not in the round shape and the fracture surface is uneven and dominated by dimples and river-like cleavage. For the coupon tested under a cathodic

potential of -1.2 V/SCE, there is no apparent necking and the fracture is totally cleavage. With the decrease of cathodic potential, the fracture surfaces gradually transform from the ductile to brittle stage. As more hydrogen is generated with the decrease of cathodic potential, the coupons are more prone to hydrogen-induced embrittlement.

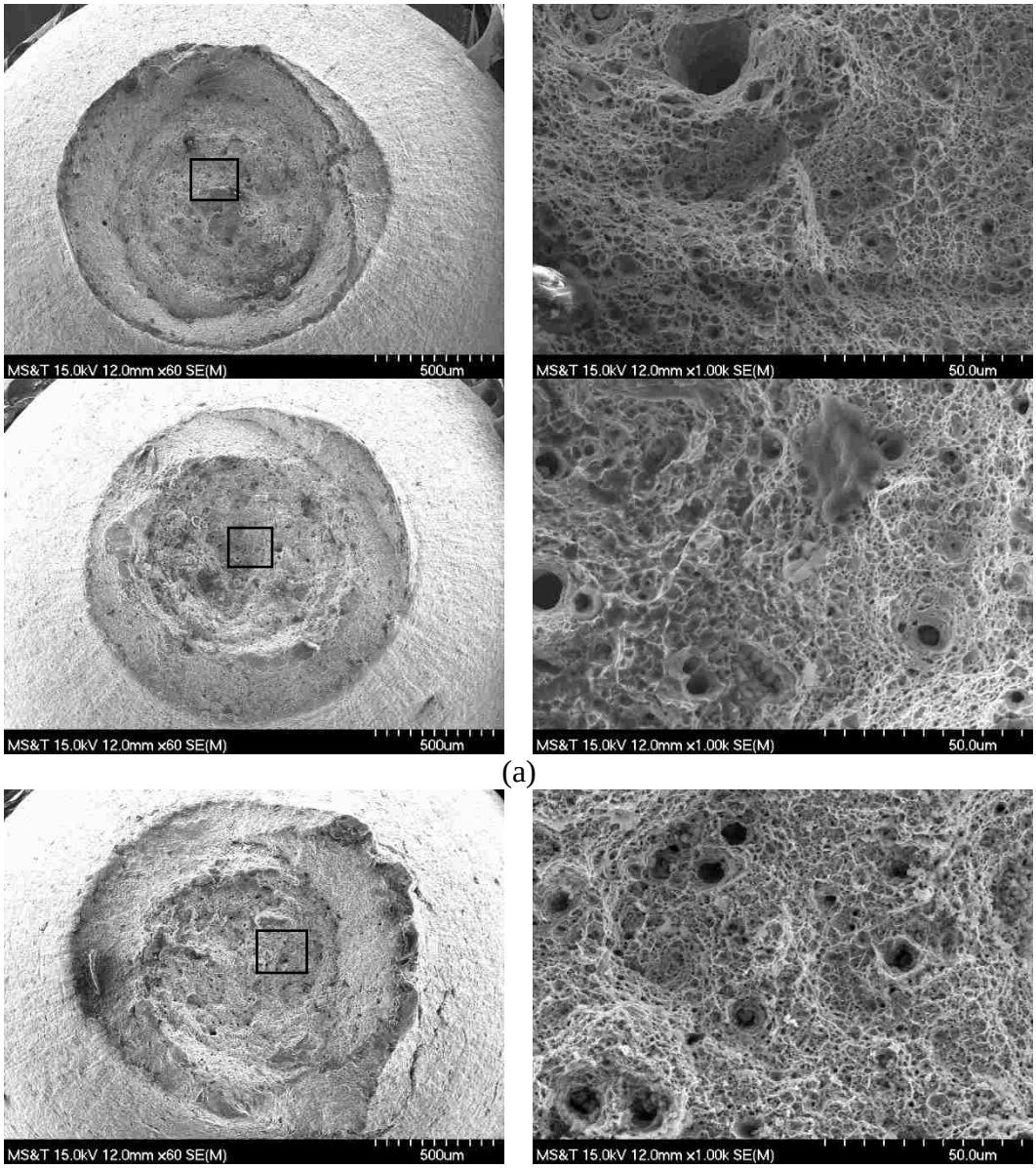

Figure 8.9. Fracture surface morphology of steel coupon samples with different applied potentials after SSRT: (a) in the air; (b-e) in the simulated soil solution at cathodic potential of 0, -0.79 V, -0.9 V, and -1.2 V, respectively.

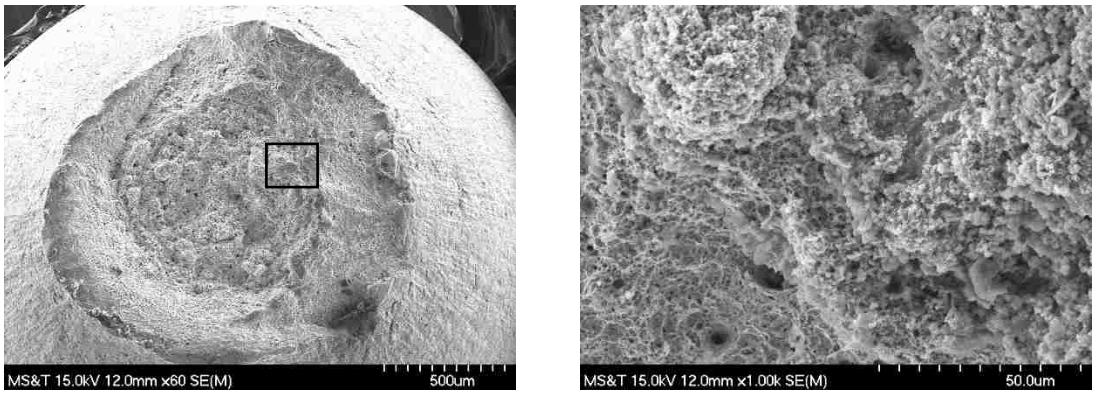

(b)

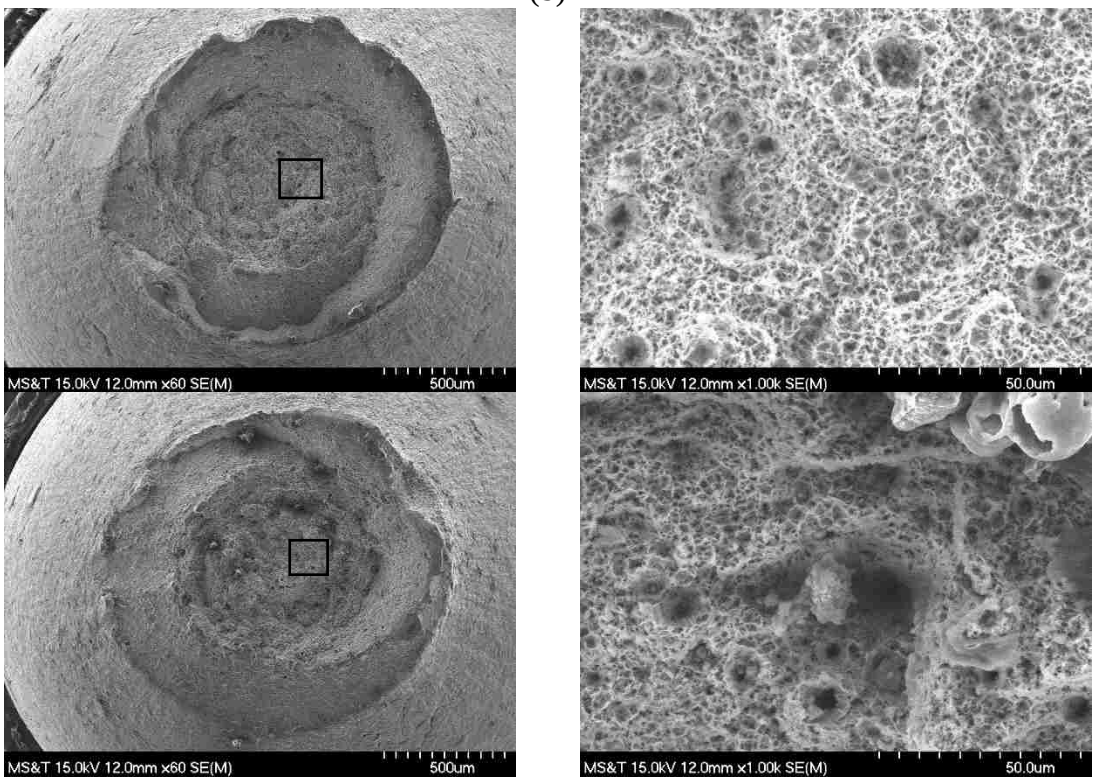

(c)

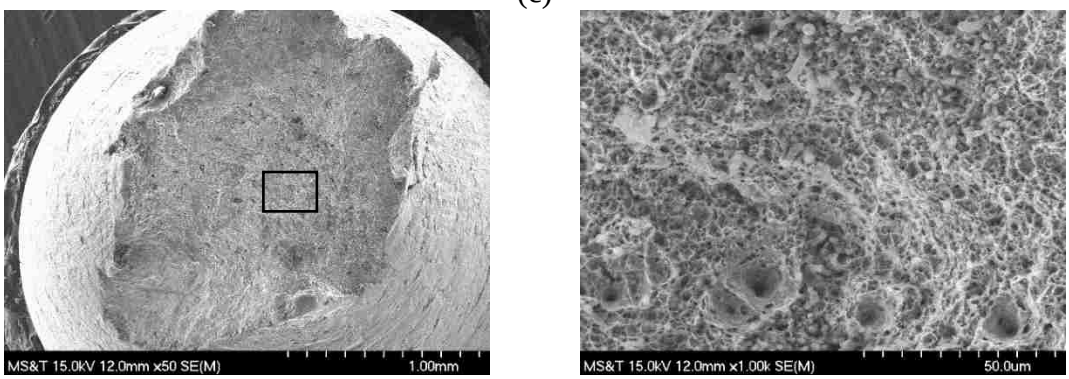

Figure 8.9. Fracture surface morphology of steel coupon samples with different applied potentials after SSRT: (a) in the air; (b-e) in the simulated soil solution at cathodic potential of 0, -0.79 V, -0.9 V, and -1.2 V, respectively (cont.).

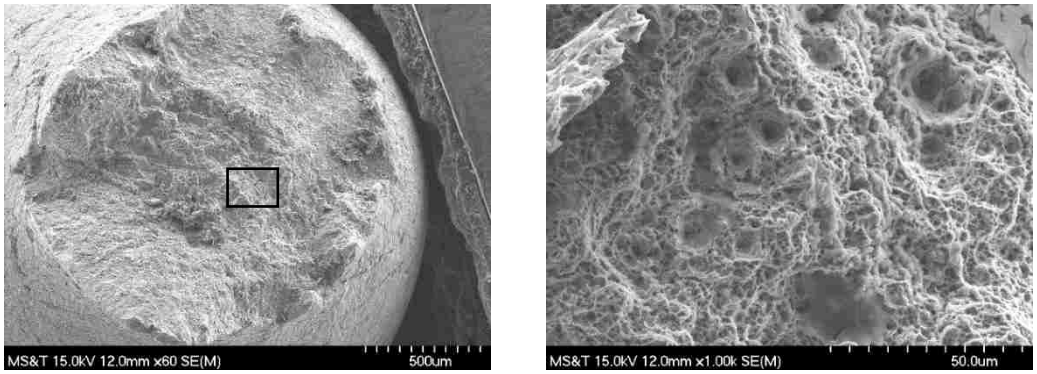

(d)

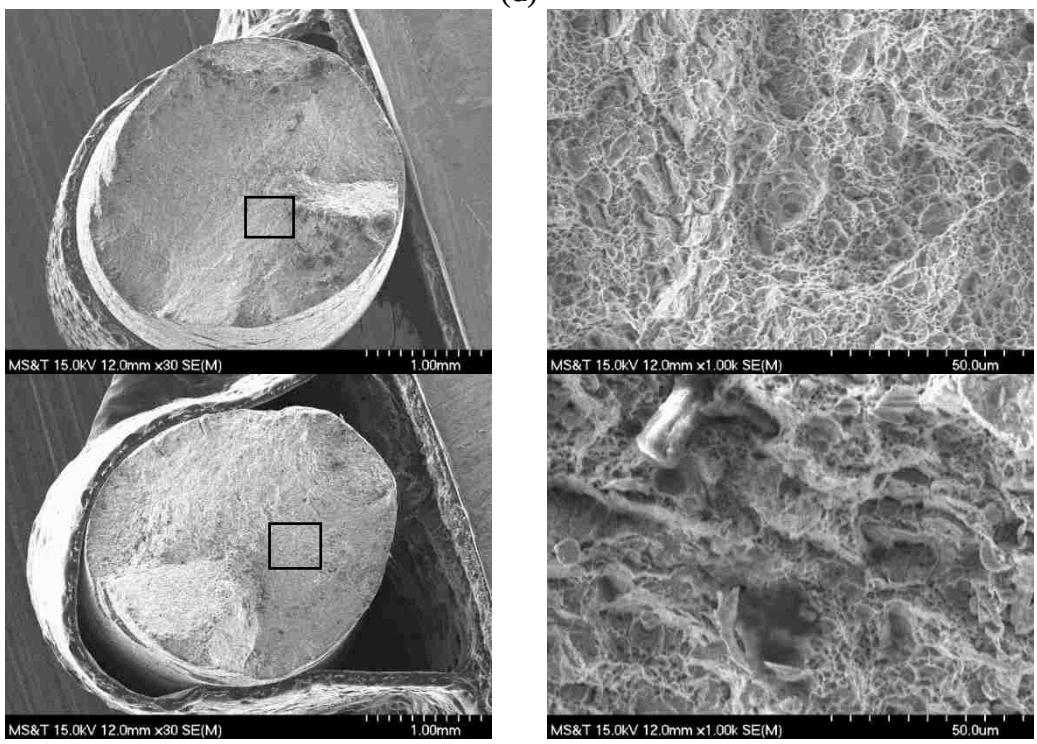

(e)

Figure 8.9. Fracture surface morphology of steel coupon samples with different applied potentials after SSRT: (a) in the air; (b-e) in the simulated soil solution at cathodic potential of 0, -0.79 V, -0.9 V, and -1.2 V, respectively (cont.).

8.4. SUMMARY

Based on the experimental results and analysis from one representative sample in each test condition, the following conclusions can be drawn:

1. The enamel-coated steel pipe is susceptible to SCC, depending on the applied potential. The more negative the applied potential, the higher SCC susceptibility the enamel-coated steel pipe.
2. The SCC mechanism is different in various potential zones. The cracking process is controlled by anodic dissolution in Zone I, hydrogen embrittlement in Zone III, and a combination of the anodic dissolution and the hydrogen embrittlement in Zone II.
3. CP changes the corrosion behavior of the steel pipe. The more negative the cathodic potential, the higher the corrosion rate.
4. The steel pipe gradually transforms in fracture mode from ductile to brittle as applied cathodic potential decreases.

9. CONCLUSIONS AND FUTURE WORK

9.1. MAIN FINDINGS FROM THE OVERALL DISSERTATION WORK

The chemically-bonded porcelain enamel coating has been developed for X65 steel pipelines to improve their corrosion protection and reduce their surface roughness or operation cost. Two types of enamel were coated on a steel pipe: Tomatec applied in the wet (spraying) process and GP2118 applied in the dry (electrostatic spraying) process. The thickness, surface roughness, porosity, bond strength, and corrosion resistance of enamel-coated steel samples were experimentally characterized. The stress distribution and stress corrosion cracking of enamel-coated steel pipes were evaluated from their finite element model under thermal residual stress, internal pressure and external effect due to soil movement and slow strain rate tests (SSRT). Based on the comprehensive experimentations and analyses, the following conclusions can be drawn:

1. The enamel coating applied on the steel samples at high temperature is under compression once cooled down due to their difference in CTE, which ensures that the enamel coating remained functional during normal operation. It has an amorphous structure with no crystalline phase observed. The GP2118 enamel coating contains fewer but larger isolated air bubbles than the Tomatec enamel coating. Both coatings cope well with small iron protrusions, ensuring strong bonding between the coatings and their steel substrate.
2. The surface roughness of the two coatings is approximately 1 μm, which can improve the flow efficiency of transported oil or gas. The enamel coatings applied on steel pipe samples fail through air bubbles inside the coatings, and

showed no sign of break at the coating-steel interface since small the coatings cope well with the steel through Fe protrusions.

3. Both enamel coatings show no sign of electrolyte penetration during the first two hours of corrosion tests, thus protecting steel substrates from corrosion. During the next 69 days, the results from three electrochemical tests (OCP, LPR, and EIS) are in general agreement. As electrolyte gradually penetrates through the coatings over time, the OCP values of all coated samples decrease, the corrosion current densities increase, and the coating resistance and charge transfer resistance decrease while the coating capacitance and the double layer capacitance increase. The coatings are good barriers against electrolyte penetration, protecting steel substrates from corrosion in sodium chloride solution. The enamel coatings reveal the same corrosion protective behavior as intact epoxy coating.
4. Intact enamel-coated samples perform well throughout the salt spray test. Only minor corrosion spots appear on the surface of samples after six weeks of salt spray test. No significant corrosion occurred during the entire salt spray tests. For the damaged samples, brown corrosion products on damaged points of all the tested samples are clearly observed after 48 hours of testing.
5. Enamel residuals remain among anchor points of their steel substrate after the enamel coating has been chipped off due to impact loading. The CP neither causes debonding between the coating and its steel substrate nor increases the degradation process of the coating. The CP can delay the electrochemical reaction at the steel-electrolyte interface when the steel is covered with intact

coating. The damaged coatings lose their barrier effect in protecting the steel substrate from corrosion. The introduction of CP does not improve the coating performance once damaged.

6. The residual thermal stress in coatings distributes uniformly in axial (longitudinal) direction of the steel pipe except at its ends. The maximum thermal residual stress is 2.55 MPa, which is much smaller than that of the chemical adhesion between the enamel and the steel. The stress concentration increases linearly with the internal pressure to about 480 MPa at an internal pressure of 25 MPa, which is close to the yield strength of the pipe steel. Further increase in internal pressure puts the pipe into a plastic range.
7. The enameled steel is susceptible to SCC, depending on the applied potential. The more negative the applied potential, the higher the SCC susceptibility. SCC mechanism varies in various potential zones. The cracking process is controlled by anodic dissolution in Zone I, hydrogen embrittlement in Zone III, and a combination of anodic dissolution and hydrogen embrittlement in Zone II. The fracture of steel samples gradually transforms from a ductile to brittle process as the applied cathodic potential decreases.

9.2. FUTURE WORK

The feasibility of enamel coating in pipeline applications has been studied comprehensively in this research. In collaboration with pipeline operators, the enamel coating may be applied into pipelines by developing a synchronized electrostatic spraying

and heating system and testing it in a field operation condition. However, the electrostatic enameling on full-size pipes requires further validation.

1. Connecting two pre-coated pipe segments through welding warrants further study since the welding procedure at high temperature may affect the properties of coating.
2. The long-term corrosion resistance and surface roughness of enamel coating needs further study under real-world pipeline operation conditions.
3. Electrostatic process is applicable to large-diameter pipes. Alternative coating process is needed when the diameter of pipes is smaller than the smallest spray gun.
4. It is necessary to develop additional handling specifications for transportation or handling to avoid potential damage to the glass lining of enamel coatings.
5. The vulnerability of glass lining to flexural cracks before the enamel-coated pipes reaches their yield point needs further investigation.
6. It is important to develop a repair procedure for any minor chipping or spalling of enamel coating.
7. The heating time period is significantly increased with the increase of pipe sizes, both diameter and length. Further experiments must be conducted to understand if the heating process has any adverse effect on the mechanical properties of enameled pipes.

BIBLIOGRAPHY

[1] G. H. Koch, M.PH Brongers, N. G. Thompson, Y. P. Virmani, and J. H. Payer, "Corrosion Cost and Preventive Strategies in the United States," No. FHWA-RD-01-156, 2002.

[2] T. Place, "Managing Corrosion of Pipelines that Transport Crude Oils," Materials Performance, March 2013.

[3] S. Prabhu, "Gas Pipelines: Internal Corrosion Protection and Fire Prevention," Corrosionpedia Newsletter, January 2016.

[4] https://primis.phmsa.dot.gov/comm/FactSheets/FSInternalCorrosion.htm?nocache=2447).

[5] Kehr, "Fusion-bonded Epoxy Internal Linings and External Coatings for Pipeline Corrosion Protection," Piping Handbook, NACE International, Houston, TX, 2003.

[6] P. A. Schweitzer, "Corrosion-Resistant Piping Systems," CRC Press, 1994.

[7] I. G. Berdzenishvili, "Synthesis of Law-Melting Pipe Enamel Coatings and Their Chemical Durability," American Journal of Materials Science, 6 (2), 2016.

[8] A. V. Ryabova, E. A. Yatsenko, V. V. Khoroshavina, and L. V. Klimova, "Glass-Enamel Corrosion-Resistant Coatings for Steel Pipelines," Glass and Ceramics, 74 (7-8), 2017.

[9] H. H. Liu, Y. Shueh, F. S. Yang, and P. Shen, "Microstructure of the Enamel-Steel Interface: Cross-Sectional TEM and Metallographic Studies," Materials Science and Engineering: A, 149(2), 1992.

[10] X. Yang, A. Jha, R. Brydson, and R. C. Cochrane, "An Analysis of the Microstructure and Interfacial Chemistry of Steel–Enamel Interface," Thin Solid Films, 443 (1), 2003.

[11] S. Rossi, N. Parziani, and C. Zanella, "Abrasion Resistance of Vitreous Enamel Coatings in Function of Frit Composition and Particles Presence," Wear, 332, 2015.

[12] F. Tang, G. Chen, R. K. Brow, J. S. Volz, and M. L. Koenigstein, "Corrosion Resistance and Mechanism of Steel Rebar Coated with Three Types of Enamel," Corrosion Science, 59, 2012.

[13] D. M. Yan, S. Reis, X. Tao, G. D. Chen, R. K. Brow, and M. L. Koenigstein, "Effect of Chemically Reactive Enamel Coating on Bonding Strength at Steel/Mortar Interface," Construction and Building Materials, 28 (1), 2011.

[14] G. A. Fogg, and J. Morse, "Development of A New Solvent-Free Flow Efficiency Coating for Natural Gas Pipelines," Proceedings of the 2005 Rio Pipeline Conference & Exposition in Riocentro, Rio de Janeiro, Brazil, October 17-19, 2005.

[15] Z. Liu, Y. Dong, Z. Chu, Y. Yang, Y. Li, and D. Yan, "Corrosion Behavior of Plasma Sprayed Ceramic and Metallic Coatings on Carbon Steel in Simulated Water," Materials and Design, 52, 2013.

[16] S. Guskov, "Application of Powder Coatings: Old Problems, New Findings, New Developments," Proceedings of the Powder Coating, 96 Conference in Indianapolis, Indian, September 18, 1996.

[17] F. Tang, X. Cheng, G. Chen, R. K. Brow, J. S. Volz, and M. L. Koenigstein, "Electrochemical Behavior of Enamel-Coated Carbon Steel in Simulated Concrete Pore Water Solution with Various Chloride Concentrations," Electrochimica Acta, 92, 2013.

[18] M. Mobin, A.U. Malik, I.N. Andijani, F. Al-Muaili, M. Al-Hajri, G. Ozair, and N.M.K. Mohammad, "Performance Evaluation of Some Fusion-Bonded Epoxy Coatings under Water Transmission Line Conditions," Progress in Organic Coatings, Vol. 62, 2008, pp. 369-375.

[19] Jr. M. Baker, and R. R. Fessler, "Pipeline Corrosion," Final Report to USDOT Pipeline and Hazardous Materials Safety Administration, November, 2008.

[20] ASME B46.1- 09, Standards: Surface Texture (Surface Roughness, Waviness, and Lay), American Society of Mechanical Engineering, 2009, New York, NY, USA.

[21] ASTM D4541-09e1, Standard Test Method for Pull-off Strength of Coatings Using portable Adhesion Tester, American Society for Testing and Materials (ASTM), 2010.

[22] PosiTest AT-M Pull-Off Adhesion Testers Quick Guide v.5.0, DeFelsko Corporation.

[23] PHMSA: Stakeholder Communications- Internal Corrosion. https://primis.phmsa.dot.gov/comm/FactSheets/FSInternalCorrosion.htm?nocache=2447

[24] Y. Zuo, R. Pang, W. Li, J. P. Xiong, and Y. M. Tang, "The Evaluation of Coating Performance by the Variations of Phase Angles in Middle and High Frequency Domains of EIS," Corrosion Science, 50(12), 2008.

[25] L. Fan, F. Tang, S. T. Reis, G. Chen, and M. L. Koenigstein, "Corrosion Resistance of Transmission Pipeline Steel Coated with Five Types of Enamels," Acta Metallurgica Sinica (English Letters), 30, 2017.

[26] F. Tang, Y. Bao, Y. Chen, Y. Tang, and G. Chen, "Impact and Corrosion Resistances of Duplex Epoxy/Enamel Coated Plates," Construction and Building Materials, 112, 2016.

[27] M. R. Presa, R. I. Tucceri, M. I. Florit, and D. Posadas, "Constant Phase Element Behavior in the Poly (o-toluidine) Impedance Response," Journal of Electroanalytical Chemistry, 502.1, 2001.

[28] Z. Yao, Z. Jiang, and F. Wang, "Study on Corrosion Resistance and Roughness of Micro-Plasma Oxidation Ceramic Coatings on Ti Alloy by EIS Technique. Electrochimica acta, 52.13 (2007): 4539-4546.

[29] M.E. Orazem, and B. Tribollet, "Electrochemical Impedance Spectroscopy," John Wiley & Sons: Hoboken, NJ, USA, 2008.

[30] C. Zhu, R. Xie, J. Xue, and L. Song, "Studies of the Impedance Models and Water Transport Behaviors of Cathodically Polarized Coating," Electrochimica Acta, 56(16), 2011.

[31] B. Hirschorn, M. E. Orazem, B. Tribollet, V. Vivier, I. Frateur, and M. Musiani, "Determination of Effective Capacitance and Film Thickness from Constant-Phase-Element Parameters," Electrochimica Acta, 55(21), 2010.

[32] P. Córdoba-Torres, T. J. Mesquita, O. Devos, B. Tribollet, V. Roche, and R. P. Nogueira, "On the Intrinsic Coupling between Constant-Phase Element Parameters α and Q in Electrochemical Impedance Spectroscopy," Electrochimica Acta, 72, 2012.

[33] J. Zhang, J. Hu, J. Zhang, and C. Cao, "Studies of Water Transport Behavior and Impedance Models of Epoxy-Coated Metals in NaCl Solution by EIS," Progress in Organic Coatings, 51(2), 2004.

[34] G. W. Walter, "A review of Impedance Plot Methods Used for Corrosion Performance Analysis of Painted Metals," Corrosion Science, 26(9), 1986.

[35] Y. Zuo, R. Pang, W. Li, J. P. Xiong, and Y. M. Tang, "The Evaluation of Coating Performance by the Variations of Phase Angles in Middle and High Frequency Domains of EIS," Corrosion Science, 50 (12), 2008.

[36] H. H. Hassan, E. Abdelghani, and M. A. Ami, "Inhibition of Mild Steel Corrosion in Hydrochloric Acid Solution by Triazole Derivatives: Part I. Polarization and EIS studies," Electrochimica Acta, 52 (22), 2007.

[37] F. Tang and G. Chen, "Chemically Reactive Enamel Coating of Steel Rebar for Enhanced Durability of Reinforced Concrete Structures," International Journal of Structural Engineering, 6(1), 2015.

[38] X. L. Zhang, Z. H. Jiang, Z. P. Yao, Y. Song, and Z. D. Wu, "Effects of Scan Rate on the Potentiodynamic Polarization Curve Obtained to Determine the Tafel Slopes and Corrosion Current Density," Corrosion Science, 51(3), 2009.

[39] R. H. Crowe, "What Transco Learned about Internal Coating of gas Pipelines," The Oil and Gas Journal, 57 (15), 1959.

[40] R. S. Lauer, "The Use of Internal Plastic Coatings to Maximize Sub-Sea System Operations," Steel Pipe, 30(40).

[41] Y. Charron, S. Duval S, D. Melot, S. Shaw, V. Alary, "Designing for Internally Coated Pipelines," 16th International Conference on Pipeline Protection, 2005.

[42] L. Pretorius, "New Application Technology for Internal Pipeline Coatings in Situ Pipeline Protection Using Pigging Techniques," NACE - International Corrosion Conference Series, 2006.

[43] R. S. Lauer, "The Use of High Performance Polymeric Coatings to Mitigate Corrosion and Deposit Formation in Pipeline Applications," NACE - International Corrosion Conference Series, 2006, No.77053.

[44] D. G. Manning, "Corrosion Performance of Epoxy-Coated Reinforcing Steel: North American Experience," Construction and Building Materials, 10(5), 1996.

[45] F. Tang, G. Chen, J. S. Volz, R. K. Brow, and M. L. Koenigstein, "Cement-Modified Enamel Coating for Enhanced Corrosion Resistance of Steel Reinforcing Bars," Cement and Concrete Composites, 35(1), 2013.

[46] Electrochemistry and corrosion: overview and techniques, Application note CORR-4, Princeton Applied Research.

[47] W. Lin, and A. Cheng, "Relationship Between Microscopy Contributions and Durability of Cement-Based Composites," Current Microscopy Contributions to Advances in Science and Technology, (A.Méndez-Vilas, Ed.), 2012.

[48] J. T. Zhang, J. M. Hu, J. Q. Zhang, and C. N. Cao, "Studies of Impedance Models and Water Transport Behaviors of Polypropylene Coated Metals in NaCl Solution," Progress in Organic Coatings, 49(4), 2004.

[49] ASTM B117—18, Standard Practice for Operating Salt Spray (Fog) Apparatus, American Society for Testing and Materials (ASTM), 2018.

[50] C.T. Love, G Xian, and V. M. Karbhari, "Cathodic Disbondment Resistance with Reactive Ethylene Terpolymer Blends," Progress in Organic Coatings 60(4), 2007.

[51] S. Martinez, L.V. Žulj, and F. Kapor, "Disbonding of Underwater-Cured Epoxy Coating Caused by Cathodic Protection Current," Corrosion Science 51(10), 2009.

[52] O. R. Lazutkina, M. G. Kostenko, S. A. Komarova, and A. K. Kazak, "Highly Reliable Energy-Efficient Glass Coatings for Pipes Transporting Energy Carriers, Liquids, and Gases," Glass and Ceramics 64(3-4), 2007.

[53] L. Fan, F. Tang, T. R. Signo, G. Chen, and M. L. Koenigstein, "Corrosion Resistances of Steel Pipes Internally Coated with Enamel," Corrosion 73(11), 2017.

[54] R. S. Lauer, "Advancements in the Abrasion Resistance of Internal Plastic Coatings," Materials Performance, 53(1), 2014.

[55] F. Deflorian and S. Rossi, "An EIS Study of Ion Diffusion through Organic Coatings," Electrochimica Acta 51(8), 2006.

[56] Q. L. Thu, H. Takenouti, and S. Touzain, "EIS Characterization of Thick Flawed Organic Coatings Aged under Cathodic Protection in Seawater," Electrochimica Acta 51(12), 2006.

[57] ASTM G14-04, Standard test method for impact resistance of pipeline coatings (falling weight test), American Society for Testing and Materials (ASTM), 2010.

[58] L. Samiee, H. Sarpoolaky, and A. Mirhabibi, "Microstructure and Adherence of Cobalt Containing and Cobalt Free Enamels to Low Carbon Steel," Materials Science and Engineering: A, 458 (1-2), 2007.

[59] H. H. Liu, Y. Shueh, F. S. Yang, and P. Shen, "Microstructure of the Enamel-Steel Interface: Cross-Sectional TEM and Metallographic Studies," Materials Science and Engineering: A, 149(2) 1992.

[60] J. M. Hu, J. Q. Zhang, and C. N. Cao, "Determination of Water Uptake and Diffusion of Cl^- Ion in Epoxy Primer on Aluminum Alloys in NaCl Solution by Electrochemical Impedance Spectroscopy," Progress in Organic Coatings 46(4), 2003.

[61] S. Ranade, M. Forsyth, and M. Y. J. Tan, "In Situ Measurement of Pipeline Coating Integrity and Corrosion Resistance Losses under Simulated Mechanical Strains and Cathodic Protection," Progress in Organic Coatings 101, 2016.

[62] Y. K. Son, L. C. Joo, L. J. Min, and K. B. Min, "Deformation Prediction of Porcelain-Enameled Steels with Strain History by Press Forming and High-Temperature Behavior of Coating Layer," Transactions of Nonferrous Metals Society of China, 22, 2012.

[63] Y. K. Son, K. H. Lee, K. S. Yang, D. C. Ko, and B. M. Kim, "Prediction of Residual Stress and Deformation of Enameled Steel," International Journal of Precision Engineering and Manufacturing 16(7), 2015.

[64] L. Xu, and F. Y. Cheng, "Assessment of the Complexity of Stress/Strain Conditions of X100 Steel Pipeline and the Effect on the Steel Corrosion and Failure Pressure Prediction," In the 9th International Pipeline Conference, American Society of Mechanical Engineers, September, 2012.

[65] National Energy Board (1996) Stress corrosion cracking on Canadian oil and gas pipelines, Report of the Inquiry, Report MH-2-95, NEB, Calgary, Alberta, Canada.

[66] P. Liang, X. Li, C. Du, and X. Chen, "Stress Corrosion Cracking of X80 Pipeline Steel in Simulated Alkaline Soil Solution," Materials and Design, 30(5), 2009.

[67] Y. F. Cheng, "Stress Corrosion Cracking of Pipelines," John Wiley and Sons, 2013.

[68] J. Jelinek, and P. Neufeld, "Temperature Effect on Pitting Corrosion of Mild Steel in De-aerated Sodium Bicarbonate-Chloride Solutions," Corrosion Science, 20, 1980.

[69] F. F. Eliyan, E. S. Mahdi, A. Alfantazi, A, "Electrochemical Evaluation of the Corrosion Behavior of API-X100 Pipeline Steel in Aerated Bicarbonate Solutions," Corrosion Science, 58, 2012.

[70] W. Chen, G. V. Boven, R. Rogge, "The Role of Residual Stress in Neutral pH SCC of Pipeline Steels: II. Crack dormancy," Acta Mater, 55, 2007.

[71] G.A. Zhang, Y. F. Cheng, "Micro-Electrochemical Characterization of Corrosion of Pre-cracked X70 Pipeline Steel in a Concentrated Carbonate/Bicarbonate Solution," Corrosion Science, 52, 2010.

[72] Y. Yang, and Y. F. Cheng, "Effect of stress on corrosion at Crack Tip on Pipeline Steel in a Near-Neutral pH Solution," Journal of Materials Engineering and Performance, 25(11), 2016.

[73] R. N. Parkins, W. K. Blanchard, and B. S. Delanty, "Transgranular Stress Corrosion Cracking of High-Pressure Pipelines in Contact with Solutions of Near-Neutral pH," Corrosion, 50, 1994.

[74] R. Chu, and W. Chen, "Microstructure Dependence of Stress Corrosion Cracking Initiation in X-65 Pipeline Steel Exposed to a Near-Neutral pH Soil Environment," Corrosion 60(3), 2004.

[75] Z. Y. Liu, X. G. Li, and Y. F. Cheng, "In-situ Characterization of the Electrochemistry of Grain and Grain Boundary of An X70 steel in a Near-Neutral pH Solution," Electrochemistry Communications, 12(7), 2010.

[76] M. Elboujdaini, Y. Z. Wang, R. Wang, W. Revie, M. T. Shehata, and R. N. Parkins, "Stress Corrosion Crack Initiation Processes: Pitting and Microcrack Coalescence," NACE International, 2000.

[77] T. Y. Jin, and Y. F. Cheng, "In Situ Characterization by Localized Electrochemical Impedance Spectroscopy of the Electrochemical Activity of Microscopic Inclusions in An X100 Steel," Corrosion Science, 53(2), 2011.

[78] T. Kushida, K. Nose, H. Asahi, M. Kimura, Y. Yamane, S. Endo, and H. Kawano, "Effects of Metallurgical Factors and Test Conditions on Near Neutral pH SCC of Pipeline Steels," NACE International, 2001.

[79] Z. Y. Liu, X. G. Li, and Y. F. Cheng, "Mechanistic Aspect of Near-Neutral pH Stress Corrosion Cracking of Pipelines under Cathodic Polarization," Corrosion Science 55, 2012.

[80] A. H. S. Bueno, B. B. Castro, and J. A. C. Ponciano, "Laboratory Evaluation of Soil Stress Corrosion Cracking and Hydrogen Embrittlement of API Grade Steels," 5th International Pipeline Conference in Calgary, Alberta, Canada, 2004.

[81] S. L. Asher, and P. M. Singh, "Role of Stress in Transgranular Stress Corrosion Cracking of Transmission Pipelines in Near-Neutral pH Environments," Corrosion, 65, 2009.

[82] B. T. Lu, J. L. Luo, and P. R. Norton, "Environmentally Assisted Cracking Mechanism of Pipeline Steel in Near-Neutral pH Groundwater," Corrosion Science 52(5), 2010.

[83] X. Chen, X. G. Li, C. W. Du, and Y. F. Cheng, "Effect of Cathodic Protection on Corrosion of Pipeline Steel under Disbonded Coating," Corrosion Science, 51(9), 2009.

[84] Z. Y. Liu, X. G. Li, and Y. F. Cheng, "Mechanistic Aspect of Near-Neutral pH Stress Corrosion Cracking of Pipelines under Cathodic Polarization," Corrosion Science, 55, 2012.

[85] L. Zhang, X. Li, C. Du, and Y. Huang, "Effect of Applied Potentials on Stress Corrosion Cracking of X70 Pipeline Steel in Alkali Solution," Materials & Design, 30(6), 2009.

[86] ASTM E8, Standard Test Methods for Tension Testing of Metallic Materials, American Society for Testing and Materials (ASTM), 2016.

[87] Z. Y. Liu, X. G. Li, C. W. Du, G. L. Zhai, and Y. F. Cheng, "Stress Corrosion Cracking Behavior of X70 Pipe Steel in An Acidic Soil Environment," Corrosion Science 50(8), 2008.

[88] NACE TM0198, Slow Strain Rate Test Method for Screening Corrosion-Resistant Alloys for Stress Corrosion Cracking in Sour Oilfield Service, NACE International Standard Test Method, 2016.

VITA

Liang Fan was born in Hegang, Heilongjiang Province, the People's Republic of China. He entered Southwest Jiaotong University, Chengdu, China, in 2008, and received his Bachelor of Science degree in Civil Engineering in June 2012. He was directly admitted into Master Program in Civil Engineering and exempted from the mandatory entrance exam due to his excellent academic performance. He received his Master of Science degree in 2014. He was then enrolled in the Ph. D Program in Civil Engineering at Missouri University of Science and Technology under the supervision of Professor Genda Chen. During his Ph. D study, he published nine papers in international journals. In May 2019, he received his Ph. D degree in Civil Engineering from Missouri University of Science and Technology, Rolla, Missouri. He was a student member of National Association of Corrosion Engineers (NACE).